9-26-2019 1:00 PM

Excess NO stabilizes the luminal domain of STIM2 in a Cys-specific manner thereby regulating basal calcium homeostasis and store-operated calcium entry

Matthew Novello
The University of Western Ontario

Supervisor
Stathopulos, Peter B.
The University of Western Ontario Co-Supervisor
Feng, Qingping
The University of Western Ontario

Graduate Program in Physiology and Pharmacology
A thesis submitted in partial fulfillment of the requirements for the degree in Master of Science

Recommended Citation

Novello, Matthew, "Excess NO stabilizes the luminal domain of STIM2 in a Cys-specific manner thereby regulating basal calcium homeostasis and store-operated calcium entry" (2019). *Electronic Thesis and Dissertation Repository*. 6570.
https://ir.lib.uwo.ca/etd/6570

Abstract

Stromal-interaction molecule 2 (STIM2) is an endoplasmic reticulum (ER) membrane-inserted Ca^{2+}-sensing protein which, together with the plasma membrane Ca^{2+} channel Orai1, regulates basal Ca^{2+} homeostasis and store-operated Ca^{2+} entry (SOCE). Recent evidence suggests that *S*-nitrosylation, which is the covalent attachment of a nitric oxide (NO) moiety to a cysteine thiol, can attenuate the function of the paralog STIM1 protein. Compared to STIM1, STIM2 also functions as a basal Ca^{2+} homeostatic feedback regulator. Therefore, the objective of my study was to evaluate the susceptibility of STIM2 to *S*-nitrosylation and the effects that this modification has on basal Ca^{2+} homeostasis, which is uniquely controlled by STIM2, as well as SOCE, which is regulated by both STIM1 and STIM2. Recombinant wildtype and Cys-mutated human STIM2 Ca^{2+} sensing luminal domain proteins were treated with either excess NO donor, *S*-nitrosoglutathione (GSNO), to promote *S*-nitrosylation or dithiolthreitol (DTT), to maintain reduced sulfhydryls as controls, to determine the effect of *S*-nitrosylation on the biophysical properties of the domain. Fura-2-AM ratiometric fluorimetry was used to probe basal Ca^{2+} and SOCE in mammalian HEK293T cells transiently co-overexpressing enhanced green fluorescent protein fused to Orai1 (*i.e.* eGFP-Orai1) and mCherry tagged full length STIM2 (*i.e.* mChSTIM2) variants in the presence or absence of excess NO. My data revealed that excess NO thermally and thermodynamically stabilized the full luminal domain of STIM2 in a Cys-dependent manner. Structurally, I found that excess NO alters the structure of the highly conserved core Ca^{2+} sensing region of STIM2 despite the *S*-nitrosylation sites being far in sequence space. Moreover, my data suggest that all three modifiable Cys sulfhydryls within the variable N-terminal region of STIM2 can contribute to enhanced luminal domain stabilization in the presence of excess NO. Consistent with the observed stabilization *in vitro*, I found that the basal Ca^{2+} and SOCE regulating function of STIM2 was suppressed in the full-length molecular context when live cells were exposed to exogenous NO. Taken together, this study reveals novel molecular insights into *S*-nitrosylation-mediated regulation of STIM2 structure and function via NO exposure, and is a first step towards understanding the complex role that NO may play in the regulation of cellular Ca^{2+}.

Keywords:

Stromal interaction molecule 2, nitric oxide, post-translational modifications, *S*-nitrosylation, store-operated calcium entry, basal calcium homeostasis

Layman Abstract

Stromal-interaction molecule 2 (STIM2) is a calcium (Ca^{2+}) sensing protein embedded within the endoplasmic reticulum (ER) membrane of cells. Upon ER luminal Ca^{2+} depletion, which can result from myriad physiological and pathological cellular signals, STIM2 becomes activated, and together with Orai1, a plasma membrane bound Ca^{2+} channel, can form Ca^{2+} release activated Ca^{2+} (CRAC) channels to elicit the influx of extracellular Ca^{2+} into the cytosol of cells, otherwise known as store operated Ca^{2+} entry (SOCE). Inappropriate activation of SOCE can lead to a wide range of pathologies, including neurodegeneration, heart muscle cell enlargement, and a weakened immune system. Recent evidence suggests that *S*-nitrosylation, or the covalent attachment of a nitric oxide (NO) moiety to cysteine residues, can suppress the function of Ca^{2+}-sensing proteins. Therefore, the objective of my study was to evaluate the susceptibility of STIM2 to *S*-nitrosylation and the downstream structural mechanism by which this modification can affect function. By utilizing *S*-nitrosoglutathione treatment, a chemical which can sufficiently *S*-nitrosylate proteins, and a wide range of spectroscopic techniques, my data elucidated the structural mechanism by which *S*-nitrosylation stabilizes the luminal region of STIM2 to suppress its function as a mediator of SOCE within mammalian cells. This study reveals novel molecular insights into *S*-nitrosylation-mediated regulation of STIM2 structure and function via NO exposure, and is a first step towards understanding the complex role that NO may play in the regulation of cellular Ca^{2+} to treat a wide range of pathologies.

Co-Authorship Statement

Drs. Peter B. Stathopulos and Qingping Feng supervised and greatly contributed to the design of all experiments. Dr. Peter B. Stathopulos and MengQi Zhang assisted in the generation of constructs. Dr. Peter B. Stathopulos and Jinhui Zhu contributed to the optimization of all experiments.

Epigraph

“Science may never come up with a better office communication system than the coffee break”

Earl Wilson

Acknowledgements

First and foremost, I would like to thank my primary thesis supervisor, Dr. Peter Stathopulos, for the support, guidance and encouragement you have given me throughout my graduate degree. If it wasn't for your confidence and trust in me, I wouldn't have had the chance of learning the satisfaction scientific discovery can offer. Under your guidance, I improved my scientific writing, oral presentation techniques, and laboratory skills, as well as to my ability to critically appraise the scientific literature. Your supervision fostered the development of my collaborative and communicative skills, proficiencies which I will continue to use for the rest of my life. Furthermore, the support and time you make for your students is something I strive to achieve in my own future mentoring. To simply say thank you would be an understatement. I would also like to thank my co-supervisor, Dr. Qingping Feng, for your encouragement, integrity, and scientific guidance. Your mentorship will have enduring effects on my future scientific accomplishments.

Thank you to my advisory committee members Dr. Rithwik Ramachandran and Dr. Timothy Regnault for your valuable feedback and assistance with my research endeavours. Furthermore, I wish to thank Lee-Ann Brier, for your strong practical, financial, and motivational support.

A very special thank you to Jinhui Zhu, a colleague, mentor, and friend. The many sacrifices she made to assist me with my experiments were instrumental in the completion of my project. Most importantly, her timeless support gave me the confidence to persevere on many challenging days.

I would also like to thank all of my present and past lab members from the Stathopulos and Feng laboratories. Your stimulating discussions made my time in the lab memorable and pleasant. An immense thank you to our lab associate, MengQi Zhang, for your comradeship right from the moment I met you. It was a privilege to work with such talented and intelligent young scientists.

Most importantly, to my incredible friends, loving family, and wonderful girlfriend, thank you for your unconditional love. Your support gave me the confidence to believe in myself and my dreams.

To all of my cohort, thank you. I wish you the best of luck with wherever life takes you.

Table of Contents

Chapter 2: Methods

Chapter 3: Results

Chapter 4: Discussion

List of Tables

List of Figures

List of Abbreviations

AD	Alzheimer's Disease
ANS	8-anilinonaphthalene-1-sulfonic acid
ARC	arachidonic acid-activated channels
ATP	adenosine triphosphate
BME	β-mercaptoethanol
Ca^{2+}	calcium
CAD	calcium release activated calcium activating domain
CaM	calmodulin
CaN	calcineurin
CC	coiled coil
CD	circular dichroism
cEF	canonical EF-hand
CRAC	calcium release activated calcium
CSP	chemical shift perturbation
Cys	cysteine
DLS	dynamic light scattering
DMEM	Dulbecco's modified eagle media
DTT	dithiothreitol
EDTA	ethylene-diaminetetraacetic acid
EGTA	ethylene glycol tetraacetic acid
eGFP	enhanced green fluorescent protein
GPCR	G-protein-coupled receptor
ER	endoplasmic reticulum
EtBr	ethidium bromide

Fura-2-AM	Fura-2 acetoxymethyl ester
GSNO	*S*-nitrosoglutathione
HBSS	HEPES buffered saline solution
HEK	human embryonic kidney
HEPES	4-(2-hydroxylethyl)-1-piperazineethanesulfonic acid
HSQC	heteronuclear single quantum coherence
ID	inhibitory domain
IP_3	inositol 1,4,5-trisphosphate
IP_3R	inositol 1,4,5-trisphosphate receptor
IPTG	isopropyl β-D-1 thiogalactopyranoside
K_d	Equilibrium dissociation constant
LB	Luria-Bertani broth
mCh	monomeric cherry
nEF	non-canonical EF-hand
Ni-NTA	nickel-nitrilotriacetic acid
NMR	nuclear magnetic resonance
NO	nitric oxide
OD_{600}	optical density at 600 nm
PBS	phosphate-buffered saline
PLC	phospholipase C
PM	plasma membrane
PMCA	plasma membrane calcium ATPase
SAM	sterile alpha motif
SDS-PAGE	Sodium dodecyl sulfate-polyacrylamide gel electrophoresis
SEC	size exclusion chromatography
Ser	serine

SERCA	sarco/endoplasmic reticulum calcium ATPase
SOCE	store-operated calcium entry
SR	sarcoplasmic reticulum
STIM	stromal interaction molecule
T_m	apparent midpoint of temperature unfolding
TG	thapsigargin
TRIS-HCl	trisaminomethane hydrochloride
UV	ultraviolent
WT	wildtype

Appendix: Copyrighted Material and Permissions

A version of Chapter 1 has been published in *Cell Calcium*. 2018 Jul; 73:88-94.

Matthew J. Novello[1], Jinhui Zhu[1], Qingping Feng[1], Mitsuhiko Ikura[2] and Peter B. Stathopulos[1]

[1]Department of Physiology and Pharmacology, University of Western Ontario, London, Ontario, Canada.
[2]Princess Margaret Cancer Center, University Health Network, Toronto, Ontario, Canada

"Structural elements of stromal interaction molecule function"

Chapter 1: Introduction

1.1 Overview

The importance of tightly regulating basal calcium (Ca^{2+}) levels is evident through myriad pathologies with dysregulated Ca^{2+} homeostasis, including neurodegenerative diseases, muscular dystrophies, and cardiovascular abnormalities (Davlouros et al., 2016; Mattson, 2007; Vallejo-Illarramendi et al., 2014). Stromal-interaction molecules (STIM)1 and 2 are endoplasmic reticulum (ER) membrane-inserted Ca^{2+} sensors that respond to fluctuations in ER luminal Ca^{2+} levels (Williams et al., 2001). Upon ER Ca^{2+} store depletion, STIMs become activated, which causes downstream initiation of store-operated Ca^{2+} entry (SOCE) and triggers an influx of Ca^{2+} into the cytosol (Roos et al., 2005; Zhang et al., 2005a). Dysregulation of SOCE can lead to perturbations of intracellular Ca^{2+} signalling and homeostasis, thus contributing to a multitude of disease states (Shaw and Feske, 2012).

Nitric oxide (NO) is a chemical compound involved in the regulation of the nervous, immune, and cardiovascular systems and is endogenously produced in the body by a family of enzymes termed nitric oxide synthases (NOS). Specifically, NOS can regulate the structure and function of Ca^{2+} binding proteins through the process of *S*-nitrosylation, or the covalent addition of a NO moiety to a reduced Cys residue to form *S*-nitrosocysteines (Gonzalez et al., 2007; Irie et al., 2015). Recent evidence suggests that *S*-nitrosylation can stabilize the luminal Ca^{2+} sensing domain of STIM1, thereby suppressing Ca^{2+} sensitivity and inhibiting SOCE activation (Gui et al., 2018; Zhu et al., 2018). While STIM1 predominately mediates larger and transient influx of Ca^{2+} into the cytosol, STIM2 mediates smaller and sustained influx (Stathopulos et al., 2009; Zheng et al., 2008). As a result, STIM2 has an additional and unique role of regulating basal Ca^{2+} homeostasis (Brandman et al., 2007). Although post-translational modifications which regulate STIM1 function have been extensively studied, little is known about how post-translational modifications affect STIM2 (Novello et al., 2018). Thus, the objective of my study was to determine if STIM2 is also susceptible to *S*-nitrosylation and the potential effects that this modification may have on basal Ca^{2+} homeostasis and SOCE regulation.

1.2 Calcium

1.2.1 General functions of Ca^{2+}

Calcium ions (Ca^{2+}) are a universal signalling ion essential for life. With more than 99% of Ca^{2+} in the human body immobilized in bone, it may seem unlikely that Ca^{2+} plays such an important role in maintaining homeostasis. Despite the small percentage of ionized Ca^{2+} in solution, by interacting with proteins and affecting electrochemical environments, Ca^{2+} is involved in a myriad of physiological processes including neuronal activity, apoptosis, muscle contractions, immune responses, and enzyme kinetics and activation (Cheng et al., 1993; Ebashi and Endo, 1968; Ghosh and Greenberg, 1995; Kikkawa et al., 1983; Orrenius et al., 2003; Walleczek, 1992).

From the moment cellular life begins to the time it ends, Ca^{2+} is intimately involved in cellular processes. During conception, the binding of a spermatozoa to an oocyte induces intracellular free Ca^{2+} oscillations to promote embryonic development mediated by upregulated transcription factors (Santella et al., 2004; Taylor et al., 1993). As development progresses, the initiation of localized intercellular Ca^{2+} signalling leads to an increase in embryonic cell number and contributes to the formation of the fetus (Poenie et al., 1985). On the opposite spectrum of cellular life, Ca^{2+} plays an important role in cell death. During cellular stress and injury, Ca^{2+} released after mitochondria Ca^{2+} overload can initiate pro-apoptotic signalling cascades which ultimately lead to programmed cell death (Mattson and Chan, 2003). Similarly, in cellular states where mitochondrial energy metabolism is altered, elevated intracellular Ca^{2+} levels cause widespread activation of various Ca^{2+}-dependent catabolic enzymes leading to necrosis (Orrenius et al., 2015).

Physiologic changes in Ca^{2+} levels are also implicated in the human immune system. Specifically, elevations in cytosolic Ca^{2+} can activate calcineurin, a calcium dependent protein phosphatase, which aids in positive selection during immature T-cell (thymocyte) development (Bueno et al., 2002). Disturbing the catalytic and regulatory subunits of calcineurin results in fewer positive thymocytes, or a reduction in positive selection (Neilson et al., 2004). Once matured, the binding of an antigen triggers elevated intracellular Ca^{2+} levels which activates T-cells. This elevation is mediated by phospholipase C-γ (PLC) (van Leeuwen and Samelson, 1999), which i) activates protein kinase C and Ras-dependent pathways, causing an influx of Ca^{2+} from the extracellular space and ii) produces 1,4,5-inositol trisphosphate (IP_3), causing an influx of Ca^{2+} into the cytosol from the ER. In order to efficiently activate T-cells to produce pro-inflammatory cytokines, a sustained Ca^{2+} response is required (Negulescu et al., 1994). This event is facilitated by elevated cytosolic Ca^{2+} levels, which can trigger the opening of Ca^{2+} release activated Ca^{2+} (CRAC) channels, allowing additional Ca^{2+} to flow into the cytosol (Cahalan and Chandy, 2009). The elevated cytosolic Ca^{2+} can then bind calmodulin, which can activate the nuclear factor of activated T-cells (NFAT) transcription factor, thus promoting long-term proliferation and maturation of activated T-cells (Macian, 2005).

Ca^{2+} also plays a major role in excitable and non-excitable cells, whereby ER membrane bound Ryanodine receptors (RyR) and IP_3 receptors (IP_3R) serve as the predominant channels that augment cytosolic Ca^{2+} levels from intracellular stores. Both structurally related channels regulate Ca^{2+} signals that mediate numerous cellular processes. For example, RyRs regulate excitation-contraction coupling in excitable skeletal muscle cells, while IP_3Rs regulate exocrine secretion in glandular cells (Berridge et al., 2003; Mikoshiba, 2007). It is important to note, however, that there are many pathways wherein RyRs and IP_3Rs are implicated in both physiological and pathological processes, which are not discussed here. Moreover, these previously mentioned pathways and processes are a small minority in which Ca^{2+} plays an important regulatory role.

1.2.2 Cellular Ca^{2+} homeostasis

As evident from the aforementioned pathways, it is essential to regulate cytosolic Ca^{2+} homeostasis. While specific concentrations vary slightly between cells, Ca^{2+} is effectively compartmentalized in the extracellular space (*i.e.* ~ 1 mM) with a concentration that is 10,000× higher than the resting cytosolic concentration (*i.e.* ~ 0.0001 mM). In order to establish this gradient, Plasma Membrane Ca^{2+}-activated ATPases (PMCAs) are involved, which causes an efflux of cytosolic Ca^{2+} into the extracellular space. Because of the sizeable difference in Ca^{2+} concentration, this efflux works against an electrical gradient created across the plasma membrane. As a result, many cells have additional Ca^{2+} efflux pumps, such as the Na^{+}-Ca^{2+} Exchanger (NCX), to remedy the electrical gradient and further regulate intracellular Ca^{2+} levels. Together, the PMCA and the NCX play important roles in the regulation of intracellular basal Ca^{2+} concentrations after a cell stimulus has occurred. Specifically, the high affinity, low capacity PMCA is efficient at removing intracellular Ca^{2+} when levels are low, thus preventing background ‘noise’ in Ca^{2+}

signalling cascades (Burette and Weinberg, 2007). On the other hand, the low affinity, high capacity NCX is efficient at removing large concentrations of Ca^{2+} quickly, thus enabling rapid and successive Ca^{2+} signalling, such as that seen in neurons (DiPolo and Beauge, 2006).

In addition to the extracellular space, Ca^{2+} is also segregated within intracellular stores. Under basal conditions, Ca^{2+} levels within the cytosol are similar to the mitochondria. Conversely, in times of cellular stress and injury, mitochondria can act as temporary Ca^{2+} stores in order to prevent cytosolic Ca^{2+} overload (Pinton et al., 2008; Rimessi et al., 2008). Consequently, mitochondrial Ca^{2+} concentration increases temporarily (~ 0.05 mM). Persistently high levels of mitochondrial Ca^{2+} generate reactive oxygen species and subsequently lead to oxidative stress, a key determinant in chronic heart failure (Peng and Jou, 2010; Santulli et al., 2015). To prevent this, Ca^{2+} is quickly extruded from the mitochondria through a number of channels such as the Leucine-zipper EF-hand containing Transmembrane protein-1 (LETM1) (Boyman et al., 2013; Lin and Stathopulos, 2019). Interestingly, the Golgi apparatus (Surroca and Wolff, 2000) and peroxisomes (Lasorsa et al., 2008) have also been shown to transiently store cytosolic Ca^{2+} in mammalian cells (~ 0.03 and ~ 0.1 mM, respectively). Finally, the largest intracellular organellar Ca^{2+} store is the ER (~ 0.4 – 0.7 mM). ER Ca^{2+} can be released into the cytosol in a process that is mediated by a plethora of electrochemical signals, for regulation of numerous cell functions, ranging from rapid striated muscle contraction to long-term gene regulation.

Because intracellular Ca^{2+} stores are limited, extracellular Ca^{2+} is critical for the activation of Ca^{2+}-dependent signalling cascades, which require more chronic elevations in cytosolic Ca^{2+}. The rise in cytosolic Ca^{2+} from intracellular stores, in concert with specific molecular signals, causes extracellular influx of Ca^{2+} and amplifies cytosolic Ca^{2+} levels. This process is termed store operated Ca^{2+} entry (SOCE) (Putney, 1986). In turn, these elevated Ca^{2+} levels can activate Ca^{2+}-dependent processes and replenish depleted intracellular Ca^{2+} stores, such as those within the ER, mitochondria, and Golgi apparatus.

1.3 SOCE and CRAC channels

Store operated Ca^{2+} entry (SOCE) is a highly conserved Ca^{2+} signalling mechanism, present in organisms ranging from lower eukaryotes such as *Caenorhabditis elegans* to higher vertebrates such as *Homo sapiens* (Cai, 2007; Yeromin et al., 2004). This concept of SOCE, first described in 1986, states that agonist-induced release of intracellular Ca^{2+} stores results in the influx of extracellular Ca^{2+} into the cytosol (Putney, 1986). The first of two essential components within this process is a single-pass transmembrane protein inserted within the ER membrane called Stromal Interaction Molecule (STIM), (Manji et al., 2000; Williams et al., 2001), which structurally responds to fluctuations in ER Ca^{2+} levels (Liou et al., 2005; Roos et al., 2005). The second essential component is Orai, a pore forming plasma membrane inserted protein (Prakriya et al., 2006). Together, STIM and Orai form the highly selective CRAC channel, which facilitates SOCE.

SOCE activation occurs after various types of cell stimulations. An initial stimulation of plasma membrane receptors, including G-protein-coupled receptors (GPCRs), receptor tyrosine kinases (RTKs), and T-cell receptors can lead to the production of a secondary messenger which triggers intracellular Ca^{2+} store depletion. One such mechanism is the binding of endothelin 1 (ET-1) to GPCRs in response to oxidative stress (Kahler et al., 2001; Kahler et al., 2000; Romero et al., 2009). Upon GPCR activation, the G_q subunit can activate PLC, which causes the catalytic cleavage of membrane bound phosphoinositide bisphosphate (PIP_2) into IP_3. Subsequently, IP_3 triggers ER Ca^{2+} store depletion by binding to IP_3 receptors (IP_3R) on the ER membrane. Because ER Ca^{2+} stores are limited, extracellular Ca^{2+} entry is necessary to sufficiently elevate and sustain cytosolic Ca^{2+} (Venkatachalam et al., 2002). The initial depletion of ER Ca^{2+} by IP_3-induced opening of IP_3R triggers the formation and opening of CRAC channels, causing extracellular Ca^{2+} entry into the cytosol (Fig. 1.1). The elevated Ca^{2+} levels effectively activate downstream signaling cascades and refill the depleted ER Ca^{2+} store through the sarco/endoplasmic reticulum Ca^{2+} transport ATPase (SERCA) pump. In general, the cytosolic Ca^{2+} increase mediated by STIM/Orai-constituted CRAC channels is more sustained and of a relatively lower capacity compared to cytosolic Ca^{2+} increases mediated by voltage- and mechanically-gated Ca^{2+} channels.

One of the major cell signaling outcomes mediated by SOCE is transcriptional regulation through the activation of various transcription factors such as Octamer-binding transcription factor 4 (Oct-4), cAMP Response Element Binding (CREB) protein and the Nuclear Factor of Activated T-cells (NFAT) protein (Hu et al., 2011; Hunton et al., 2002; Oh-hora and Rao, 2009; Pulver et al., 2004). However, SOCE is also implicated in numerous other physiological and pathological processes, including, but not limited to, the proliferation and activation of lymphocytes, the steering of developing growth cones in response to guidance cues, the maturation of spermatocytes, and the metastasis of neoplasms after remodeling of the tumor microenvironment [(Davis et al., 2016; Mo and Yang, 2018; Pavez et al., 2019; Zhou et al., 2014) for a comprehensive review, see (Putney et al., 2017)].

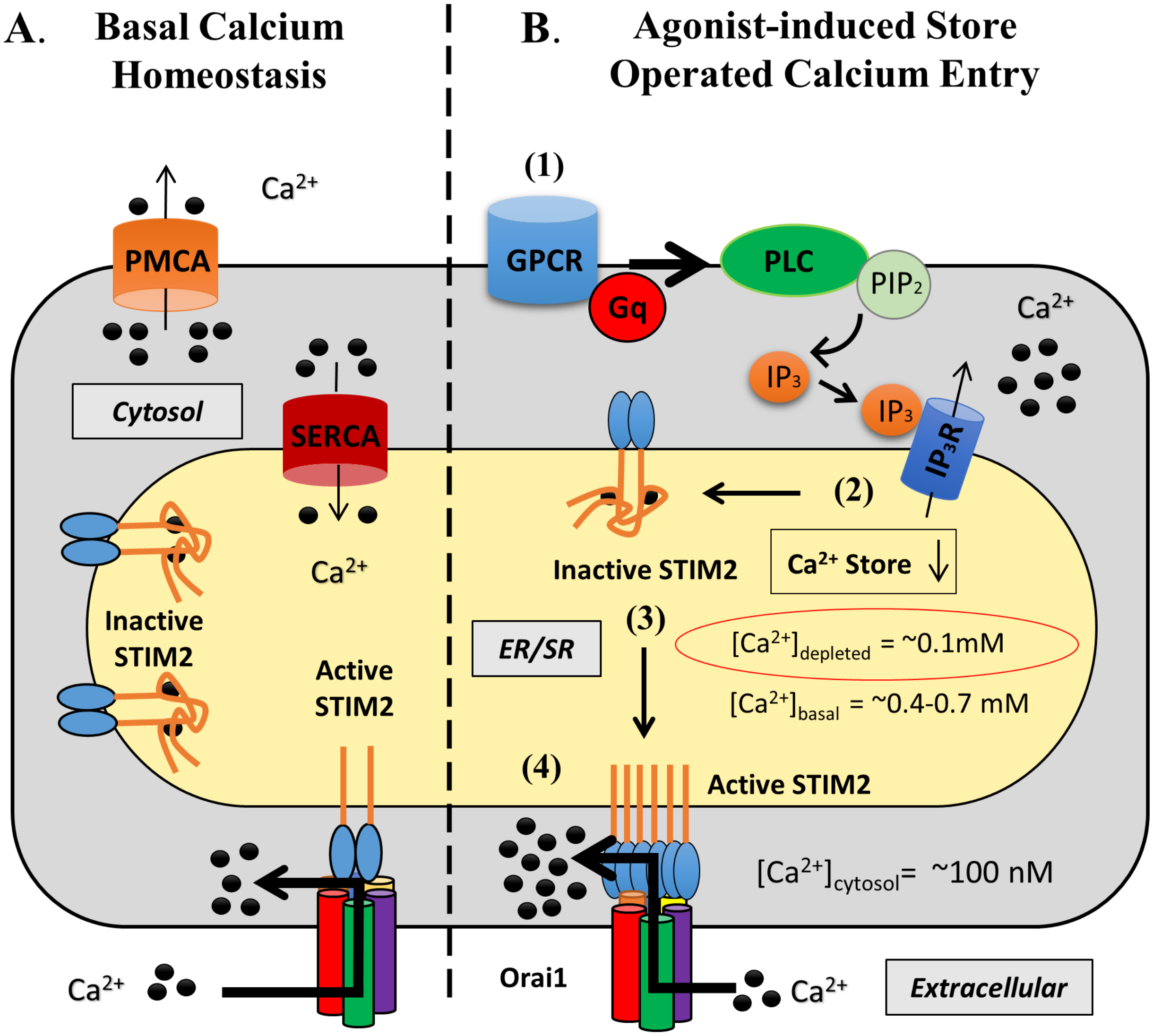

Fig. 1.1. Schematic diagram of STIM2 mediated Ca^{2+} regulation. (A) STIM2 mediated basal Ca^{2+} homeostasis. STIM2 normally remains in an inactive and quiescent state in replete ER/SR calcium stores. However, a small subset of STIM2 is in an active state, gating Orai1 channels to mediate an increase in basal calcium levels. ER membrane bound SERCA pumps and plasma membrane bound PMCA pumps remove Ca^{2+} from the cytosol. **(B)** STIM2 mediated agonist-induced store operated calcium entry (SOCE). (1) An initial stimulus leads to GPCR activation, subsequently causing IP$_3$ production from PIP$_2$ by PLC. (2) IP$_3$ initiates ER store depletion through IP$_3$R located on ER membranes. (3) The majority of STIMs become activated following ER Ca^{2+} depletion and mediate Orai1-composed CRAC channel formation, which (4) results in extracellular Ca^{2+} influx into the cytosol.

1.4 Stromal Interaction Molecule and Orai proteins

In all mammalian cells, SOCE is as an essential molecular pathway mediating cytosolic Ca^{2+} entry (Putney, 1986; Soboloff et al., 2006). As previously mentioned, STIM and Orai proteins are mediators of SOCE. In *Homo sapiens*, two STIM homologs exist: Stromal interaction molecule 1 (STIM1) and 2 (STIM2). Upon activation by ER Ca^{2+} depletion, human STIM1 undergoes structural changes which promote oligomerization and translocation to ER/PM junctions (Baba et al., 2006; Liou et al., 2007; Luik et al., 2006; Stathopulos and Ikura, 2013a). At these junctions, STIM1 interacts with and traps Orai1 proteins, forming CRAC channels. The direct interaction of STIM1 with Orai1 channels also facilitates gating of the CRAC channels to induce SOCE (Feske et al., 2006; Prakriya et al., 2006; Yeromin et al., 2006).

The human STIM2 paralog similarly regulates SOCE; however, STIM2 is less efficient than STIM1 in this cellular role. Instead, STIM2 is more closely involved in the regulation of basal Ca^{2+} homeostasis compared to STIM1 (Brandman et al., 2007). It is interesting to note that, in lower order eukaryotes such as *Drosophila melanogaster* and *Caenorhabditis elegans*, only one isoform of STIM exists. Thus, a molecular divergence of the STIM homolog occurred at some point during higher order eukaryotic evolution, suggesting a distinct function for STIM2 (Cai, 2007).

Orai proteins are the plasma membrane pore-forming components which mediate SOCE via CRAC channels. Three Orai homologs exists in humans: Orai1, Orai2, and Orai3. While all Orai components may be activated by exogenous STIM expression, only Orai1 is responsible for generating endogenous homomeric CRAC channel currents which underlie SOCE activation (Frischauf et al., 2009; Lis et al., 2007). On the other hand, Orai2 and Orai3 are mainly modulators of the predominately STIM1/Orai1 mediated Ca^{2+} channel currents (Hoth and Niemeyer, 2013). However, Orai3 channels appear to differ from Orai1 and Orai2 as they are slightly resistant to the process of Ca^{2+} de-potentiation (DeHaven et al., 2007).

1.4.1 STIM organization

Human *STIM1* can be translated into two isoforms, including 685 (*i.e.* STIM1) or 791 (*i.e.* STIM1L) amino acid polypeptides, whereas its paralog, *STIM2*, is translated into three isoforms, including 746 (*i.e.* STIM2 or STIM2.2), 754 (*i.e.* STIM2β or STIM2.1), and 841 (*i.e.* preSTIM2) amino acid polypeptides (Fig. 1.2). Interestingly, all three STIM2 isoforms share the same core architecture, which is similarly conserved with STIM1 isoforms.

The luminal region of STIMs (*i.e.* residing within the ER lumen) contains an ER targeting signal peptide (SP) sequence, an N-terminal region that is not conserved among phylogeny as well as canonical and non-canonical EF-hand motifs, and a sterile α-motif (SAM) domain that are conserved in STIMs from higher- to lower-order organisms (Fig. 1.3A). While there are no known modifications to the ER SP of STIM1, inefficient SP cleavage generates a cytosolic subpopulation of STIM2 which is not targeted to the ER (*i.e.* 841 amino acid isoform) and results in ineffective activation of Orai1 in a store-independent manner (Graham et al., 2011). As mentioned, the N-terminal region is highly variable among eukaryotes and between the human STIM homologs (Stathopulos and Ikura, 2009; Zhou et al., 2009). Despite the high variability, the short N-terminal regions of STIM1 and STIM2 can profoundly affect Orai1 channel activation kinetics (Zhou et al., 2009). Interestingly, two cysteine residues within this region are conserved between STIM1 (*i.e.* Cys49 and Cys56) and STIM2 (*i.e.* Cys53 and Cys60) (Fig. 1.3B), and post-translational modifications to these cysteines in STIM1 affect structure and function (Choi et al., 2017b; Gui et al., 2018; Zhu et al., 2018). It is important to note that STIM2 contains an additional modifiable cysteine residue (*i.e.* Cys15) within its variable N-terminal region. However, post-translational modifications that affect STIM2 structure and function have yet to be explored in any capacity (Novello et al., 2018).

The EF-hand, together with the SAM domain (EFSAM), constitute the Ca^{2+} sensing domain of STIMs. While it was initially proposed that STIMs only contained one EF-hand motif based on primary structure analysis, a high-resolution structure of STIM1 EFSAM revealed a second, non-canonical EF-hand (Stathopulos et al., 2008b). Interestingly, only the canonical EF-hand coordinates Ca^{2+}, where it can bind one Ca^{2+} ion (Stathopulos et al., 2006; Stathopulos et al., 2008b; Zheng et al., 2011b). However, a recent calorimetric analysis and competition study suggests as many as 5 Ca^{2+} binding sites may exist on STIM1 EFSAM, and up to 15 binding sites on STIM2 EFSAM [(Gudlur et al., 2018) reviewed by (Stathopulos and Ikura, 2019)]. The second non-canonical EF-hand exerts structurally stabilizing effects on the canonical EF-hand through hydrogen bonding (Stathopulos et al., 2008b). As a result of its essential role in stabilizing the canonical EF-hand, the non-canonical EF-hand is structurally conserved between STIM homologs despite the fact that it cannot measurably coordinate Ca^{2+} ions. In the presence of Ca^{2+}, the EF-hands adopt an "open" or "exposed" conformation where the two helices composing each EF-hand motif are in a semi-perpendicular conformation (Stathopulos et al., 2008b; Zheng et al., 2008). The open conformation exposes several hydrophobic residues that mediate interactions with the SAM domain. Thus, in the presence of Ca^{2+}, the EF-hand and SAM domains closely interact (*i.e.* EFSAM). In contrast, Ca^{2+} ion dissociation elicits a marked destabilization of the EFSAM domain interaction, ultimately resulting in the oligomerization of the full luminal region (Liou et al., 2007; Spassova et al., 2006a; Stathopulos et al., 2006; Stathopulos et al., 2013).

Despite the highly conserved EFSAM sequence between STIM homologs, the EFSAM domain of STIM2 is more structurally stable; however, STIM2 EFSAM has a weaker apparent Ca^{2+} binding affinity [Equilibrium dissociation constant (K_d) = ~0.4-0.8 mM] compared to STIM1 EFSAM (K_d = ~0.2-0.6 mM) (Stathopulos et al., 2006; Zheng et al., 2008; Zheng et al., 2011a). Given the resting ER lumen Ca^{2+} concentration (~0.4-0.7 mM) and the weaker apparent Ca^{2+} binding affinity, a larger subset of STIM2 molecules are partially active at resting ER Ca^{2+} levels, resulting in weak activation of Orai1 channels even in the absence of cell stimulation (Brandman et al., 2007; Miederer et al., 2015; Rana et al., 2015; Wang et al., 2014; Zheng et al., 2018). Thus, the ability of STIM2 to activate Orai1 under resting conditions suggests that STIM2 plays an important physiological role in maintaining basal Ca^{2+} homeostasis via a feedback mechanism dependent on ER luminal Ca^{2+} levels.

As previously mentioned, STIMs contain an ER-inserted, single pass transmembrane domain. While many factors contribute to the differing activation kinetics of STIM proteins, recent evidence suggests that differences between the transmembrane domains of STIM homologs are involved (Zheng et al., 2018). Previous research has shown that, when the transmembrane domain of STIM1 is swapped with that of STIM2 in the absence of Ca^{2+}, the chimeric STIM1 protein harbouring the STIM2 transmembrane domain transduces the Ca^{2+} depletion signal across the ER membrane to the cytosolic portion more slowly and less efficiently (Zheng et al., 2018). While not specifically determined, it is likely that two hydrophobic residues within STIM2, but not present in the STIM1 transmembrane domain, account for these differences.

The cytosolic regions of STIMs contain three coiled-coil (CC) domains, an inhibitory domain (ID) and two distally located Pro/Ser and Lys-rich domains (*i.e.* closest to the C-terminus) (Fig. 1.2). Previous studies indicate that the cytosolic region of STIMs can induce SOCE independently of the luminal Ca^{2+} sensing region (Kawasaki et al., 2009; Park et al., 2009; Yuan et al., 2009). Thus, the cytosolic domains contain all the molecular machinery needed to trigger Orai1-mediated SOCE activation. Located within the cytosolic region of STIM is the Orai-activating STIM fragment (OASF), which includes all three CC domains (*i.e.* CC1, CC2, and CC3). Furthermore, within the OASF is the STIM-Orai activating region [SOAR (also known as the CRAC-activating domain (CAD)], which includes the CC2 and CC3 domains. In the absence of ER Ca^{2+} depletion, CAD/SOAR are able to maximally elicit Orai1-mediated CRAC channel currents, making CC2-CC3 the minimal required domains needed to activate SOCE (Park et al., 2009; Yuan et al., 2009). Specifically, the CC2 region can directly interact with Orai1 in order to gate STIM/Orai1 mediated CRAC channels (Stathopulos et al., 2013). In addition to differences in the short N-terminal regions, EFSAM stability, and TM domains between STIM homologs, differences between CAD/SOAR amino acid sequences have also been demonstrated to regulate their distinct kinetics of activation, further supporting the notion that STIM1 functions as a more robust activator of Orai1 mediated CRAC channels (Brandman et al., 2007; Wang et al., 2014).

Interestingly, a STIM2 splice variant that retains exon 9 includes an additional 8 amino acids (*i.e.* VAASYLIQ) within the CC2 domain (*i.e.* STIM2β/STIM2.1; 754 amino acid isoform), negatively regulates Orai1 mediated SOCE (Miederer et al., 2015; Rana et al., 2015). Furthermore, incorporation of the STIM2β 8-amino-acid insert into full-length STIM1 protein abolished the robust SOCE response observed with wildtype STIM1 (Chung et al., 2018). These findings further support the role of STIM2 as a basal Ca^{2+} homeostatic feedback regulator, wherein non-functional STIM2β can heterodimerize with functional STIM2 (*i.e.* STIM2/STIM2β), thus impairing interactions with Orai1 and subsequently modulating Ca^{2+} homeostasis (Miederer et al., 2015). In contrast, the CC1 domain has opposite effects to those of the CAD and SOAR domains. When OASF and CC1 domains were co-expressed, Orai1 channel activity was inhibited (Fahrner et al., 2014). Additionally, the crystal structure of a STIM1 CC1 domain fragment (*i.e.* residues 237 – 310) illustrates that this region can form a long and extended helix (~13 nm), likely bridging the physical distance between the ER and PM membranes (Calloway et al., 2011; Cui et al., 2013). Therefore, the CC2 and CC3 domains of STIMs are required for the activation of Orai1. On the other hand, the CC1 domain is required to maintain the OASF region in a quiescent state when STIMs are inactive, but bring the cytosolic portion of STIMs in close proximity to membrane-bound Orai1 once activated. Downstream from the three CC domains is the acidic inhibitory domain (ID), which quickly inactivates STIM1-activated Orai1 channels in a Ca^{2+}-dependent manner (Derler et al., 2009) as well as a proline-serine rich region which can extensively undergo post-translational modifications (see section 1.6) to differentially regulate Ca^{2+} flux.

Finally, the polybasic lysine-rich region is located at the C-terminus and tethers STIMs to PM bound lipids (*i.e.* PIP_2) to stabilize STIMs at ER/PM junctions. Interestingly, studies have shown that deleting this region perturbs the interaction of STIM1 with the PM (Calloway et al., 2011; Stathopulos et al., 2013) and attenuates puncta formation (Barr et al., 2009) and SOCE activation (Jardin et al., 2013). It is worth noting that the polybasic region of STIM2 has a stronger affinity for acidic PM bound lipids than that of STIM1 (Bhardwaj et al., 2013), likely due to the additional basic Lys residues within this region. Taken together, these results suggest that, through multiple different types of biomolecular interactions, the cytosolic region regulates the activation state of STIMs and Orai channel activity.

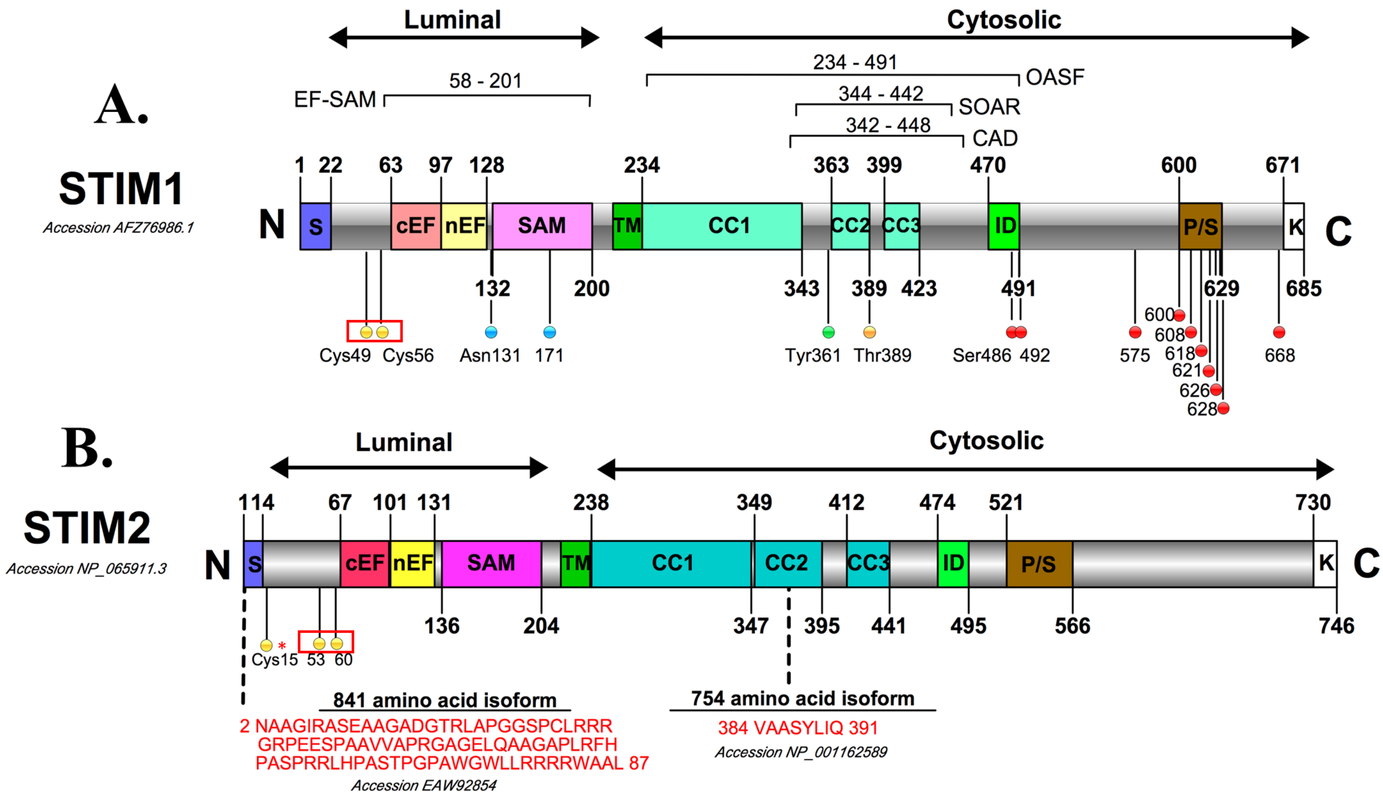

Fig. 1.2 Domain architecture of human STIM1 and STIM2 proteins. A. Key structural features on the human STIM1 domain architectures. Residue ranges are shown on top or bottom of the domain architecture. Domain boundaries and names of the various fragments used in the structure-function studies of STIMs are shown on top. The relative locations of detected post-translational modifications are shown below the diagram (yellow, *S*-nitrosylation or *S*-glutathionylation; blue, *N*-glycosylation; green, Tyr-phosphorylation; orange, Thr-phosphorylation; red, Ser-phosphorylation). **B.** Key structural features on the human STIM2 domain architectures. Residue ranges are shown on top or bottom of the domain architecture. Differences in sequence associated with the STIM2 isoforms are indicated by broken lines specifying the amino acid insertions. The potential *S*-nitrosylation sites under investigation are shown below the diagram in yellow. In *A* and *B*, the conserved Cys residues between STIM homologs are encompassed in a red box, while the unique Cys to STIM2 is emphasized by a red star. The cellular localization of the region of STIM is indicated on top of the diagrams. S, signal peptide; cEF, canonical EF-hand motif; nEF, non-canonical EF-hand motif; SAM, sterile α motif; TM, transmembrane; CC1, 2, 3, coiled-coil-1, -2, -3; ID, inhibitory domain; P/S, proline-serine-rich region; K, polybasic region. Adapted with permission, from Novello et al., 2018, *Cell Calcium*. 73:88-94.

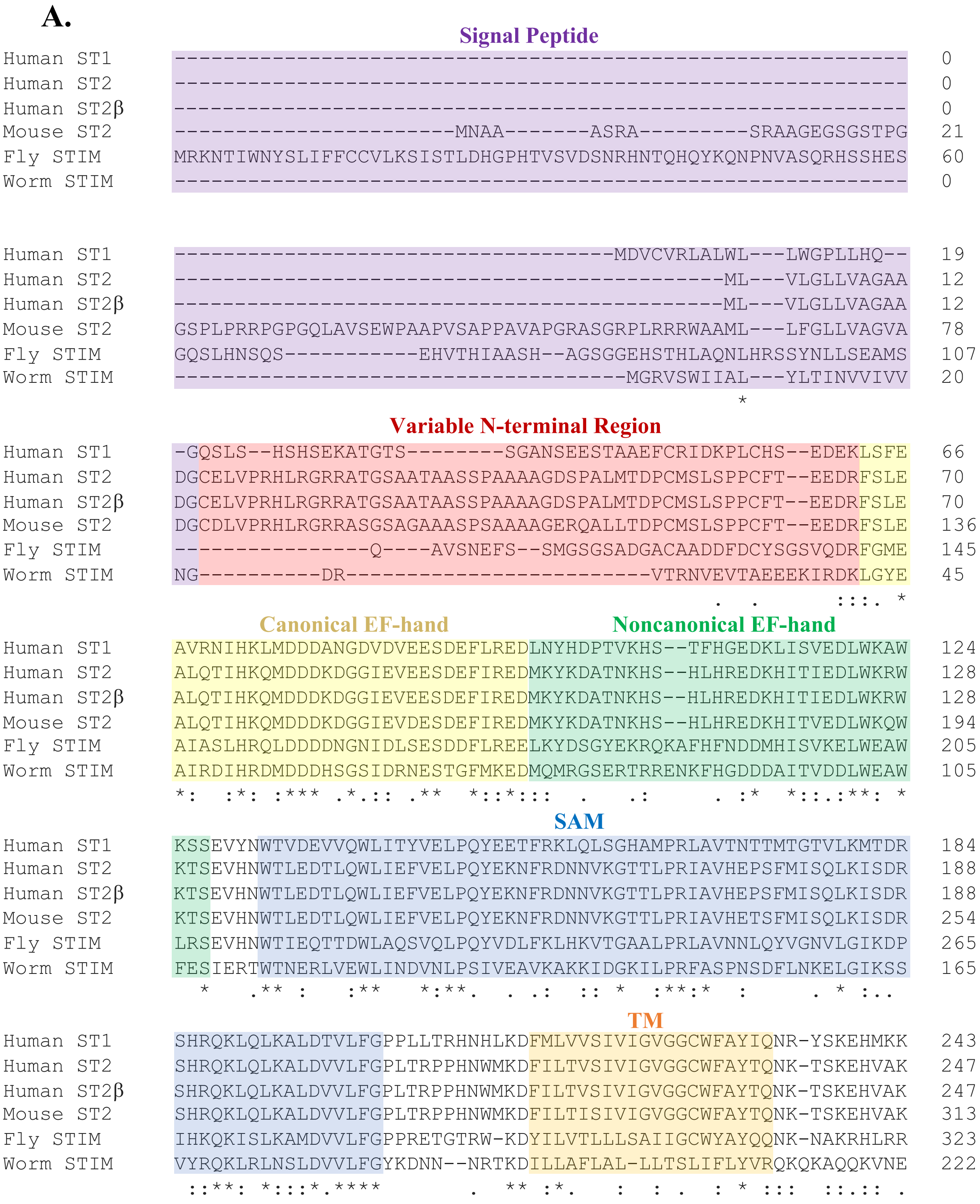

```
Human ST1      ------------------------------------------------------------   0
Human ST2      ------------------------------------------------------------   0
Human ST2β     ------------------------------------------------------------   0
Mouse ST2      -----------------------MNAA-------ASRA---------SRAAGEGSGSTPG   21
Fly STIM       MRKNTIWNYSLIFFCCVLKSISTLDHGPHTVSVDSNRHNTQHQYKQNPNVASQRHSSHES   60
Worm STIM      ------------------------------------------------------------   0

Human ST1      ------------------------------------MDVCVRLALWL---LWGPLLHQ--   19
Human ST2      ---------------------------------------------ML---VLGLLVAGAA   12
Human ST2β     ---------------------------------------------ML---VLGLLVAGAA   12
Mouse ST2      GSPLPRRPGPGQLAVSEWPAAPVSAPPAVAPGRASGRPLRRRWAAML---LFGLLVAGVA   78
Fly STIM       GQSLHNSQS-----------EHVTHIAASH--AGSGGEHSTHLAQNLHRSSYNLLSEAMS   107
Worm STIM      -------------------------------------MGRVSWIIAL---YLTINVVIVV   20
                                                             *

Human ST1      -GQSLS--HSHSEKATGTS--------SGANSEESTAAEFCRIDKPLCHS--EDEKLSFE   66
Human ST2      DGCELVPRHLRGRRATGSAATAASSPAAAAGDSPALMTDPCMSLSPPCFT--EEDRFSLE   70
Human ST2β     DGCELVPRHLRGRRATGSAATAASSPAAAAGDSPALMTDPCMSLSPPCFT--EEDRFSLE   70
Mouse ST2      DGCDLVPRHLRGRRASGSAGAAASPSAAAAGERQALLTDPCMSLSPPCFT--EEDRFSLE   136
Fly STIM       ----------------Q----AVSNEFS--SMGSGSADGACAADDFDCYSGSVQDRFGME   145
Worm STIM      NG----------DR-------------------------VTRNVEVTAEEEKIRDKLGYE   45
                                                           .  .      :::. *

Human ST1      AVRNIHKLMDDDANGDVDVEESDEFLREDLNYHDPTVKHS--TFHGEDKLISVEDLWKAW   124
Human ST2      ALQTIHKQMDDDKDGGIEVEESDEFIREDMKYKDATNKHS--HLHREDKHITIEDLWKRW   128
Human ST2β     ALQTIHKQMDDDKDGGIEVEESDEFIREDMKYKDATNKHS--HLHREDKHITIEDLWKRW   128
Mouse ST2      ALQTIHKQMDDDKDGGIEVDESDEFIREDMKYKDATNKHS--HLHREDKHITVEDLWKQW   194
Fly STIM       AIASLHRQLDDDDNGNIDLSESDDFLREELKYDSGYEKRQKAFHFNDDMHISVKELWEAW   205
Worm STIM      AIRDIHRDMDDDHSGSIDRNESTGFMKEDMQMRGSERTRRENKFHGDDDAITVDDLWEAW   105
               *:  :*: :*** .*.:: .**  *::*:::  .   .:     . :*  *::.:**: *

Human ST1      KSSEVYNWTVDEVVQWLITYVELPQYEETFRKLQLSGHAMPRLAVTNTTMTGTVLKMTDR   184
Human ST2      KTSEVHNWTLEDTLQWLIEFVELPQYEKNFRDNNVKGTTLPRIAVHEPSFMISQLKISDR   188
Human ST2β     KTSEVHNWTLEDTLQWLIEFVELPQYEKNFRDNNVKGTTLPRIAVHEPSFMISQLKISDR   188
Mouse ST2      KTSEVHNWTLEDTLQWLIEFVELPQYEKNFRDNNVKGTTLPRIAVHETSFMISQLKISDR   254
Fly STIM       LRSEVHNWTIEQTTDWLAQSVQLPQYVDLFKLHKVTGAALPRLAVNNLQYVGNVLGIKDP   265
Worm STIM      FESIERTWTNERLVEWLINDVNLPSIVEAVKAKKIDGKILPRFASPNSDFLNKELGIKSS   165
                 *   .** :   :**   *:**.  . .:  :: *  :**:*  :     . * :..

Human ST1      SHRQKLQLKALDTVLFGPPLLTRHNHLKDFMLVVSIVIGVGGCWFAYIQNR-YSKEHMKK   243
Human ST2      SHRQKLQLKALDVVLFGPLTRPPHNWMKDFILTVSIVIGVGGCWFAYTQNK-TSKEHVAK   247
Human ST2β     SHRQKLQLKALDVVLFGPLTRPPHNWMKDFILTVSIVIGVGGCWFAYTQNK-TSKEHVAK   247
Mouse ST2      SHRQKLQLKALDVVLFGPLTRPPHNWMKDFILTISIVIGVGGCWFAYTQNK-TSKEHVAK   313
Fly STIM       IHKQKISLKAMDVVLFGPPRETGTRW-KDYILVTLLLSAIIGCWYAYQQNK-NAKRHLRR   323
Worm STIM      VYRQKLRLNSLDVVLFGYKDNN--NRTKDILLAFLAL-LLTSLIFLYVRQKQKAQQKVNE   222
                ::**: *:::*.****       .  ** :*.   :  : .  : * :::  ::.:: .
```

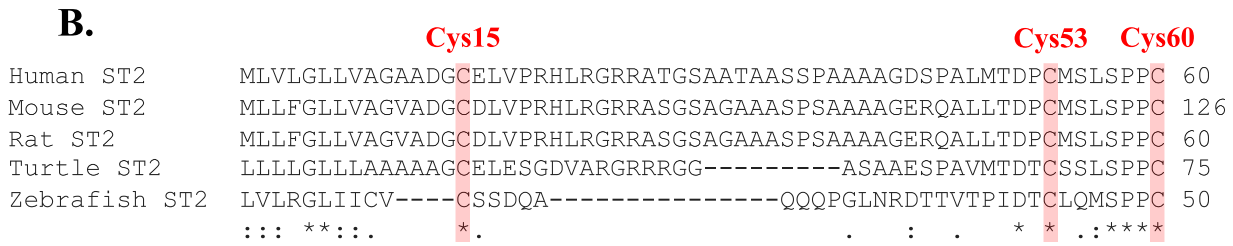

```
Human ST2         MLVLGLLVAGAADGCELVPRHLRGRRATGSAATAASSPAAAAGDSPALMTDPCMSLSPPC 60
Mouse ST2         MLLFGLLVAGVADGCDLVPRHLRGRRASGSAGAAASPSAAAAGERQALLTDPCMSLSPPC 126
Rat ST2           MLLFGLLVAGVADGCDLVPRHLRGRRASGSAGAAASPSAAAAGERQALLTDPCMSLSPPC 60
Turtle ST2        LLLLGLLLAAAAAGCELESGDVARGRRRGG---------ASAAESPAVMTDTCSSLSPPC 75
Zebrafish ST2     LVLRGLIICV----CSSDQA---------------QQQPGLNRDTTVTPIDTCLQMSPPC 50
                  ::: **::.     *.                       .   :  .   * * .:****
```

Fig. 1.3. Primary sequence alignment of STIM proteins. A. Multiple sequence alignment of luminal STIM protein regions. Primary sequences of STIM from human to lower-order organisms are aligned, including: *Homo sapiens* STIM1 (Human ST1; NCBI accession NP_003147.2); *Homo sapiens* STIM2 (Human ST2; NCBI accession NP_065911.3); *Homo sapiens* STIM2β (Human ST2β; NCBI accession NP_001162589.1); *Mus musculus* STIM2 (Mouse ST2; NCBI accession AAI45002.1); *Drosophila melanogaster* STIM (Fly STIM; NCBI accession NP_523357.2); *Caenorhabditis elegans* STIM (Worm STIM; NCBI accession CCD73857.1). Conserved domains are highlighted using various colours: Signal Peptide, purple; Variable N-terminal Region: red; Canonical EF-hand, yellow; Non-canonical EF-hand, green; Sterile α motif, blue; Transmembrane domain, orange. **B.** Multiple sequence alignment of the STIM2 variable N-terminal region from human to the lowest order *Stim2* containing organism (Cai, 2007), including *Homo sapiens* STIM2 (Human ST2; NCBI accession NP_065911.3); *Mus musculus* STIM2 (Mouse ST2; NCBI accession AAI45002.1); *Rattus norvegicus* STIM2 (Rat ST2; NCBI accession NP_001099220); *Terrapene exicana triunguis* STIM2 (Turtle ST2; NCBI accession XP_024060054.1); and *Danio rerio* STIM2 (Zebrafish ST2; NCBI accession XP_002660454.3). Conserved Cys residues between STIM2 homologs are highlighted in red; positions are relative to *Homo sapiens* STIM2. Alignments were performed using Clustal Omega (EMBL-EBI) software. Fully conserved (*), highly conserved (:), partially conserved (.).

1.4.2 Orai organization

While the high-resolution structure of the full-length human Orai channel has not been elucidated, a high-resolution crystal structure of the *Drosophila melanogaster* Orai channel exits. Both tetrameric and hexameric models have been proposed for Orai assembly during CRAC channel activation; however, recent evidence more strongly supports the hexameric conformation. First, the *D. melanogaster* crystal structure unequivocally shows that a single Orai channel adopts a hexameric quaternary structure (Hou et al., 2012). Moreover, HEK293 cells stably expressing STIM1 transfected with concatenated Orai1 channel constructs (*i.e.* tetramers and hexamers) revealed that Orai1 tetramers utilize only their N-terminal subunits in CRAC channel formation compared to all subunits in Orai1 hexamers (Cai et al., 2016). Consequently, Orai subunits most likely form a hexameric channel configuration when recruited by STIMs to mediate cytosolic Ca^{2+} flux.

Both crystal structure and bioinformatics analysis (*i.e.* sequence alignments) reveal that Orai is composed of four TM helices (*i.e.* TM1-TM4) localized at the PM (Feske et al., 2006; Hou et al., 2012). TM1 lines the pore and is responsible for the formation of the Ca^{2+} selectivity filter. Specifically, residue Glu106 of human Orai1 is required for Ca^{2+} binding, resulting in the high selectivity of CRAC channels. TM2 and TM3 are involved in promoting structural stability of the TM1 helix, whereas TM4 interacts with a neighbouring TM4 helix of another Orai subunit to stabilize dimer building blocks within the hexameric structure (Enomoto et al., 2017).

Both the N- and C-termini of Orai are located in the cytosol and facilitate the interaction with STIMs. As mentioned above, a small subset of STIM2 is in an active conformation and coupled to Orai1 channels under resting conditions (Brandman et al., 2007). For the majority of STIM1 and the remaining fraction of STIM2 molecules, upon ER Ca^{2+} store depletion, the EFSAM domains undergo a destabilization-coupled oligomerization. This oligomerization rearranges the TM domains and closely apposes the CC1 domains within STIM dimers. This CC1 clustering results in a release of the CAD/SOAR domain, which interacts with CC1 under ER Ca^{2+} loaded conditions. The release of the CAD/SOAR domain promotes further oligomerization of STIM molecules, and translocation of STIMs to ER/PM junctions. At these junctions, the polybasic domains interact with PM phosphoinositides and the C-terminal of Orai interacts with the

CAD/SOAR domain of STIMs to form CRAC channels (Stathopulos et al., 2013). Gating of the Orai1 channels requires interactions of CAD/SOAR with both the N- and C-termini of Orai, although the C-terminal interactions are higher affinity. All three Orai homologs (*i.e.* Orai1, Orai2, and Orai3) share conserved TM helices as well as residues required for Ca^{2+} sensitivity and selectivity. Interestingly, all forms of human Orai protein can assemble into functional heteromeric CRAC channels, each with unique functional characteristics based on STIM:Orai protein combinations (Lis et al., 2007).

1.4.3 STIM and Orai function

Together STIM and Orai proteins mediate both SOCE and basal Ca^{2+} homeostasis. While both STIMs can elicit SOCE, STIM1 is the principal regulator whereas STIM2 is primarily involved in basal Ca^{2+} regulation.

SOCE is triggered by agonist-induced ER luminal Ca^{2+} depletion. Normally, Ca^{2+} is bound to the EFSAM region of STIMs, maintaining an inactive, stable state. As reviewed above, following ER Ca^{2+} depletion, Ca^{2+} dissociation from the EFSAM results in destabilization and oligomerization of STIMs. These events lead to structural changes within the cytosolic CC domains such that STIMs adopt an "extended" conformation, translocate to ER/PM junctions and together with Orai1, form CRAC channels. This molecular collaboration ultimately causes the influx of extracellular Ca^{2+} into the cytosol, otherwise known as SOCE. It should be noted that resting, inactive STIM molecules are likely dimerized (Soboloff et al., 2012; Yang et al., 2012). Thus, the initial structural changes that occur during activation take place within the dimer; however, activated dimers further cluster during Orai1 activation. Interestingly, STIM1 and STIM2 can undergo heterodimerization, during which different combinations of STIM dimers differentially regulate SOCE (Fig. 1.4). Under high agonist stimulation, where ER Ca^{2+} levels drop below ~0.1 mM, STIM1 dimers predominately mediate larger influxes of Ca^{2+} into the cytosol through Orai1-mediated CRAC channels. Conversely, under low agonist stimulation, where ER Ca^{2+} levels fall between ~0.1-0.4 mM, STIM2 dimers predominately mediate smaller influxes of Ca^{2+} into the cytosol through Orai1-mediated CRAC channels (Berna-Erro et al., 2009; Brandman et al., 2007; Liou et al., 2005; Soboloff et al., 2006).

CRAC channels can be deactivated by a process known as Ca^{2+}-dependent inactivation (CDI). The ID of STIM1 provides a negative feedback signal to Ca^{2+} entry by triggering the inactivation of Orai1-mediated CRAC channel currents (Derler et al., 2009; Roos et al., 2005). Notably, a Ca^{2+} binding protein, calmodulin (CaM), is able to bind STIMs and Orai1 to facilitate Ca^{2+}-CaM-dependent CRAC channel inhibition. Isothermal titration shows that CaM binds to the polybasic C-termini of STIMs in a Ca^{2+} dependent manner (*i.e.* K_d ~1 μM with Ca^{2+} and ~100 μM without Ca^{2+}), a region critical for STIMs translocation and trapping at the PM, thereby disrupting STIM-Orai1 interactions and inactivating Orai1 channels (Bauer et al., 2008; Mullins et al., 2009; Yuan et al., 2009). Moreover, crystallography and isothermal titrations reveal that both the N- and C-terminal lobes of CaM can bind to the N-terminus of Orai1 in a Ca^{2+} dependent manner via hydrophobic interactions, thereby disrupting STIM-Orai1 interactions and inactivating Orai1 channels (Liu et al., 2012). Taken together, these data indicate that STIMs, together with Orai1, are mediators of SOCE and CRAC channel activity.

In summary, STIM2 aptly acts as an effective basal Ca^{2+} homeostatic feedback regulator due to several important differences compared to the STIM1 paralog. First, the EF-hand of STIM2 (K_d ~ 0.4-0.8 mM) has a lower Ca^{2+} affinity compared to STIM1 (K_d ~ 0.2-0.6 mM) (Brandman et al., 2007; Soboloff et al., 2012; Stathopulos et al., 2006). Consequentially, STIM2 is more sensitive to smaller decreases in luminal Ca^{2+} levels from resting levels. Second, the C-terminal polybasic domain of STIM2 has a stronger affinity for PM-bound PIP_2 than that of STIM1, which can tether STIM2 to the PM (Yuan et al., 2009). Third, compared to the SOAR domain of STIM1 (SOAR1), the SOAR domain in STIM2 (SOAR2) further unfolds the cytosolic region of STIM2, placing the Orai-activating SOAR2 region in the vicinity of Orai1 at rest (Zheng et al., 2018). Hence, SOAR2 has to move a shorter distance to activate Orai1 when compared to SOAR1. Fourth, when expressed in cells, a higher fraction of STIM2 appears to be pre-clustered near ER/PM junctions compared to STIM1, which causes constitutive activation of CRAC channels (Brandman et al., 2007). As a result, STIM2 is partially activated at resting ER luminal Ca^{2+} concentrations (0.4 - 0.7 mM) and constitutively induces basal Ca^{2+} entry through STIM2-activated Orai1 channels to regulate Ca^{2+} homeostasis (Fig. 1.4B). Collectively, these data indicate that, together with Orai1, STIM2 also functions as an efficient basal Ca^{2+} homeostatic feedback regulator.

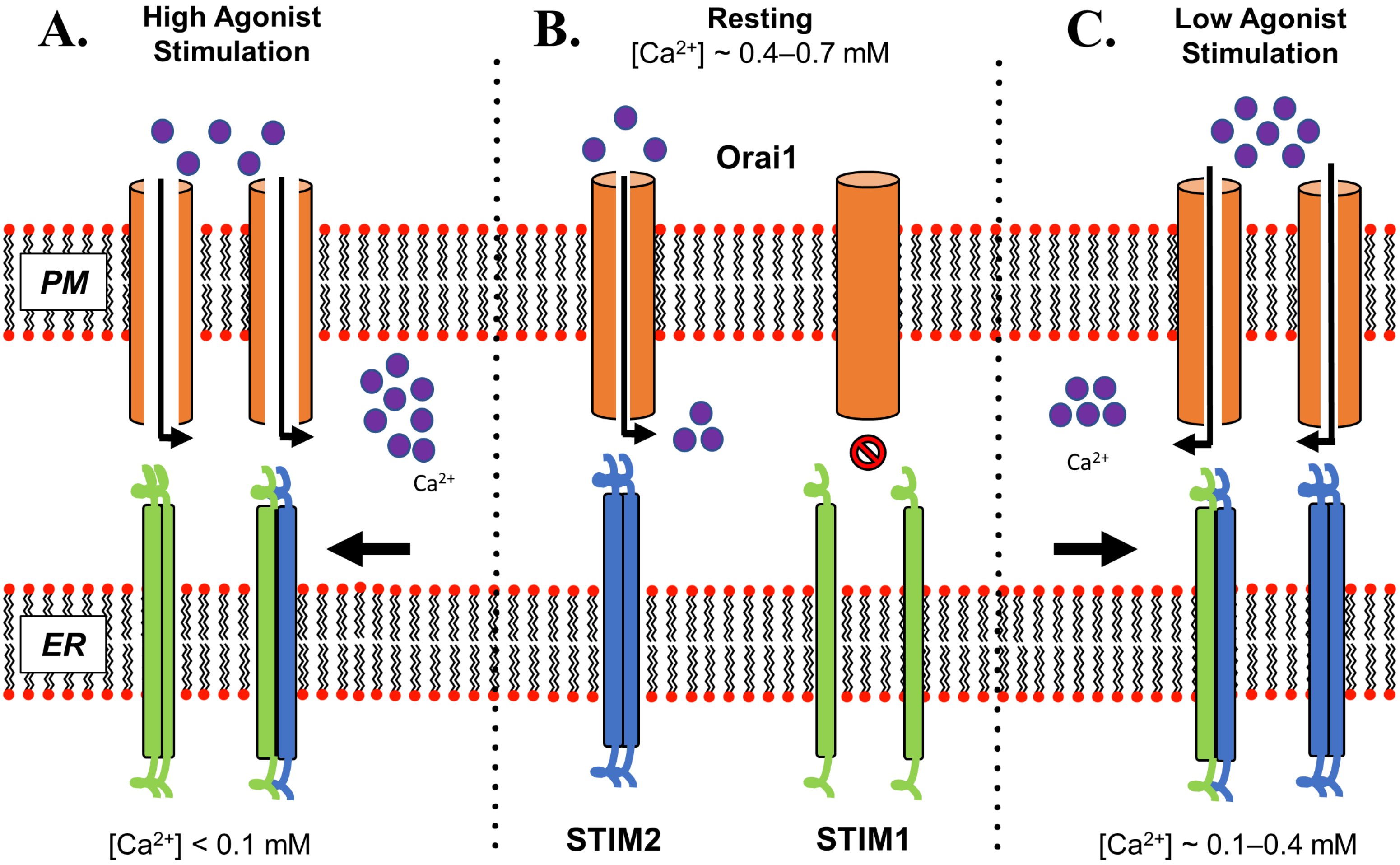

Fig. 1.4. STIM and Orai function under various ER Ca^{2+} concentrations. A. Under high agonist stimulation (ER Ca^{2+} concentration < 0.1 mM), activated STIM1 dimers predominately mediate large influxes of Ca^{2+} into the cytosol through Orai1 mediated CRAC channels. The influx mediated by high agonist stimulation is large enough to effectively activate downstream signaling cascades (Liou et al. 2005; Soboloff et al. 2006). **B.** A small subset of STIM2 dimers, but not STIM1, is activated under resting ER Ca^{2+} concentrations (~0.4–0.7 mM), which regulates basal Ca^{2+} homeostasis (Brandman et al. 2007). **C.** Under low agonist stimulation (ER Ca^{2+} concentration ~0.1–0.4 mM), activated STIM2 dimers predominately mediate smaller influxes of Ca^{2+} into the cytosol through Orai1-mediated CRAC channels (Berna-Erro et al. 2009; Brandman et al. 2007). In *A* and *C* some fractions of STIM1-STIM2 heterodimers have been proposed to form and be involved in regulating Ca^{2+} entry (Soboloff et al. 2012; Yang et al. 2012).

1.5 STIM-associated pathologies

The physiological importance of STIM proteins are emphasized by studies probing STIM-mediated Ca^{2+} flux in health and disease. STIM1/Orai1 double knockout mice typically die *in utero* or shortly after birth due to respiratory and immunological pathologies (Cahalan and Chandy, 2009; Vig et al., 2008). Additionally, mice lacking STIM2 progressively die between ~4 – 8 weeks after birth (Berna-Erro et al., 2009; Oh-Hora et al., 2008). Within the immune system, STIM1 is essential for Fc_{γ} receptor activation on phagocytes, which can trigger autoantibody and immune complex-induced diseases, such as systemic lupus erythematosus and rheumatoid arthritis (Braun et al., 2009). Despite the essential role of STIM1, evidence suggests a cooperative function between STIM homologs. While helper T-cell-specific deletion of STIM1 impairs T-cell function, the resultant phenotype is incomplete, suggesting a compensatory role of STIM2 (Ma et al., 2010). Moreover, B-cell specific deletion of STIM1 also results in an attenuated function wherein interleukin-10 production is significantly diminished; when both STIMs are deleted, interleukin-10 production is completely abolished (Matsumoto et al., 2011). Thus, STIM1 and STIM2 work in concert to mediate cellular responses within the immune system. While the pathological mechanism by which STIM proteins elicit disease are poorly understood, these results indicate that STIMs are essential for sustaining life and abnormalities in structure and function can result in a wide range of pathological complications (see below).

1.5.1 STIM1-associated pathologies

Perhaps the most widely studied system harbouring mutated STIM1 protein is the immune system. Mutations to various regions in STIM1 ultimately disrupt Ca^{2+} homeostasis, which can give rise to immunological pathologies. A single point mutation in the CC1 region of STIM1 (*i.e.* Arg304Trp) results in the autosomal dominantly inherited Stormorken Syndrome due to upregulated SOCE, which is characterized clinically by anemia, thrombocytopathy, and tubular aggregate myopathy (Misceo et al., 2014). On the other hand, a missense mutation in the CC3 region of STIM1 (*i.e.* Arg429Cys) results in an autosomal recessively inherited severe combined immunodeficiency-like syndrome due to reduced SOCE, which is characterized clinically by an increased susceptibility to infections (Maus et al., 2015).

1.5.2 STIM2-associated pathologies

While there are currently no identified pathologies caused by single mutations to human *STIM2* alleles, upregulated and hyperactivated STIM2 has been linked to numerous pathological conditions, especially within the nervous system. Compared to STIM1, STIM2 expression is relatively higher in neurons, suggesting that STIM2 plays a more prominent role in these cells (Lopez et al., 2012b). Specifically, STIM2 is involved in synaptic function and neuronal survival. Recent evidence using a conditional knockout mouse model suggests that STIM2 is involved in long-term potentiation of hippocampal neuronal synapses, and that deletion of STIM2 impairs plasticity (Yap et al., 2017). Moreover, STIM2, but not STIM1, was shown to be downregulated in mouse models of Alzheimer's disease (AD), which results in disturbed Ca^{2+} homeostasis concomitant with large losses of hippocampal neurons (Sun et al., 2014). Consistent with this report, only STIM2 overexpression was shown to correct aberrant Ca^{2+} flux in a similar mouse model of AD (Zhang et al., 2015). While not yet explored, STIM2 is likely involved in similar neurodegenerative diseases characterized by perturbed Ca^{2+} homeostasis.

1.6 STIM post-translational modifications

Proteins that mediate cell signaling cascades are often able to adopt multiple structural conformations which promote distinct functions. Post-translational modifications can play a pivotal role in controlling both intra- and inter-molecular interactions associated with biological function (Hunter, 1995). The CAD/SOAR domain of STIMs can undergo phosphorylation events that impact both structure and function (Table 1.1). STIMs mediate both store-dependent CRAC channel as well as store-independent arachidonic acid-regulated Ca^{2+}-selective (ARC) channel activations (Mignen et al., 2007; Shuttleworth, 2017). However, the underlying mechanism by which STIMs differentially activate these two processes was unknown until the discovery that phosphorylation of Thr389 by protein kinase A (PKA) induces structural changes leading to the selective activation of ARC channels (Thompson and Shuttleworth, 2015). Using molecular dynamics simulations and optical spectroscopy, it was demonstrated that phosphorylation of Thr389 in STIM1 induces a helical extension of the C-terminal region of the CC2 domain, resulting in an increased stability of the helix (Thompson et al., 2018). It is this structural conformation mediated by Thr389 phosphorylation that establishes STIM1 specificity in activating ARC channels over CRAC channels.

Tyrosine phosphorylation of STIM1 has been identified and may be required for STIM1 to couple to Orai1 in platelets (Lopez et al., 2012a). STIM1 phosphorylation has been detected at Tyr361 of the CAD/SOAR region in endothelial cells (Table 1.1). This phosphorylation is mediated by proline rich kinase 2 (Pyk2) following ER Ca^{2+} store depletion (Yazbeck et al., 2017). Interestingly, when this phosphorylation site was conservatively mutated (*i.e.* Tyr361Phe), STIM1 was able to oligomerize, but unable to recruit Orai1 subunits, thus preventing activation of the SOCE pathway (Yazbeck et al., 2017). It is noteworthy that Tyr361 forms self-stacking interactions in the CAD/SOAR crystal and CC1-CC2 NMR dimer interfaces. Thus, Tyr361 phosphorylation may affect the dimer architecture of the critical CAD/SOAR region, and thereby also affect interactions with Orai1.

Outside CAD/SOAR, STIM1 is phosphorylated by extracellular-signal-regulated kinase 1 and 2 (ERK1/2) at Ser575, Ser608 and Ser621, as observed in HEK293 cells (Pozo-Guisado et al., 2010) (Table 1.1). When ERK1/2 phosphorylation sites were mutated in STIM1 (*i.e.* Ser575Ala/Ser608Ala/Ser621Ala), the apparent binding affinity of Orai1 was reduced, thereby suppressing SOCE in HEK293 cells (Pozo-Guisado et al., 2010). Ser486 and Ser668 have also been identified as mitosis-specific phosphorylation sites (Smyth et al., 2009) (Table 1.1). Mitotic cells co-expressing Orai1 and fluorescently-tagged STIM1 Ser486Ala/Ser668Ala displayed higher levels of SOCE when compared to the same mitotic cells expressing wildtype STIM1 (Smyth et al., 2009). Thus, site-specific phosphorylation of STIM1 can either promote (Tyr361, (Ser575, Ser608, Ser621) or inhibit SOCE (Thr389, Ser486, Ser668), adding yet another layer of regulation to STIM1 function.

Cysteine *S*-glutathionylation is the covalent and reversible attachment of a tripeptide glutathione moiety to a cysteine thiol. *S*-Glutathionylation is commonly promoted under oxidative stress and is implicated in redox signaling (Dalle-Donne et al., 2009; Gallogly and Mieyal, 2007). In response to oxidative stress, STIM1 undergoes *S*-glutathionylation near the conserved luminal Ca^{2+}-sensing domain (Table 1.1). Specifically, after subjecting DT40 cells to oxidative stress, STIM1 was found to be *S*-glutathionylated at Cys56; moreover, the modification at this position constitutively activated Ca^{2+} entry via CRAC channels, independent of ER luminal Ca^{2+} concentrations

(Hawkins et al., 2010). While STIM1 is typically activated when intracellular ER Ca^{2+} levels are depleted, *S*-glutathionylation of Cys56 decreases the affinity of the immediately downstream canonical EF-hand for Ca^{2+}, thereby leading to STIM1 activation and SOCE even under replete ER luminal Ca^{2+} conditions (Hawkins et al., 2010).

N-linked glycosylation is the covalent attachment of an oligosaccharide to the amide nitrogen of an asparagine residue via a series of enzymatic reactions in the ER and Golgi. *N*-glycosylation is distinct from *O*-glycosylation which occurs on the side chain hydroxyl groups of Ser or Thr residues (Moremen et al., 2012). A minor fraction of STIM1 is located on the PM with the EFSAM domain directed into the extracellular space (Lopez et al., 2006; Manji et al., 2000; Spassova et al., 2006b; Williams et al., 2001; Zhang et al., 2005b). This cell surface targeting is mediated by *N*-glycosylation of Asn131 and Asn171 (Csutora et al., 2008; Czyz et al., 2009; Kilch et al., 2013; Manji et al., 2000; Mignen et al., 2007; Williams et al., 2001). Both these Asn residues are located within the EFSAM domain, and recent solution NMR approaches have shed light onto the structural mechanisms of regulation via modifications at these sites (Choi et al., 2017a; Choi et al., 2017c). Site-selective covalent attachment of glucose at Asn131 and Asn171 in isolated STIM1 EFSAM resulted in a reduced Ca^{2+} binding affinity, concomitant loss in stability and enhanced oligomerization propensity of the domain; moreover, the two simultaneous modifications were found to cause structural changes which pervaded through the EFSAM core (Choi et al., 2017a). Consistent with these structural and biophysical alterations to EFSAM, blocking *N*-glycosylation in full-length STIM1 via Asn131Gln/Asn171Gln results in diminished SOCE in HEK293 cells (Choi et al., 2017a). Interestingly, STIM1 can also *O*-link N-acetylglucosamine, resulting in suppressed SOCE (Zhu-Mauldin et al., 2012). The likely target of this modification is the STIM1 cytosolic domains given that *O*-glycosylation typically takes place in the cytosol or nucleus and the cytosolic region of STIM contains a sequence rich in Pro, Glu, Ser, Thr (Rogers et al., 1986) which has high *O*-linked modification propensity (Zhu-Mauldin et al., 2012).

S-Nitrosylation is the covalent addition of a NO moiety to a reduced cysteine residue. Typically, *S*-nitrosylation occurs under nitrosative stress, which can profoundly modify protein function and stability (Anand and Stamler, 2012; Benhar et al., 2006). STIMs are susceptible to *S*-nitrosylation near the conserved, Ca^{2+} sensing luminal EFSAM domain. Recent evidence demonstrates that *S*-

nitrosylation at Cys49 and Cys56 stabilizes the luminal domain of STIM1, thereby suppressing Ca^{2+} sensitivity and inhibiting SOCE activation (Gui et al., 2018; Zhu et al., 2018) (Table 1.1). While these results suggest that *S*-nitrosylation reduces SOCE, an *in vivo* model studying the effects *S*-nitrosylation has on cardiac hypertrophy has not yet been studied. Moreover, STIM2 is also a regulator of SOCE and plays a prominent role as a basal Ca^{2+} homeostatic feedback regulator (Brandman et al., 2007). However, the effects of *S*-nitrosylation on STIM2 stability and the resultant effects in either SOCE or basal Ca^{2+} regulation have not yet been investigated in any capacity.

1.6.1 *S*-Nitrosylation mechanism

Protein *S*-nitrosylation is a chemical redox reaction whereby a NO moiety oxidizes a reduced cysteine sulfhydryl group, yielding an *S*-nitrosothiol (S-NO) group (Fig. 1.5). Specifically, *S*-nitrosothiol formation is thought to occur via a recombination between a thiyl radical and NO or via oxidation of NO to N_2O_3 in the presence of an electron acceptor (Broniowska and Hogg, 2012).

NO is endogenously produced in humans from the breakdown of L-arginine via a group of enzymes termed NO synthases (NOS), which are activated by myriad biological signals and conditions. Three structurally and functionally distinct isoforms of NOS exist: neuronal NOS (nNOS), inducible NOS (iNOS) and endothelial NOS (eNOS). nNOS and eNOS are typically expressed constitutively and have a Ca^{2+}-dependent activity, while iNOS is only highly expressed after pro-inflammatory cytokine production and has a Ca^{2+}-insensitive activity. Collectively, these three NOS isoforms are able to produce NO under distinct cellular environments to regulate important pathophysiological functions, most notably within the cardiovascular system, wherein the importance of tightly regulated NO levels become apparent. Typically, NO production by iNOS is elevated in the myocardium of mammals after myocardial infarctions (Drexler et al., 1998; Feng et al., 1999). Interestingly, mice deficient in iNOS [*i.e.* iNOS (-/-)] have significantly lower mortality rates after myocardial infarctions induced by left coronary artery ligation when compared to wildtype iNOS mice (Feng et al., 2001), suggesting that this increased NO production contributes to myocardial dysfunction and mortality. Similarly, decreased NO production by eNOS is detrimental to the nascent mammalian heart, since mice deficient in eNOS [*i.e.* eNOS (-/-)] experience significantly increased postnatal mortality compared to wildtype eNOS mice due to atrial and ventricular septal defects, pulmonary congestion, and increased cardiomyocyte apoptosis (Feng et al., 2002).

Endogenous *S*-nitrosoglutathione (GSNO) is comprised of a glutathione (GSH) tripeptide covalently attached to a NO moiety, thereby serving as a biological reservoir of NO to regulate cellular levels of this compound within the body. GSNO reductase (GSNOR), a ubiquitously expressed enzyme, can catalyze the breakdown of GSNO using an electron donor (*i.e.* NADPH), to produce oxidized glutathione (*i.e.* GSSG) and an intermediate (*i.e.* GSNHOH), thereby lowering GSNO levels (Barnett and Buxton, 2017). Thus, cells have the protein machinery to produce NO, to store NO in the form of GSNO, and to tightly regulate cellular NO levels in order to control the level of protein *S*-nitrosylation in cells.

1.6.2 Effects of *S*-Nitrosylation

S-Nitrosylation plays an important role in the regulation of protein function. Interestingly, *S*-nitrosylation can mediate competing functions in a protein, depending on the specific Cys residue modified. After treatment with a specific agonist, *S*-nitrosylation of Ca^{2+}/CaM-dependent protein kinase II at Cys290 causes autonomous kinase activation, while *S*-nitrosylation at Cys273 reduces kinase activity (Erickson et al., 2015).

Hyperactive CRAC channels in mammalian cardiomyocytes can lead to pathological hypertrophy mediated by the transcription factor NFAT; however, recent evidence suggests that *S*-nitrosylation of STIM1 at Cys49 and Cys56 mediated by nNOS inhibits STIM1-mediated I_{CRAC} in mammalian cardiomyocytes (Gui et al., 2018). Interestingly, adenoviral nNOS infection inhibits phenylephrine induced hypertrophy in cardiomyocytes (unpublished data; Feng laboratory). While *S*-nitrosylation of human STIM1 at Cys49 and Cys56 were shown to suppress function and attenuate pathological cardiomyocyte hypertrophy, the effects of human STIM2 *S*-nitrosylation at the conserved Cys53 and Cys60, as well as the unique Cys15 in health and disease remains unknown.

Table 1.1 Summary of detected post-translation modifications on STIM1.

Modification	Location on STIM1[a]	Cellular localization	Effect on SOCE	References
S-glutathionylation	Cys56 – N-terminal variable	ER lumen	enhances	(Hawkins et al., 2010)
N-glycosylation	Asn131 – SAM domain	ER lumen and extracellular space	enhances	(Choi et al., 2017a; Csutora et al., 2008; Czyz et al., 2009; Kilch et al., 2013; Manji et al., 2000; Mignen et al., 2007; Williams et al., 2001)
N-glycosylation	Asn171 – SAM domain	ER lumen and extracellular space	enhances	(Choi et al., 2017a; Csutora et al., 2008; Czyz et al., 2009; Kilch et al., 2013; Manji et al., 2000; Mignen et al., 2007; Williams et al., 2001)
O-glycosylation	Ser/Thr – P/S	cytosol	suppresses	(Zhu-Mauldin et al., 2012)
phosphorylation	Tyr361 – SOAR/CAD	cytosol	enhances	(Lopez et al., 2012a; Yazbeck et al., 2017)
phosphorylation	Thr389 – SOAR/CAD	cytosol	suppresses	(Thompson and Shuttleworth, 2015; Thompson et al., 2018)
phosphorylation	Ser486 – OASF, Ser668 – P/S	cytosol	suppresses	(Smyth et al., 2009)
phosphorylation	Ser575, Ser608, Ser621 – P/S	cytosol	enhances	(Pozo-Guisado et al., 2010)
S-nitrosylation[b]	Cys49, Cys56 – N-terminal variable	ER lumen	suppresses	(Zhu et al., 2018)

[a] See Fig. 1.2 for relative location in sequence space and on STIM1 domain architecture.

[b] Information not included in original publication.

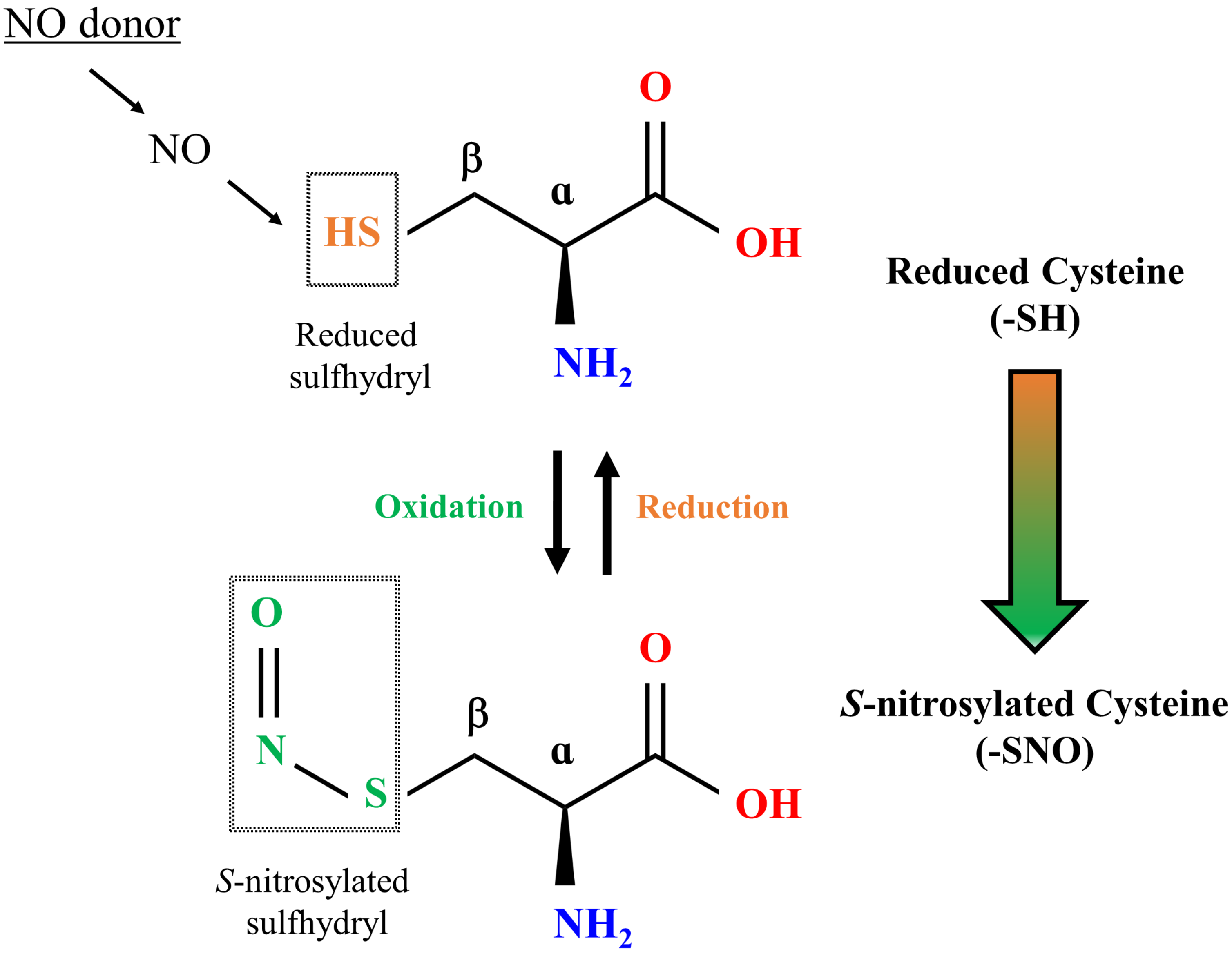

Fig. 1.5. Schematic mechanism by which cysteine residues undergo *S*-nitrosylation in the presence of NO donors. NO molecules produced by various NO donors or NOS enzymes can chemically react with the sulfhydryl group on the side chain of a cysteine residue to form *S*-nitrosocysteines under various oxidizing conditions. The inherent chemical lability associated with this covalent bond results in an equilibrium between reduced and *S*-nitrosylated states, which is dependent on the environment. The atoms directly modified by *S*-nitrosylation are highlighted in dashed boxes. The atoms making up the carboxylate and amino groups of the Cys are coloured in red and blue, respectively.

1.7 Rationale

The *STIM2* gene first appeared in the *Euteleostomi* lineage (*i.e.* bony vertebrae), most likely due to a duplication of an ancestral *STIM* gene (Cai, 2007; Williams et al., 2001). Despite the high sequence similarity between STIM homologs, many differences exist, underlying the unique molecular and functional properties of STIM2. Recently, two Cys residues within the N-terminal domain of STIM1 (*i.e*. Cys49 and Cys56) were shown to be important functional regulatory sites through post-translational modifications. Specifically, *S*-nitrosylation of these residues suppresses Ca^{2+} sensitivity and inhibits SOCE (Zhu et al., 2018), whereas *S*-glutathionylation of Cys56 constitutively activates STIM1 mediated SOCE (Choi et al., 2017b). While these two Cys residues are conserved between STIM vertebrate homologs (*i.e.* STIM2 Cys53 and Cys60), STIM2 contains an additional and non-conserved Cys within its N-terminal domain (*i.e.* Cys15). Interestingly, this unique Cys is present in the earliest known *STIM2*-containing organism (*i.e. Danio rerio*; zebra fish) (Fig. 1.3B), highlighting the evolutionary importance of this residue. As a result, the Cys15 residue may serve as an additional post-translational modification site whereby *S*-nitrosylation affects the structure and function of STIM2, underlying its unique function as a basal Ca^{2+} homeostatic feedback regulator.

I posit that the stability and function of STIM2 are also regulated by luminal domain *S*-nitrosylation at Cys15, Cys53, and Cys60, and that *S*-nitrosylation of the unique Cys15 residue contributes to distinct functions between the STIM homologs. Thus, the aim of my study is to characterize the biophysical, structural and functional effects of STIM2 luminal domain *S*-nitrosylation to enhance our understanding of basal Ca^{2+} regulation and the role of STIM2 in health and disease.

1.8 Hypothesis and objectives

Hypothesis:

I hypothesize that *S*-nitrosylation of STIM2 near the luminal Ca^{2+} sensing domain affects its biophysical properties including structure, stability, oligomerization and activation. Thus, I posit that *S*-nitrosylation of STIM2 affects SOCE and basal Ca^{2+} homeostasis in mammalian cells.

Aim 1: To determine the effect of *S*-nitrosylation on the biophysical and structural properties of the full luminal domain and variable N-terminal region of human STIM2.

The luminal domain of *H. sapiens STIM2* (NCBI GeneID 57620) (*i.e.* residues 15-217), comprised of the Ca^{2+}-sensing EFSAM domain as well as the far N-terminal region containing the three cysteine residues available for *S*-nitrosylation, was cloned into a pET-28a vector. STIM2 has 3×cysteine residues (*i.e.* Cys15, Cys53 and Cys60) compared to the 2×cysteine residues in the luminal domain of STIM1 (*i.e.* Cys49 and Cys56), and thus has an additional potential *S*-nitrosylation site that may contribute to the differential regulation of Ca^{2+} flux by STIM2. As such, site-directed mutagenesis was applied to generate single, double and triple Cys to Ser STIM2 luminal domain mutants. Wildtype and mutant constructs were expressed in *E. coli* and purified using metal-affinity and size exclusion chromatography. Moreover, the variable N-terminal region of *H. sapiens STIM2* (NCBI GeneID 57620) (*i.e.* residues 15-66) containing the three modifiable Cys residues was cloned into a pGEX-4T1 vector, expressed in *E. coli* and purified using affinity and size exclusion chromatography. Purified STIM2 luminal domain (*i.e.* residues 15-217) and variable N-terminal region (*i.e.* residues 15-66) proteins were exchanged in a buffer with the excess NO donor GSNO to study the effects of *S*-nitrosylation compared to the native protein exchanged into dithiolthreitol (DTT) buffer. A wide range of spectroscopic techniques were applied to characterize the biophysical and structural properties of these proteins under reducing and *S*-nitrosylating conditions.

Aim 2: To elucidate the effect of *S*-nitrosylation on the functional properties of full-length STIM2 in mammalian cells.

The full-length sequence of wildtype *H. sapiens STIM2* (NCBI GeneID 57620) was cloned into a pCMV6 mammalian expression vector with a constitutive promoter. Site-directed mutagenesis was used to generate Cys15Ser single-mutant and Cys15Ser/Cys53Ser/Cys60Ser triple-mutant constructs. HEK293T cells were co-transfected with Orai1 and different combinations of wildtype and mutated STIM2 constructs, and fura-2-AM ratiometric fluorimetry was used to probe basal Ca^{2+} and SOCE. Overnight GSNO incubation was used to study the effect of *S*-nitrosylation on STIM2 function in the full-length molecular context.

Chapter 2: Methods

2.1 Generation of recombinant vectors encoding human STIM2

In order to assess the biophysical properties associated with STIM2 variable N-terminal region *S*-nitrosylation, the full luminal region (*i.e.* residues 15-217) of *Homo sapiens* STIM2 (NCBI accession NP_065911.3) containing the region with three modifiable Cys residues available for *S*-nitrosylation (*i.e.* Cys15, Cys53 and Cys60) together with the Ca^{2+}-sensing EFSAM domain (*i.e.* residues 67-204), was cloned into a pET-28a vector. Additionally, a pCMV6 vector encoding full length *H. Sapiens* STIM2 (*i.e.* residues 1-746) fused to monomeric cherry fluorescent protein (mCh) (*i.e.* pCMV6-mCh-STIM2) (Chung et al., 2018; Stathopulos et al., 2009; Zheng et al., 2011a) was used in the present study to determine the functional properties associated with this site-specific post-translational modification *in vitro*.

Furthermore, to uncover the importance that each *S*-nitrosylated Cys has on the biophysical and functional properties of STIM2, polymerase chain reaction (PCR)-mediated -site directed mutagenesis using either the pET-28a or pCMV6-mCh wildtype STIM2 vectors and mutagenic primers (detailed in Table 2.1) were used to mutate various combinations of Cys residues to Ser (Table 2.2). For the mutagenesis, either ~250 ng of the forward or reverse primers (Table 2.1) were added to a 20 µL dH_2O solution containing 1× of the 5× High Fidelity (HF) buffer (Thermo Fischer Scientific), 2% (v/v) DMSO, ~100 ng of the vector template, 10 mM dNTPs, and 1 µL (0.02 units/µL) Phusion DNA polymerase (Thermo Fischer Scientific). The two solutions were first subjected to 10 PCR amplification cycles in a LifeECO Thermocycler (BioER) using parameters listed in Table 2.3. Upon completion, the resultant amplicons from both solutions were combined, and the final mixture was subjected to another 25 amplification cycles using the parameters listed in Table 2.3. The final amplicon products, as well as equal amounts of control template DNA and a GeneRuler 1kb Plus DNA ladder (ThermoFisher), were separated on a 1.5% (w/v) agarose gel prepared in 0.5× TRIS, acetic acid, ethylene diamine tetra acetic acid (TAE) running buffer electrophoresed at 125 V for 60 minutes. Following electrophoresis, the gel was submerged in 0.5 µg mL^{-1} ethidium bromide (EB) solution and placed on a platform shaker for 30 min. The gel was subsequently visualized under UV light at 302 nm. Amplification success was determined by a higher relative intensity of the PCR product compared to control, template DNA. 15 units of Dpn1

(New England BioLabs) was added to the remaining PCR product (~25 μL) and incubated for 3 hours at 37 °C in an incubator to digest the original methylated template DNA. To transform the mutagenized vector into bacteria, 15 μL of the PCR product was incubated with 100 μL competent DH5α *E. coli*, incubated on ice for 1 hour and subsequently heat shocked at 42 °C for 45 seconds. The heat shocked cells together with the amplified digestion product were subsequently transferred into 900 μL of Luria-Bertani (LB) broth media and incubated for 1.5 hours at 37 °C with constant shaking at 190 revolutions per minute (rpm). After this time, the cells were pelleted by centrifugation at 7,500 ×g for 5 min and resuspended in ~100 μL of LB. These resuspended cells were plated on an agar plate containing 60 μg/mL kanamycin, and incubated overnight in an air incubator at 37 °C. The next day, colonies were selected and grown overnight in 5 mL LB liquid culture at 37 °C and 190 rpm. Finally, the mutant plasmids were isolated the next day using the Presto Mini Plasmid Kit (GeneAid) according to the manufacturer's protocol. Isolated plasmids were subsequently sequenced at the Robarts DNA Sequencing facility (London, ON, CAN) using the T7 reverse terminator primer to confirm the mutagenesis at the nucleotide level.

Finally, to study the structure of the variable N-terminal region of STIM2 (*i.e.* residues 15-66), the DNA encoding this region was subcloned from a pET-28a-STIM2 vector containing the full luminal domain (*i.e.* residues 15-217) into a pGEX-4T1 (GE Heathlcare) recombinant vector using BamHI and EcoRI restriction sites. In order to obtain the STIM2 15-66 insert, a 150 μL PCR mixture in dH_2O was prepared, which contained 1× of the 5× HF buffer (Thermo Fischer Scientific), ~30 ng of pET-28a-STIM2 15-217 template, ~500 ng each of the forward and reverse primer (Table 2.1), 10 mM dNTPs, and 1μL (0.02 units/μL) Phusion DNA polymerase (Thermo Fischer Scientific). The forward and reverse primers had BamHI and EcoRI restriction sites incorporated at the 5' and 3' ends, respectively. The 150 μL PCR mixture was divided in equal volumes and amplified for 35 cycles using a thermal cycler (Eppendorf Mastercycler) as described in Table 2.3. The final PCR products were electrophoresed on a 1.5% (w/v) agarose gel as described above for the mutagenesis. The agarose gel was visualized under UV light at 302 nm and the amplicon band size (~159 base pairs) was assessed by comparing the fragment size to a Gene Ruler 1kb Plus DNA ladder (Thermo Fischer Scientific). The corresponding fragment was excised from the gel, transferred into a separate Eppendorf tube, and the DNA was subsequently isolated from the agarose gel using the GeneFlow Gel/PCR purification kit according to the manufacture's protocol.

Compatible sticky end overhangs were generated by double digestions of the isolated STIM2 15-66 insert and target pGEX-4TI wildtype STIM2 15-217 vector using BamHI and EcoRI restriction enzymes. The first digestion mixture was prepared using ~500 ng of the STIM2 15-66 insert, 4 μL Cut Smart Buffer, and 0.5 μL of each restriction enzyme, while the second digestion mixture was prepared using ~1 μg pGEX-4TI vector, 2 μL Cut Smart Buffer, and 1 μL of each restriction enzyme in 8.5 μL dH_2O. Each digestion mixture was incubated at 37 °C overnight in an incubator. The following day, both digested samples were separated on an agarose gel, stained with ethidium bromide, and visualized under UV light as described above. The digested DNA bands from both the STIM2 15-66 insert and the pGEX-4TI vector with compatible sticky ends were excised from the agarose gel using the GeneFlow Gel/PCR purification kit according to the manufacture's protocol.

In order to ligate the digested STIM2 15-66 insert into the pGEX-4T1 recombinant vector, 4.5 μL dH_2O, 3.0 μL of the digested pGEX-4TI vector, 10 μL of the digested STIM2 15-66 insert and 2 μL of 2× T4 DNA ligation buffer (New England Biolabs) were combined into an Eppendorf tube. The mixture was subsequently heated at 42 °C for 2 minutes, chilled on ice for 1 minute, and supplemented with 1 μL T4 DNA ligase (New England Biolabs). The ligation reaction was carried out by placing the mixture in a water bath at 16 °C for ~16 hours. The ligation product was transformed into DH5α *E. coli* using a similar transformation approach described above for the mutagenesis protocol, and the cells that successfully took up the plasmid were selectively grown on agar plates containing 100 μg/mL ampicillin antibiotic.

The resultant transformed colonies were screened for the STIM2 15-66 insertion in the pGEX-4TI recombinant vector by suspending individual colonies in 20 μL dH_2O. Afterwards, 5 μL of this solution was added to a 20 μL dH_2O mixture containing 10 μL 2× Taq Frogga Master Mix (Froggabio) and ~250 ng each of pGEX forward and reverse primers. The entire mixture was amplified in a thermocycler for 25 cycles using the parameters detailed in Table 2.3. The final

PCR product was electrophoresed on an agarose gel, stained with ethidium bromide and visualized under UV light as described above. Positive colonies that indicated the expected band size (~5000 bp) using the PCR screening approach were then grown in a 5 mL LB broth solution containing 100 µg/mL ampicillin overnight at 37°C in an incubator shaking at 200 rpm. The next day, pGEX-4TI plasmids containing the STIM2 15-66 insert were isolated from the liquid cultures using the Presto Mini Plasmid kit (Geneaid) as per the manufacturer's protocol. DNA sequencing (Robarts DNA Sequencing Facility, London, ON) using the pGEX forward primer confirmed that the STIM2 15-66 insertion was in the correct reading frame in the pGEX-4T1 recombinant vector.

Table 2.1. Oligonucleotide primers (Sigma-Aldrich, St. Louis, MO) used in this study.

Primer	**Sequence**
pET-28a STIM2 15-217 Cys15Ser [a]	5’-GGCAGCCATATGGCTAGCAGCGAGCTTGTGCCCCGGCAC-3’
	5’-GTGCCGGGGCACAAGCTCGCTGCTAGCCATATGGCTGCC-3’
pCMV6-mCh STIM2 1-746 Cys15Ser [b]	5’-GAGCTGTACAAGGGTACCAGCGAGCTTGTGCCCCGGCAC-3’
	5’-GTGCCGGGGCACAAGCTCGCTGGTACCCTTGTACAGCTC-3’
pET-28a STIM2 15-217 Cys53Ser [a]	5’-CTCATGACAGATCCCAGCATGTCACTGAGTCCA-3’
	5’-TGGACTCAGTGACATGCTGGGATCTGTCATGAG-3’
pET-28a STIM2 15-217 Cys60Ser [a]	5’-TCACTGAGTCCACCAAGCTTTACAGAAGAAGAC-3’
	3’-GTCTTCTTCTGTAAAGCTTGGTGGACTCAGTGA-5
mCherry [c]	5’-GTTGGACATCACCTCCCACAACG-3’
T7 Terminator [c]	5’-GCTAGTTATTGCTCAGCGG-3’
pGEX-4T1 STIM2 15-66 Insertion [d]	5’ GCCATATGGGATCCTGCGAGCTTGTGCCCCGGCACCTCCG-3’
	5’-AATCTGTCGAATCCCTAAAAGCATGGTGGACTCAGTGACATGC-3’
pGEX Forward [c,e]	5’- GGGCTGGCAAGCCACGTTTGGTG-3’
pGEX Reverse [e]	3’- CCGGGAGCTGCATGTGTCAGAGG-5’

[a] Mutagenesis primer for wildtype pET-28a STIM2 15-217

[b] Mutagenesis primer for wildtype pCMV6 STIM2 1-746

[c] Sequencing primer

[d] Subcloning primer for STIM2 15-66

[e] Screening primer for pGEX-4T1 STIM2 15-66

Table 2.2. Cys to Ser mutation strategy used in this study.

Vector:	**Construct:**	**DNA used for SDM-PCR Construct generation:** Template:	Mutagenic Primers (Table 2.1)
pET-28a[a]	STIM2 15-217 Wildtype	---	---
	STIM2 15-217 Cys15Ser	STIM2 Wildtype	pET-28a STIM2 15-217 Cys15Ser Primers
	STIM2 15-217 Cys53Ser	STIM2 Wildtype	pET-28a STIM2 15-217 Cys53Ser Primers
	STIM2 15-217 Cys60Ser	STIM2 Wildtype	pET-28a STIM2 15-217 Cys60Ser Primers
	STIM2 15-217 Cys53/60Ser	STIM2 Cys53Ser	pET-28a STIM2 15-217 Cys60Ser Primers
	STIM2 15-217 Cys15/53/60Ser	STIM2 Cys53/60Ser	pET-28a STIM2 15-217 Cys15Ser Primers
pCMV6[b]	STIM2 1-746 Wildtype	---	---
	STIM2 1-746 Cys15Ser	STIM2 1-746 Wildtype	pCMV6-mCh-STIM2 1-746 Cys15Ser Primers
	STIM2 1-746 Cys15/53/60Ser	STIM2 1-746 Cys15Ser	pCMV6-mCh-STIM2 1-746 Cys53Ser & Cys60Ser Primers

[a] Primers acquired from GeneScript
[b] Primers acquired from Sigma Aldrich

Table 2.3. PCR amplification parameters used in LifeECO (BioER) thermocycler

		pET-28a STIM2 15-217 mutagenesis		pCMV6 STIM2 1-746 mutagenesis		pGEX-4T1 STIM2 15-66 subcloning		pGEX-4T1 STIM2 15-66 Screening	
		10 Cycles + 25 Cycles		10 Cycles + 25 Cycles		35 Cycles		35 Cycles	
		Temp (°C)	Time (sec)	Temp (°C)	Time (sec)	Temp (°C)	Time (sec)	Temp (°C)	Time (sec)
Initial Denaturation		98	35	98	35	98	30	98	30
Cycles	Denaturation	98	10	98	10	98	10	98	10
	Annealing	54-55	30	53-55	30	54	30	54	30
	Extension	72	180	72	180	72	30	72	30
Final Extension		72	330	72	330	72	30	72	30
Storage		4	∞	4	∞	4	∞	4	∞

2.2 Protein expression and purification

2.2.1 Expression and purification of wildtype and mutant STIM2 15-217

The pET-28a vector harboring the wildtype STIM2 luminal domain corresponding to residues 15-217, hereafter named STIM2 15-217, was transformed into BL21(DE3) *E. coli* using a similar transformation approached described in section 2.1, and cells that successfully took up the plasmid were selectively grown on agar plates containing 60 μg/mL kanamycin overnight at 37 °C. The next day, one isolated individual colony was lifted from the kanamycin agar plate, inoculated into a 65 mL LB mixture containing 60 μg/mL kanamycin and grown overnight at 200 rpm and 37 °C. The following day, 10 mL of the LB culture was added individually to 6× 4L sterile flasks containing 1L of LB media and 60 μg/mL kanamycin. The 6× 4L flasks each containing the liquid culture and kanamycin antibiotics were subsequently grown in a New Brunswick ™ Excella ® E25/E25R incubator shaker at 37 °C and 200 rpm until the optical density (OD) at 600 nm reached a range of ~0.6-0.8. Once within the optimal OD range, each of the 6 flasks was supplemented with a final concertation of 300 μM of isopropyl β-D-1-thiogalactopyranoside (IPTG) to induce protein expression from the recombinant pET-28a vector, as IPTG is a lactose analog which binds to a lac repressor also encoded within the vector. To minimize protein degradation and increase protein expression, the temperature was dropped to 25 °C and incubated overnight at 190 rpm, respectively. The following morning, the J2-21M Induction drive centrifuge equipped with a JA10 rotor (Beckman) was used to collect the BL21 cells via a centrifugation at 10,000 ×g at 4 °C for 40 minutes. Immediately after the centrifugation, the cell pellets were collected, pooled together (~15 mL total wet cells) and stored at -80 °C until needed for protein purification.

To purify the STIM2 15-217 protein, the ~5 mL bacterial cell pellets were thawed and resuspended in ~40 mL of 6 M guanidine hydrochloride, 20 mM Tris-HCl (pH=8) and 5 mM β-mercaptoethanol (BME). The mixture was physically homogenized with using a 10-mL transfer pipette. To ensure proper release of the protein from inclusion bodies, the homogenized mixture was rotated in a hybridization oven at room temperature for 90 minutes. Moreover, in order to separate the insoluble cell debris from the soluble protein supernatant, the homogenized mixture was centrifuged using a JA20 rotor in a J2-21M Induction drive centrifuge at 12,000 ×g and 8°C for 40 minutes. The clarified lysate corresponding to the supernatant was collected immediately after the centrifugation, and subsequently rotated in a hybridization oven for 90 minutes after supplementing with 500 μL of 50% (v/v) nickel-nitrilotriacetic acid (Ni^{2+}-NTA) agarose HisPur bead slurry (ThermoFischer Scientific) solution. Gravity filtration using a gravity flow protein purification column (Bioscience) was used to retain the Ni^{2+}-NTA beads bound to the N-terminally fused hexahistidine (6× His)-tag of the STIM2 15-217 protein. The protein bound beads retained in the gravity column were washed 3× with a 10 mL solution of 6 M Urea, 20 mM Tris-HCl (pH=8), and 5 mM BME, and eluted 7× in 2 mL aliquots with the same mixture supplemented with 300 mM imidazole, a binding competitor of the 6×His-STIM2 15-217 for the Ni^{2+}-NTA beads. In order to ensure maximal displacement of the 6×His-tagged STIM2 15-217 protein from the Ni^{2+}-NTA beads, each 2 mL aliquot was incubated in the gravity column for 2 minutes before flow through and collection. Separating the aliquots of each elution on a 15% (w/v) SDS-PAGE gel followed by Coomassie Brilliant Blue (Thermo Fischer Scientific) staining confirmed the presence of the protein (Fig 2.1A).

Elution fractions containing the protein of interest were pooled together into a 3.5 kDa molecular weight dialysis membrane (BioDesign) and submerged into a 1 L protein refolding buffer containing 20 mM TRIS-HCl (pH=8), 300 mM NaCl, 1 mM dithiothreitol (DTT) and 5 mM $CaCl_2$. In order to ensure homogeneous exchange between the buffers, a magnetic stir bar was used to rotate the submerged dialysis membrane for ~18 hours at 4 °C. Following the protein refolding, ~1 unit of bovine thrombin (BioPharm Laboratories, Inc.) was added per ~ 1 mg of STIM2 15-217 directly into the dialysis membrane and gently stirred overnight at 4 °C in the protein refolding buffer to cleave the N-terminally attached 6×His-tag. The completeness of thrombin cleavage was determined by comparing the migration of pre- and post-thrombin protein samples separated on a 15% (w/v) SDS-PAGE gel followed by Coomassie blue staining for visualization (Fig. 2.1B). After confirmation of the His-tag cleavage, 100 μM of 4-(2aminoethyl) benzenesulfonyl fluoride (AEBSF) was added to protein solution to stop the thrombin enzyme activity.

Size-exclusion chromatography (SEC) using a HiLoad Superdex S200 20/60 PG column connected to an AKTA Pure system (GE Healthcare) was used to achieve a STIM2 15-217 protein purity >95% by separating impurities/contaminants by molecular weight. Prior to injecting the refolded STIM2 15-217 protein, the column was washed with water, and subsequently equilibrated with a filter sterilized running buffer composed of 5 mM $CaCl_2$, 20 mM TRIS-HCl (pH=8), 1 mM DTT, and 150 mM NaCl. The protein elution was monitored by UV absorbance at 280 nm (UV 280) and collected in1 mL fractions on a 96× deep well plate (Fig. 2.2A). The fractions that showed a high UV 280 absorbance were separated on a 15% (w/v) SDS-PAGE gel and stained with Coomassie blue to confirm the presence and purity of STIM2 15-217 (Fig. 2.2B). Elutions that showed a single band at the theoretical molecular weight of the STIM2 15-217 protein (~22.4 kDa) were pooled together, flash frozen using liquid nitrogen, and stored at -80 °C until use.

STIM2 15-217 single mutants Cys15Ser, Cys53Ser, Cys60Ser, double mutant STIM2 15-217 Cys53Ser/Cys60Ser, and triple mutant Cys15Ser/Cys53Ser/Cys60Ser proteins were expressed and purified as described above for STIM2 15-217 wildtype protein. Protein concentrations were estimated using UV extinction coefficients at 280 nm ($\varepsilon_{280\text{ nm}}$). The extinction coefficients were $\varepsilon_{280\text{ nm}}$ = 1.2944 mg/mL for wildtype STIM2 15-217, $\varepsilon_{280\text{ nm}}$ = 1.2953 mg/mL for Cys15Ser, Cys53Ser or Cys60Ser single mutant STIM2 15-217, $\varepsilon_{280\text{ nm}}$ = 1.2961 mg/mL for Cys53Ser/Cys60Ser double mutant STIM2 15-217, and $\varepsilon_{280\text{ nm}}$ = 1.2970 mg/mL for Cys15Ser/Cys53Ser/Cys60Ser triple mutant STIM2 15-217 proteins.

For the preparation of protein for use in solution nuclear magnetic resonance (NMR) spectroscopy experiments, the wildtype STIM2 15-217 protein was uniformly ^{15}N-labelled by expression in 1 L minimal M9 media containing 42 mM Na_2HPO_4, 22 mM KH_2PO_4, and 8.6 mM NaCl supplemented with 0.2% (w/v) D-glucose, 100 μM $CaCl_2$ 50 μM thiamine, 1 mM $MgSO_4$, 1 μg/mL biotin and 1 mg/mL ^{15}N-NH_4Cl as the sole nitrogen source. The M9 salts were sterilized by autoclaving, while the supplement mixture was filter sterilized into the 1 L of M9 salts using one 0.2 μm syringe filter (Millipore). Prior to using the supplemented M9 media, one STIM2 15-217 BL21(DE3) *E. coli* transformant was inoculated in 30 mL LB media and grown overnight for ~18 hours at 37 °C and 190 rpm. The bacterial cell pellet from this 30 mL starter culture was isolated via centrifugation 3,500 ×g for 30 minutes at 20 °C. The LB medium was decanted and the bacterial cells were re-suspended in 10 mL of M9 media and subsequently transferred into the M9 media containing the previously mentioned supplements. The remaining expression and purification steps of the ^{15}N-labelled protein were conducted exactly as described for the unlabelled protein.

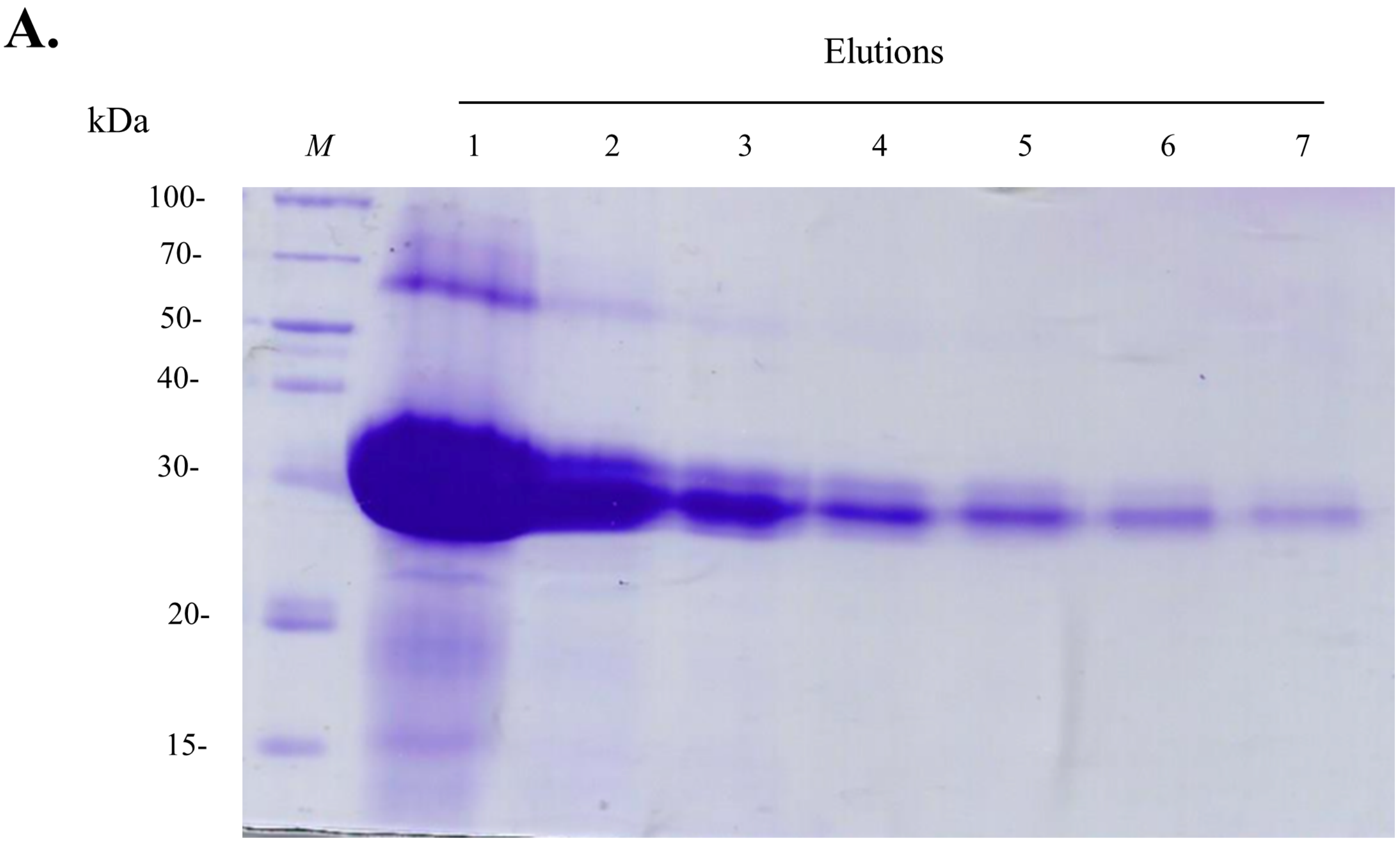

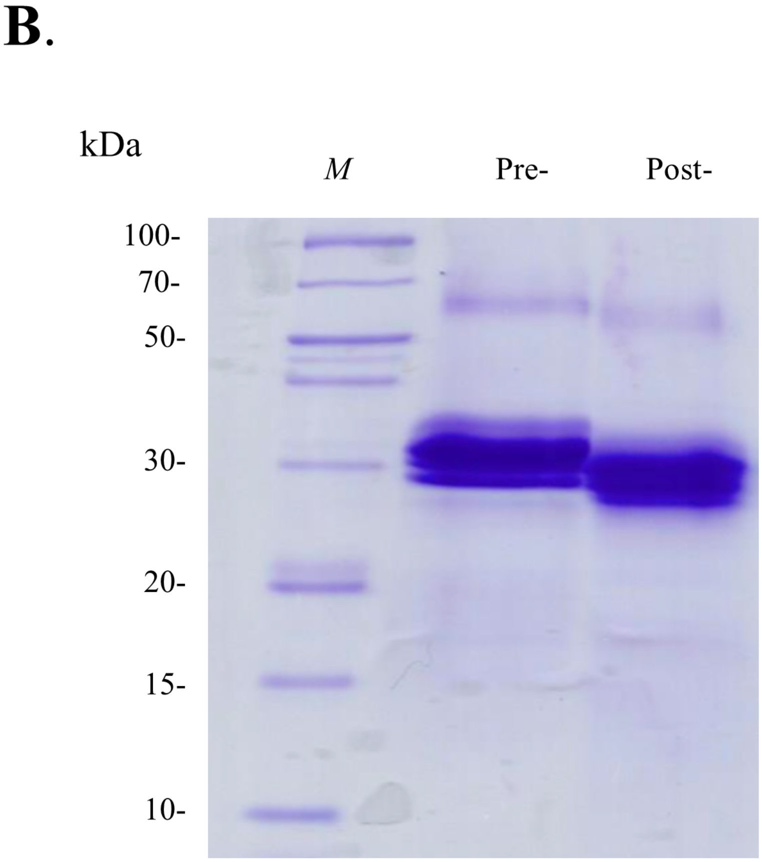

Fig. 2.1. Coomasise Brilliant Blue staining of STIM2 15-217 protein on a 15 % (w/v) SDS-PAGE gel. A. Wildtype 6×His-STIM2 15-217 (~26 kDa) protein elution fractions (1-7) from Ni-NTA resin using 300 mM imidazole. **B.** Pre- and post-thrombin cleaved samples, which indicate protein samples with and without the 6×-His tag corresponding to ~26 kDa and ~24 kDa, respectively. *M* denotes PageRuler Broad Range Unstained Protein Ladder (Thermo Fisher Scientific).

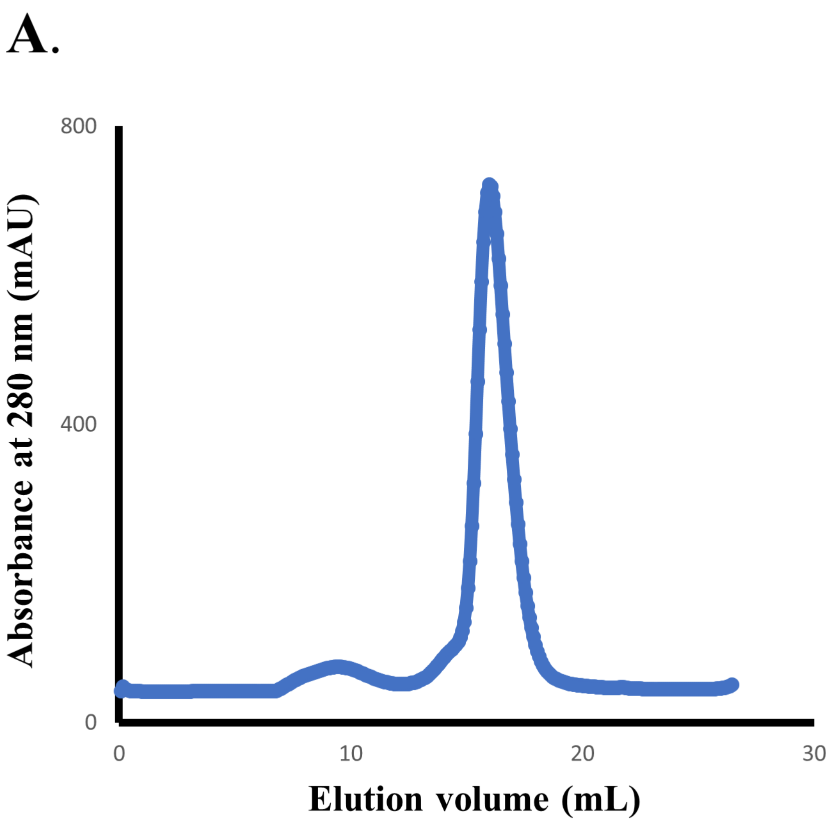

Fig. 2.2. Size Exclusion chromatography (SEC) elution profile of STIM2 15-217. SEC was performed using Superdex 200 10/300 GL column (GE Healthcare, Inc.). **A.** Elution profile is based on absorbance at 280 nm (A_{280}) in arbitrary milli Absorbance Units (mAU) as a function of elution volume. **B.** Coomassie Brilliant Blue staining of STIM2 15-217 (~24 kDa) on a 15 % (w/v) SDS-PAGE gel of elution fractions corresponding to volumes 11-19 mL. Yellow box indicates fractions collected for analyses. *M* denotes PageRuler Broad Range Unstained Protein Ladder.

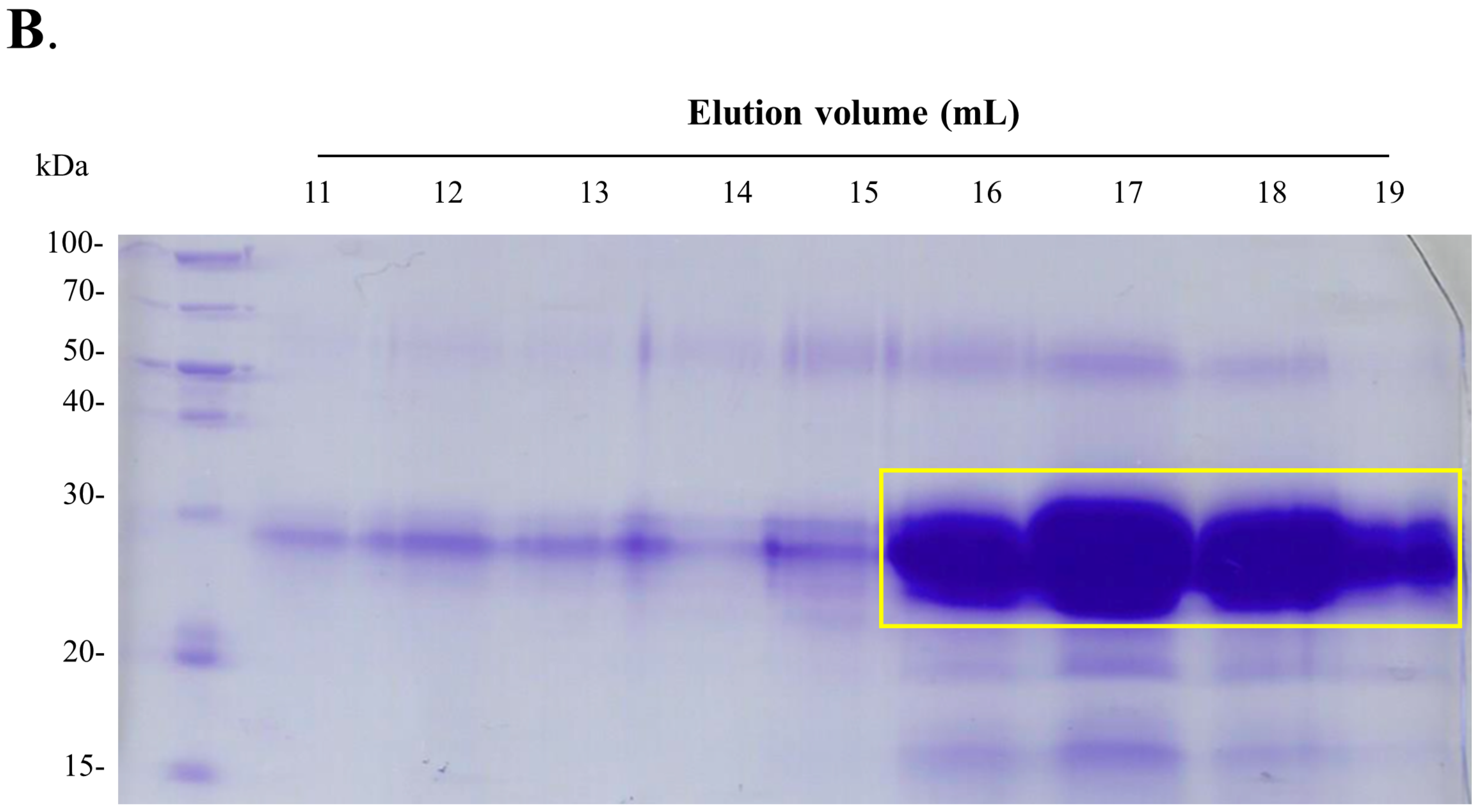

2.2.2 Expression and purification of wildtype STIM2 15-66

The pGEX-4TI vector harboring the wildtype STIM2 variable region corresponding to residues 15-66, hereafter named STIM2 15-66, was transformed into BL21(DE3) *E. coli* cells described for the pET-28a STIM2 15-217 recombinant vector, with the exception that 100 μg/mL ampicillin was used as the selection pressure. One colony was picked, inoculated into 30 mL LB media containing 100 μg/mL ampicillin and grown overnight at 37 °C and 190 rpm constant shaking. The following day, 10 mL of the bacterial culture was added to 1 L of LB supplemented with 100 μg/mL ampicillin, and grown at 37 °C and 190 rpm until the OD at 600 nm reached ~0.6-0.8. Subsequently, a final concentration of 300 μM of IPTG was added to the culture to induce recombinant protein expression under control of the lac operon, and the temperature was dropped to 30 °C. The cells were grown for an additional 4 hours with 190 rpm constant shaking under these conditions and subsequently collected into cell pellets by centrifugation as described previously in section 2.2.1.

Since the pGEX-4TI vector expresses recombinant proteins as fusions with glutathione-*S*-transferase, the wet bacterial cell pellets were purified using GST Sepharaose beads (Genescript) as described in the manufacturer's protocol. In brief, ~5 mL cell pellets were suspended in a 45 mL wash buffer containing 1× phosphate buffer saline (PBS) and 1 mM DTT. To ensure the complete homogenization of cells, the cell mixture was sonicated on ice at 40 % power using the Fischer Sonic Dismembrator Model 150 (Thermo Fischer Scientific) for 10 minutes in 3 second on/off cycles. After sonication, 0.2 % (v/v) triton X-100 was added to the sonicated mixture. The resultant homogenized mixture was rotated for 90 minutes at 4 °C in order to maximize release of the GST-STIM2 15-66 fusion into solution. A JA20 rotor in a J2-21M Induction drive centrifuge was used to separate the insoluble cell debris from the soluble GST-STIM2 15-166 by centrifugation at 12,000 ×g and 8 °C for 40 minutes. The supernatant was immediately collected and supplemented with a 1 mL solution of 50% (v/v) GST beads pre-equilibrated with 1× PBS and 1 mM DTT. The resultant solution was rotated for another 90 minutes at 4 °C in order to promote maximal binding of the GST beads to the GST-STIM2 15-66 fusion. Gravity filtration using a gravity flow protein purification column (Bioscience) was used to retain the GST beads bound to GST-STIM2 15-66 peptide. The collected beads were subsequently washed with 3× 10 mL wash buffer containing 1× PBS and 1 mM DTT. After washing, 15 mL of 20 mM TRIS-HCl (pH=7.5), 150 mM NaCl, 1 mM DTT and ~5 units of thrombin per ~1 mg of GST-STIM2 15-66 was added to the closed gravity column. The closed column containing the GST beads and captured GST-STIM2 15-66 was rocked overnight for ~18 hours at 4 °C in order to promote thrombin cleavage and release of the STIM2 15-66 peptide. After rocking in this cold environment, the STIM2 15-66 peptide was eluted from the column, leaving behind the GST bound to the beads. Subsequent washes of the GST beads with 3× 1 mL wash buffer was used to collect residual peptide. Pre- and post-thrombin solutions were separated on a 15% (w/v) SDS-PAGE gel and visualized by silver staining to confirm the presence of the peptide. The samples containing the STIM2 15-66 peptide were pooled together and further purified using SEC as described in 2.2.1, this time by monitoring UV absorbance at 215 nm (UV215) and using a running buffer of 50 mM Na_2HPO_4 and 1 mM DTT (Fig. 2.3A). The fractions that showed a high UV215 absorbance were separated on a 15% (w/v) SDS-PAGE gel, silver stained (according to manufacturer's protocol; Thermo Fisher Scientific), and visualized to confirm for the purity of STIM2 15-66 peptide (Fig. 2.3B). Elutions that showed a band migrating at the theoretical molecular weight of the STIM2 15-66 peptide (~3.2 kDa) were pooled together, flash frozen using liquid nitrogen, and stored at -80 °C until use in experiments.

For protein concentration estimates of STIM2 15-66, a bicinchoninic acid assay (BCA) kit was used according to the manufacturer's protocol. Bovine serum albumin (Thermo Fisher Scientific) was used to generate a standard curve for the protein concentration estimate.

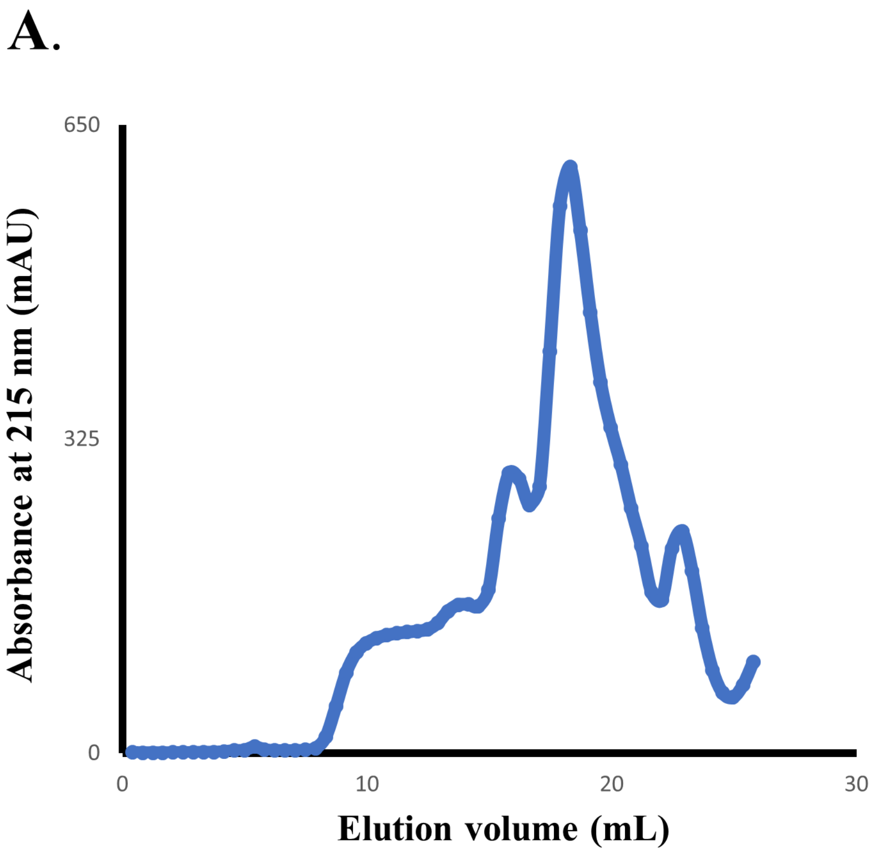

Fig. 2.3. Size Exclusion chromatography (SEC) elution profile of STIM2 15-66. SEC was performed using a Superdex 200 10/300 GL column (GE Healthcare, Inc.). **A.** Elution profile is based on absorbance at 215 nm (A_{215}) in arbitrary milli Absorbance Units (mAU) as a function of elution volume. **B.** Silver staining (Pierce) of STIM2 15-66 (~5.5 kDa) on a 15 % (w/v) SDS-PAGE gel of elution volumes 14-22 mL. Yellow box indicates fractions collected for analyses. *M* denotes Wide Range Protein Protein Molecular Weight Marker (BioBasic).

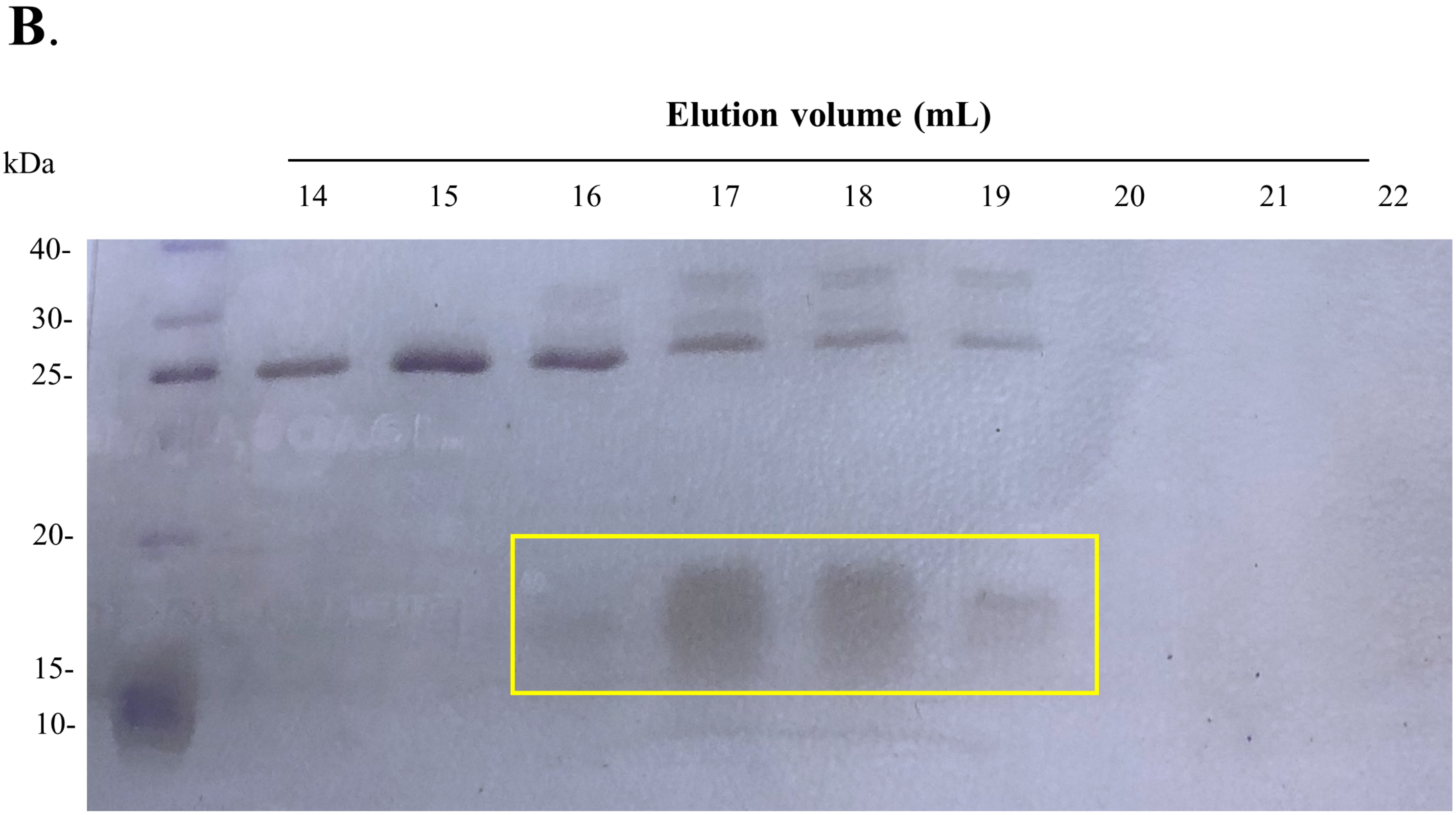

2.3 *S*-Nitrosylation of STIM2 recombinant proteins

All proteins of interest (*i.e.* wildtype STIM2 15-217, Cys15Ser, Cys53Ser, and Cys60Ser single mutants, Cys53Ser/Cys60Ser double mutant, and Cys15Ser/Cys53Ser/Cys60Ser triple mutant) were exchanged into the various buffers described in subsequent sections below, each containing 1 mM of the NO donor GSNO by ultrafiltration. Centrifugal concentrators with Amicon Ultra-15 10,000 Da (Millipore) or Vivaspin-20 3,000 Da (Sartorius) molecular weight cut-offs (for STIM2 15-217 and STIM2 15-66, respectively), at 2,500 ×g and 4 °C were used for the buffer exchange process. Specifically, a 20×20×20-fold or 20×20×20×20-fold buffer exchange was used for the Ca^{2+} loaded and depleted conditions, respectively.

The use of 1 mM GSNO was previously used effectively to donate NO and promote *S*-nitrosylation of proteins in solution under similar buffer conditions as I employed here (Zhu et al., 2018). A ~500 mM GSNO stock solution was synthesized by dissolving 1.54 g of reduced glutathione into 5.9 mL of 570 mM HCl. The glutathione solution was stirred gently in the dark while 1 mL of 5 M $NaNO_2$ was added to the mixture in a dropwise fashion. The mixture was stirred for an additional 5 minutes in the dark. After adjusting to pH 6 with 1 M NaOH, the solution was brought to a final volume of 10 mL using nano-filtered and deionized water (dH_2O). A spectrophotometer set to 335 nm and an extinction coefficient of 0.92 $mmol^{-1}$ cm^{-1} was used to determine the concentration of GSNO. GSNO serial dilutions of 500×, 750×, and 1000× were prepared to accurately assess the GSNO stock concentration. Approximately 1 mL aliquots of ~500 mM prepared GSNO were stored at -80 °C. These stocks were stored in single use aliquots.

2.4 Far-UV circular dichroism (CD) spectroscopy

In order to determine the effect *S*-nitrosylation on the secondary structure and thermal stability of the STIM2 full luminal domain (*i.e.* resides 15-217) and variable N-terminal region (*i.e.* residues 15-66), far-UV CD spectra were acquired using a Jasco J-815 CD spectrophotometer equipped with a Jasco PTC-423S temperature controller (Jasco Inc).

To prepare a far-UV CD sample in the Ca^{2+} loaded condition, protein solutions were exchanged into buffers at pH = 7.4 containing 10 mM TRIS-HCl, 5 mM $CaCl_2$ and either 1 mM DTT or 1 mM GSNO using a centrifugal concentrator (see section 2.3). To prepare samples in the Ca^{2+} depleted condition, protein solutions were incubated with 50 mM EDTA at 4 °C for ~18 hours the day prior and followed a similar buffer exchange approach as mentioned above, this time in the absence of 5 mM $CaCl_2$. CD spectra were acquired on 0.5 mg/mL protein samples in a 0.1 cm path length quartz cuvette.

Far-UV CD spectra were acquired at 20 °C with an average of 3 accumulations between 200 – 240 nm using 8 sec averaging time at each wavelength, 1 nm increments, and 1 nm bandwidth. Protein spectra were corrected for buffer contributions (10 mM TRIS-HCl ± 5 mM $CaCl_2$ at pH = 7.4).

To assess thermal stability, protein unfolding was monitored by measuring the changes in the 225 nm far-UV CD signal as a function of temperature using an 8 second averaging time, 1 nm bandwidth and a 1 °C/minute scan rate. The apparent midpoint of temperature denaturation (T_m) was used as a quantitative indicator of the thermal stability and was extracted by fitting a Boltzmann sigmoidal equation (see below) to thermal denaturation curves.

$$Y = \frac{Min + (Max - Min)}{1 + 10^{[(logT_m - X) \times slope]}}$$

where:

Y = change in CD signal,

Min = minimum CD signal (folded baseline),

Max = maximum CD signal (unfolded baseline),

T_m = temperature of denaturation,

X = temperature.

2.5 8-Anilinonaphthalene-1-sulfonic acid (ANS) binding assay

The relative levels of solvent-exposed hydrophobicity on the full luminal domain of STIM2 under reducing (control) and *S*-nitrosylating (experimental) conditions was assessed using ANS, a fluorescent probe which changes fluorescence intensity when bound to solvent-exposed hydrophobic protein regions. A Cary Eclipse spectrofluorimeter (Varian/Aligent Inc) was used to detect extrinsic ANS fluorescence intensity.

Wildtype STIM2 15-217 protein was exchanged into a buffer without Ca^{2+} the day following a 50 mM EDTA incubation as described in section 2.3, using a buffer at pH = 7.4 containing 20 mM TRIS, 150 mM NaCl, and either 1 mM DTT or 1 mM GSNO. 600 μL of 0.143 mg/mL protein solution was transferred to a quartz cuvette. The emission spectrum of the extrinsic ANS was acquired from 400 – 600 nm using an excitation wavelength of 372 at 37 °C. The photomultiplier tube (PMT) was set to 600 V while the excitation and emission slit widths were set to 10 and 20 nm, respectively. 5 mM $CaCl_2$ was titrated into the protein containing cuvette with a 15 minute incubation after each Ca^{2+} addition to allow for sufficient binding equilibration. Baseline extrinsic ANS readings were acquired in buffer only solutions using the identical spectrofluorimeter parameters and $CaCl_2$ titration regime.

2.6 Dynamic light scattering (DLS)

The contribution of deconvoluted particle size distributions to the light scattering intensity of Ca^{2+} depleted STIM2 15-217 were determined in a Micro Cuvette (JC501) using a DynaPro Nanostar dynamic light scattering detector equipped with a 658 nm laser (Wyatt Technology). Distributions of hydrodynamic radii size were extracted using the autocorrelation function, which correlates scattered light intensity fluctuations with respect to time (ns-μs) using the regularization algorithms for polydisperse solutions within the instrument software (Dynamics version 7; Wyatt Technology).

Wildtype STIM2 15-217 protein was exchanged into control and experimental buffers at pH = 7.4 containing 20 mM TRIS, 150 mM NaCl, and either 1 mM DTT or 1 mM GSNO. The respective buffer of the sample used for ultrafiltration was loaded into the quartz cuvette, equilibrated for 5 minutes, and then an initial light scattering reading was taken to ensure that the cuvette was dust free. Protein samples were assessed at final concentrations of 0.46 mg/mL. The protein samples were centrifuged at 12,000 ×g for 3 minutes and 5 μL aliquots per replicate were taken from the uppermost portion of the protein sample, thereby avoiding aggregated protein and dust, and loaded into the quartz cuvette. Following a 5 minute equilibration period, 10 consecutive acquisitions, each averaging 5 seconds, were recorded per sample at 37 °C. Low and high cut-offs of 1.5 nm and 150 nm, respectively, for the hydrodynamic radii size were used in the regularization deconvolutions for polydisperse solutions.

2.7 Equilibrium chemical denaturation curves

For the chemical denaturation of my proteins, urea was chosen as the chaotropic agent. Urea reduces the amount of order in the hydration shell around a protein, which leads to protein denaturation. A Cary Eclipse spectrofluorimeter (Varian/Aligent Inc) was used to detect intrinsic fluorescence intensity emitted from excited aromatic residues within my protein of interest as a function of urea concentration. Fluorescence of aromatic residues (*i.e.* five Trp residues within STIM2 15-217) is sensitive to the chemical environment, providing a direct readout of protein denaturation as the aromatic emerges from a buried non-polar environment in the folded state (*i.e.* high fluorescence) to an exposed polar environment in the unfolded state (*i.e.* low fluorescence).

Wildtype and mutant STIM2 15-217 protein samples were exchanged into a buffer with or without 5 mM $CaCl_2$ at pH = 7.4 containing 20 mM TRIS, 150 mM NaCl, and either 1 mM DTT or 1 mM GSNO by ultrafiltration as described in section 2.3. A series of protein samples were prepared in urea concentrations ranging from 0 to 6 M from a common stock of 7 M urea. Sample protein concentrations were kept constant at 5 μM in this series and incubated overnight for ~18-20 hours in a water bath at 25 °C. The following day, intrinsic fluorescent readings of aromatic residues Phe, Trp, and Tyr were recorded for each sample using an excitation wavelength of 280 nm and a slit width of 5 nm. Fluorescent emission spectra were acquired from 300-450 nm with an emission slit width of 10 nm and a scan rate of 600 nm/minute. Three scans per control (1 mM DTT) and seven scans per experimental (1 mM GSNO) samples at each urea concentration (0 to 6 M) were taken to ensure reproducible fluorescent readings within each sample. Equilibrium chemical denaturation curves were constructed from the change in fluorescence intensity of the last scan at 333 or 330 nm as a function of urea concentration in the Ca^{2+} loaded and Ca^{2+} depleted conditions, respectively. These wavelengths were chosen since they showed the maximal change in fluorescence intensity between the 0 M and 6 M samples under Ca^{2+} loaded and Ca^{2+} depleted conditions, respectively.

Wildtype and mutant STIM2 15-217 protein thermodynamic stability parameters including the change in Gibbs free energy of unfolding in water (ΔG_{H2O}), denaturant dependence of the unfolding transition (m-value) and midpoint of chemical-induced denaturation (C_{mid}) were assessed using equilibrium chemical denaturation curves and determined via the linear extrapolation method (Pace, 1986; Pace and Shaw, 2000). Chemical denaturation curves were fit to a two-state unfolding model through the following set of equations:

$$\Delta \mathrm{G} = -\mathrm{RT} \ln K = \Delta \mathrm{G}_{\mathrm{H2O}} - m \times (urea),$$

where R is the ideal gas constant, T is temperature in Kelvin, urea is the concentration in M, and K is the equilibrium constant of two state unfolding. K is related to the fraction of unfolded (F_U) protein as:

$$F_U = \frac{K}{1+K}$$

and thus, F_U can be solved from rearranging $\Delta \mathrm{G} = -\mathrm{RT} \ln K$ as

$$F_U = \frac{\exp^{(\frac{-\Delta \mathrm{G}}{RT})}}{1+\exp^{(\frac{-\Delta \mathrm{G}}{RT})}}$$

where $\Delta G = \Delta G_{H2O} - m \times (urea)$

The midpoint of chemical denaturation (*i.e.* C_{mid}) was calculated from

$$\frac{\Delta \mathrm{G}_{\mathrm{H2O}}}{m}$$

2.8 Solution nuclear magnetic resonance (NMR) spectroscopy

All NMR experiments were conducted using the Varian INOVA 600 MHz magnet equipped with a triple resonance HCN cryogenic probe house in the Biomolecular NMR facility at Western University (London, ON, CAN).

Solution NMR spectroscopy was utilized to determine structural changes associated with *S*-nitrosylation of the full luminal domain of STIM2. Approximately 250 μM of solubilized STIM2 15-217 protein was exchanged in a buffer containing 20 mM TRIS, 100 mM NaCl, 10 mM $CaCl_2$, and 1 mM GSNO at pH 7.4 as described in 2.3. The solubilized protein sample was supplemented with 60 μM 4,4-dimethyl-4-silapentane-1-sulfonic acid (DSS) and 10% (v/v) D_2O final concentrations, bringing the final sample volume to 660 μL. This sample was subsequently transferred into a Wilmad thin walled (0.38 nm), 5 mm NMR tube. A ^1H-^{15}N-heteronuclear single quantum coherence (HSQC) spectrum for *S*-nitrosylated STIM2 15-217 protein was obtained using 256 transients, which revealed strong peaks for ~200 amino acids. The *S*-nitrosylated spectra was then compared to the unmodified, reduced spectra by supplementing the sample with 1.5 mM DTT final concentration to fully remove the NO moiety via reduction before acquiring an HSQC spectra using the same parameters listed above.

Residue specific chemical shift perturbations (CSP) within the core EFSAM domain were determined from the *S*-nitrosylated and DTT-reduced ^1H-^{15}N HSQC spectra using previously assigned STIM2 EFSAM residue chemical shift information (*i.e.* residues 62-206) (Zheng et al., 2011a). The computer aided resonance assignment (CARA) software was used to transfer the assignments from EFSAM to the STIM2 15-217 spectra. Observed residue specific CSP between *S*-nitrosylated and control (*i.e.* DTT-reduced) spectra were calculated from the chemical shift differences observed in both ^1H and ^{15}N dimensions of each amide peak using the following equation:

$$Residue\ specific\ CSP\ =\ \sqrt{[\Delta H^2 + (0.14 \times \Delta N^2)]}$$

where:
ΔH^2 = parts per million (ppm) change in the proton dimension
ΔN^2 = ppm change in the nitrogen dimension

2.9 STIM2 Mobility Assay

To assess whether my *S*-nitrosylation protocol alters protein electrophoretic migration either directly or due to downstream post-translational modifications such as disulfide bond formation, I examined the mobility of wildtype STIM2 15-217 under reducing and non-reducing conditions by SDS-PAGE. Note that STIM2 15-217 intramolecular disulfide bond formation between any of Cys15, Cys53 or Cys60 would alter SDS-PAGE protein mobility due to protein de-linearization.

Wildtype and mutant STIM2 15-217 protein samples were exchanged at room temperature by ultrafiltration as described above into three buffers (pH = 8.0) containing 20 mM TRIS and 5 mM $CaCl_2$ for the oxidized condition, and supplemented with either 1 mM DTT or 1 mM GSNO for reduced and *S*-nitrosylated conditions, respectively. The final protein concentration used in this assay was 0.25 mg/mL for all conditions. Protein samples were separated on a 12.5% (w/v) SDS-PAGE gel at 120 V for 90 minutes and subsequently stained with Coomassie blue to visualize protein mobility.

2.10 Human embryonic kidney (HEK) 293T culture

2.10.1 HEK 293T culture and isolation

HEK 293T adherent cells were cultured in Dulbecco's modified eagle media (DMEM) supplemented with high glucose (Wisent), 10% (v/v) fetal bovine serum, 100 µg/mL penicillin (Wisent), and 100 units/mL streptomycin (Wisent). Cells were grown on 10 cm plates within a humidified incubator (Panasonic) at 37 °C and 5% (v/v) CO_2. When cells reached >70% confluency after an overnight incubation, the supplemented DMEM was aspirated in a laminar flow hood and immediately washed with 10 mL of 1× PBS. After swirling the wash buffer gently around the plate, the 1× PBS was removed and 1 mL of 0.25% trypsin (Thermo Scientific Fischer) supplemented with EDTA (Wisent) was added dropwise throughout the entire surface of the dish. The plates were manually rocked to ensure complete trypsin contact with all cells and subsequently placed into a humidified incubator at 37 °C and 5% (v/v) CO_2 for ~ 3 minutes. After the brief incubation, 9 mL of supplemented DMEM was added to the petri dish to attenuate trypsin activity. The cells were fully detached from the plate and the mixture homogenized by gentle mixing with a transfer pipette. A ~10% cell passage was used to propagate the cell line where 1 mL of the trypsinized cell mixture was aliquoted to a sterile petri dish containing 9 mL of fresh, supplemented DMEM. In order to carry out a ~20 % cell passage used for experimental purposes, 0.75 mL of the trypsinized cell mixture was aliquoted 6× into a 6-well (3.5 cm wells) plate each containing 2.25 mL of supplemented DMEM. Cells were maintained in a humidified incubator at 37 °C and 5% (v/v) CO_2 immediately after.

2.10.2 pCMV6-mCherry-STIM2 recombinant vector transfection

Upon reaching a confluency of ~70 – 80 %, HEK293T cells were transiently transfected with eGFP-Orai1 and either pCMV6-mCh, wildtype pCMV6-mCh-STIM2, pCMV6-mCh-STIM2 Cys15Ser single mutant, or pCMV6-mCh-STIM2 Cys15Ser/Cys53Ser/Cys60Ser triple mutant vectors using PolyJet™ transfection reagent (Froggabio) according to the manufacture's protocol. An empty pCMV6-mCh vector that only expressed monomeric cherry fluorescence protein in the absence of STIM2 was also used in some control experiments. In short, for each 3.5 cm well, the cell culture medium was replaced with 2 mL of supplemented DMEM ~30-60 minutes prior to transfection. Next, ~500 ng of each eGFP-Orai1 and one pCMV6-mCh-STIM2 vector were diluted into 50 μL DMEM containing only high glucose. Next, 3 μL of PolyJet™ reagent was diluted into the same volume mixture in a separate tube. The PolyJet™ mixture was immediately added to the 1 μg DNA mixture and mixed by gently vortexing. The PolyJet™/DNA mixture was subsequently incubated for ~15 minutes at room temperature. The 100 μL of transfection mixture was added dropwise to the cell culture dish (3.5 cm well) containing the adherent HEK293T cells in the culture medium containing supplemented DMEM. Finally, the cells were incubated at 37 °C and 5% (v/v) CO_2 for ~24 hours prior to experimentation.

For cells treated with GSNO, HEK293T cells were allowed to express the Orai and STIM2 proteins for ~6 hours prior to supplementation with 250 μM GSNO final concentration. These cells were then left overnight in the presence of GSNO to favour *S*-nitrosylating conditions.

2.10.3 Fura-2 ratiometric fluorescence spectroscopy of live cells

Approximately 24 hours post-transfection, 2 μM Fura-2 acetoxymethly ester (AM) was added to transfected HEK293T cells and mixed gently by swirling the mixture. The cells were incubated at 37 °C and 5% (v/v) CO_2 for ~40 minutes before aspirating the culture media. Two washes were performed with 0.5 mM $CaCl_2$ supplemented HEPES buffered saline solution (HBSS) comprised of 140 mM NaCl, 5 mM KCl, 10 mM D-glucose, 1 mM $MgCl_2$ and 10 mM HEPES at pH 7.4. For cells treated overnight with GSNO, 250 μM GSNO was included in the wash buffer to maintain the NO abundance. Washed HEK293T cells were mechanically lifted by pipette from the individual wells with 1.2 mL of 0.5 mM $CaCl_2$ supplemented HBSS with or without the GSNO, and transferred into a quartz cuvette. The 1.2 mL cell suspension was incubated at 22.5 °C for 10 minutes using a water bath attached to a Cary Eclipse spectrofluorimeter (Varian/Agilent, Inc.)

In order to assess the relative transfection efficiency, eGFP and mCh fluorescence of the cell suspension were acquired using excitation wavelengths of 470 and 565 nm, respectively. eGFP fluorescence emission was recorded between 475 to 575 nm while mCh fluorescence emission was recorded between 580 to 680 nm. Excitation and emission slit widths were set to 10 and 20 nm, respectively, while the PMT was set to 650 V.

Fura-2 ratiometric fluorescence measurements of cell suspensions were acquired to determine basal Ca^{2+} levels and SOCE. Alternating excitation wavelengths of 340 and 380 nm and an emission wavelength of 510 nm were used to measure Fura-2 fluorescence at 22.5 °C, using a PMT of 650 V and an excitation and emission slit widths of 10 and 20 nm, respectively. Fluorescence intensity at the two excitation wavelengths were acquired for a total 900 s in 1 s increments. After 100 s of baseline recordings, 1 mM $CaCl_2$ was added to the cell suspension bathed in 0.5 mM Ca^{2+}. After an additional 100 s, 2 mM EGTA was added to chelate all free Ca^{2+} in the extracellular solution. At 300 s, 1 μM thapsigargin (TG) was added to passively deplete ER Ca^{2+} stores by blocking ER membrane bound SERCA pumps. Finally, at 600 s, 2.5 mM $CaCl_2$ was added to the suspended cells. All concentrations listed are final concentrations calculated based on the total cell suspension volume at the time of addition. Data was analyzed by plotting the fluorescence intensity ratio at 340/380 nm versus time.

Basal Ca^{2+} levels were measured by averaging raw Fura-2 fluorescence ratios calibrated to Ca^{2+} concentrations over 50 s in 0.5 mM Ca^{2+}. The TG-induced ER Ca^{2+} release was measured by averaging normalized Fura-2 fluorescence ratios (*i.e.* F/F_0) over 300 s after TG addition, while SOCE was measured by averaging normalized Fura-2 fluorescence ratios after 2 mM Ca^{2+} addback over 100 s once the response stabilized. F/F_0 was used to determine the fractional increase in cytosolic Ca^{2+} over baseline, where F and F_0 are the Fura-2 fluorescence ratios after and before (*i.e.* baseline) the addition of TG, respectively.

Ratiometric fluorescence spectroscopy measurements for basal Ca^{2+} levels were calibrated to the corresponding Ca^{2+} concentration (nM) using the following equation (Garcia-Sainz et al., 2010; Grynkiewicz et al., 1985):

$$Ca^{2+} = K_d \times \frac{R - R_{min}}{R_{max} - R} \times \frac{F380_{min}}{F380_{max}}$$

where,

K_d (equilibrium dissociation constant of Ca^{2+} from Fura-2) was set to 225 nM (Garcia-Sainz et al., 2010; Grynkiewicz et al., 1985),

R = F340/F380 ratio at any time during experimentation,

R_{min} = F340/F380 ratio in the Ca^{2+} depleted condition,

R_{max} = F340/F380 ratio in the Ca^{2+} saturated condition,

$F380_{min}$ = absolute fluorescence at 380nm in the Ca^{2+} depleted condition,

$F380_{max}$ = absolute fluorescence at 380nm in the Ca^{2+} saturated condition.

The Ca^{2+} saturated condition was attained by adding 0.2% (v/v) Triton X-100 to cell suspensions post-experimentation, while subsequent addition of 10 mM EGTA (pH = 8) attained the Ca^{2+} depleted condition. The same R_{max}, R_{min}, $F380_{max}$, and $F380_{min}$ values were applied to all experiments and were determined $n = 5$ from representative cell suspensions.

2.11 Statistical Analysis

Statistical Analyses involved using an unpaired t-test when comparing between two independent groups, or a One-way ANOVA followed by Tukey's post-hoc test when comparing between three or more independent groups. Tukey's multiple comparison analysis was used in this study as opposed to other post-hoc tests because of its conservative estimate of the α-value, which decreases the probability of obtaining a false positive significance. Because the effect of *S*-nitrosylation on STIM2 function in mammalian cells is fairly unknown, a Tukey's post-hoc test was used for a more stringent statistical analysis.

Chapter 3: Results

3.1 The isolated human STIM2 variable N-terminal region is unstructured

The unbinding of Ca^{2+} from the EF-hand concomitant with EFSAM structural destabilization are hallmarks of STIM mediated SOCE initiation (Stathopulos et al., 2006; Zheng et al., 2011a). As a result, I investigated the effect of Ca^{2+} on the secondary structure of the full luminal domain of STIM2 using far-UV CD spectroscopy, normalizing the signal on a per residue basis (*i.e.* mean residue ellipticity). Typical of Ca^{2+}-bound EF-hand containing proteins (Ikura, 1996), wildtype STIM2 15-217 samples loaded with Ca^{2+} displayed a characteristic α-helical spectrum with two strong negative ellipticity minima at 208 and ~225 nm. Furthermore, a marked loss in negative ellipticity at both minima of wildtype STIM2 15-217 protein was observed in samples free of Ca^{2+}, indicating an attenuated α-helicity (Fig. 3.1A).

The short N-terminal regions of STIM1 and STIM2, upstream of the core EFSAM domains can profoundly affect Orai1 channel activation kinetics (Zhou et al., 2009). Therefore, I investigated the secondary structure of the variable STIM2 N-terminal region (*i.e.* residues 15-66) using far-UV CD spectroscopy to probe for potential structural elements. In this assessment, I used the STIM2 N-terminal region in isolation. Consistent with an online PSIPRED prediction tool (McGuffin et al., 2000) which showed a very low propensity for regular secondary structure in this region, Ca^{2+} loaded wildtype STIM2 15-66 protein displays a characteristic random coil far-UV CD spectrum indicated by minimal signal between ~240 – 210 nm and abruptly negative ellipticity at ~200 nm (Fig. 3.1B).

Recent evidence suggests that *S*-nitrosylation of the variable N-terminal region of STIM1 reduces SOCE activity (Gui et al., 2018; Zhu et al., 2018). Consequentially, I sought to elucidate whether *S*-nitrosylation could affect the α-helicity of the STIM2 full luminal domain and/or promote alternate secondary structural elements in the STIM2 variable N-terminal region, as both changes could affect STIM2 mediated SOCE. To promote *S*-nitrosylation, I exchanged the reduced protein by ultrafiltration into a buffer containing 1 mM GSNO and no reducing agent. This approach of high excess NO donor compared to protein concentration is necessary due to the fast reversibility of *S*-nitrosylation in the absence of NO and has been successfully applied previously *in vitro* with

STIM1 and several other proteins (Bocedi et al., 2004; Feng et al., 2011; Gui et al., 2018; Hao et al., 2004; Liu et al., 2002; Zhu et al., 2018). Unfortunately, supplementing the protein buffer with 1 mM GSNO caused a high level of absorbance and high tensions exceeding 800 V below 215 nm, thus producing distorted far-UV CD spectra.

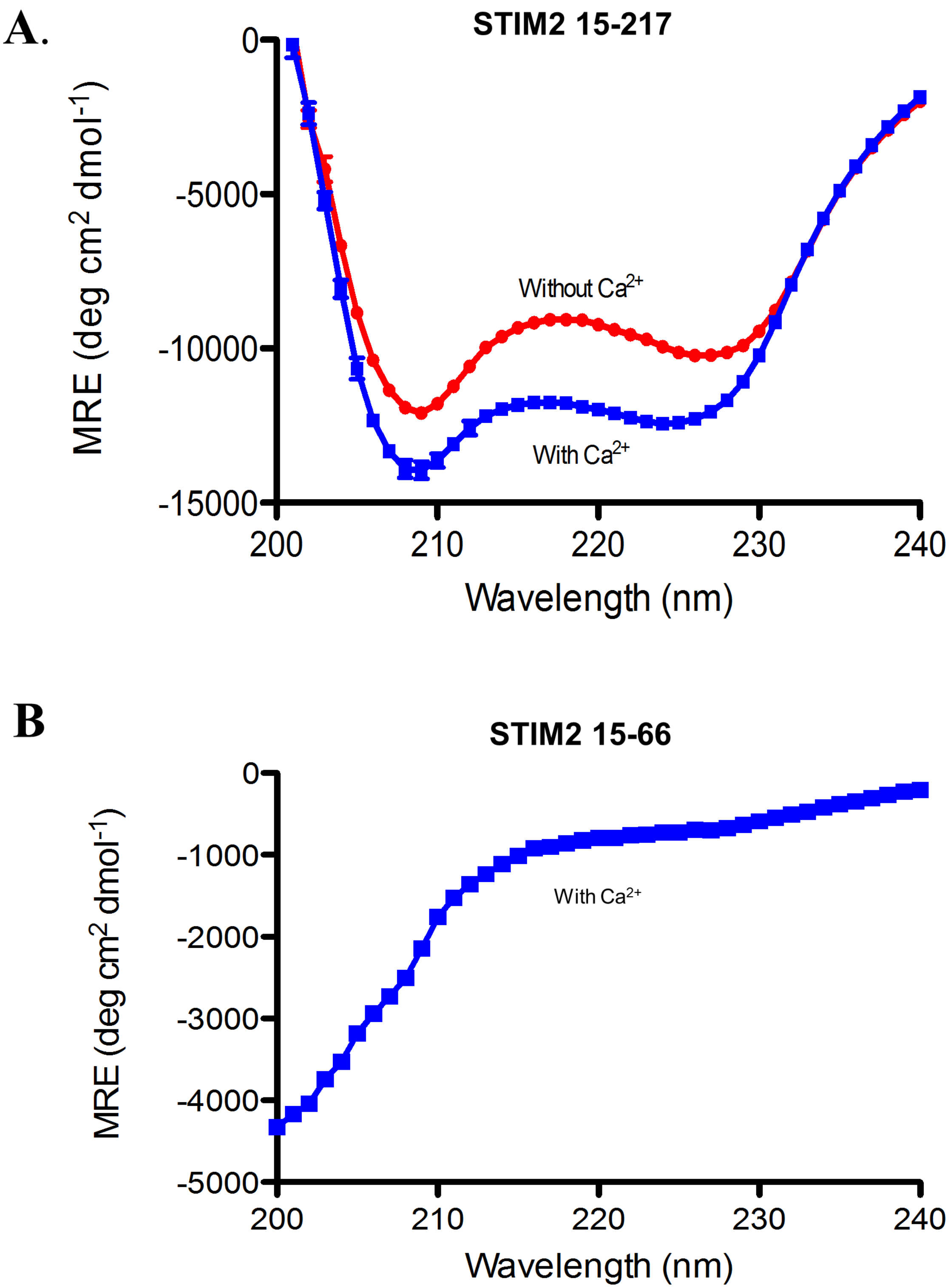

Figure 3.1. Far-UV CD spectra of wildtype STIM2 proteins. Spectra were acquired at 20 °C from 200-240 nm in 0.1 cm pathlength cuvettes using 0.5 mg mL^{-1} protein. **(A)** Mean Residue Ellipticity (MRE) of STIM2 15-217 under the Ca^{2+} depleted (red) or Ca^{2+} loaded (blue) conditions. Spectra were corrected for buffer contributions of 10 mM TRIS HCl, 1 mM DTT ± 5 mM $CaCl_2$ at pH = 7.4. **(B)** MRE of STIM2 15-66 under the Ca^{2+} loaded (blue) condition. Spectra were corrected for buffer contributions of 50 mM Na_2HPO_4 and 1 mM DTT at pH = 7.4. Analysis revealed that Ca^{2+}-depleted STIM2 15-217 has less α-helical structure compared to the Ca^{2+}-loaded state. Moreover, wildtype STIM2 15-66 displays a characteristic random coil spectrum indicated by a strong negative ellipticity at 200 nm in the presence of Ca^{2+}. Data are reported as mean ± SEM; n=3.

3.2 Excess NO donor enhances the thermal and thermodynamic stability of wildtype STIM2 15-217 under Ca^{2+} deplete and replete conditions

Normally, the majority of STIM proteins remain in a quiescent, inactivated state under replete ER Ca^{2+} conditions, with the exception of a subset of STIM2. Upon ER luminal Ca^{2+} depletion, STIM proteins destabilize to become activated and redistribute in close apposition to the PM (Brandman et al., 2007; Liou et al., 2007; Stathopulos et al., 2006; Zhang et al., 2005a). Although determining changes in secondary structure induced by *S*-nitrosylation via far-UV CD spectroscopy was not feasible, I instead examined changes in thermal stability due to excess NO donor in both Ca^{2+} loaded and depleted conditions at the CD spectroscopy minimum of 225 nm as a function of temperature, where the high tension was well below 800 V in the presence of 1 mM GSNO. The apparent midpoint of temperature denaturation (T_m) was used as an indicator of thermal stability by fitting a Boltzmann Sigmoidal equation to thermal denaturation curves, where a higher T_m is indicative of a more stable protein. The apparent T_m of Ca^{2+} loaded wildtype STIM2 15-217 was significantly increased by ~+4 °C under *S*-nitrosylating conditions when compared to the control, unmodified condition (** $p < 0.01$), suggesting a pronounced stabilization when the majority of STIM2 is in a quiescent state (Fig 3.2.1A and 3.2.1B). A similar, yet modest increase of ~+2 °C in apparent T_m of Ca^{2+} depleted wildtype STIM2 15-217 under *S*-nitrosylating conditions was detected (* $p < 0.05$), indicating a thermal stabilization when the majority of STIM2 is in the active state (Fig 3.2.1C and 3.2.1D).

To complement and further support my thermal stability data, I conducted equilibrium chemical denaturation experiments to thermodynamically quantify *S*-nitrosylation induced stability changes of wildtype STIM2 15-217 in both the Ca^{2+} loaded and depleted states. Unlike thermal denaturation which is irreversible, chemical denaturation of the STIM2 luminal domain is completely reversible and thus pliable to equilibrium analyses. Consequentially, the change in Gibbs free energy of unfolding in water (ΔG_{H2O}) and cooperativity of unfolding (*m*-value) were quantified via the linear extrapolation method (Pace and Shaw, 2000) using a two state, folded to unfolded model, where an increase in ΔG_{H2O} is indicative of increased protein thermodynamic stability. The urea concentration where the fraction of unfolded molecules was 50% (*i.e.* C_{mid}) was calculated by dividing ΔG_{H2O} by m and used as another indicator of relative stability. Expectedly, in the presence of Ca^{2+} and excess GSNO, wildtype STIM2 15-217 exhibited an increase in protein stability reflected by increased ΔG_{H2O} (+0.63 kcal/mol; ***$p < 0.001$) and C_{mid} (+0.24 M; *$p < 0.05$) values when compared to the control, unmodified condition (Fig. 3.3A-C). *S*-Nitrosylating conditions induced a similar effect in the absence of Ca^{2+}; however, this effect was more pronounced (ΔG_{H2O} +1.16 kcal/mol; ***$p < 0.001$ and C_{mid} +0.27 M; *$p < 0.05$) (Fig. 3.3D-F), suggesting a greater thermodynamic stability enhancement from *S*-nitrosylation under activating conditions (*i.e.* Ca^{2+} depleted) compared to deactivating conditions (*i.e.* Ca^{2+} loaded).

Collectively, these data show that the STIM2 luminal domain thermal and thermodynamic stabilities are enhanced in the presence of excess NO. Interestingly, excess NO enhances the thermal stability of STIM2 15-217 in the Ca^{2+} loaded condition to a larger extent than the Ca^{2+} depleted condition, whereas the opposite trend is observed in thermodynamic stability assessments.

WT STIM2 15-217, Ca^{2+} Loaded

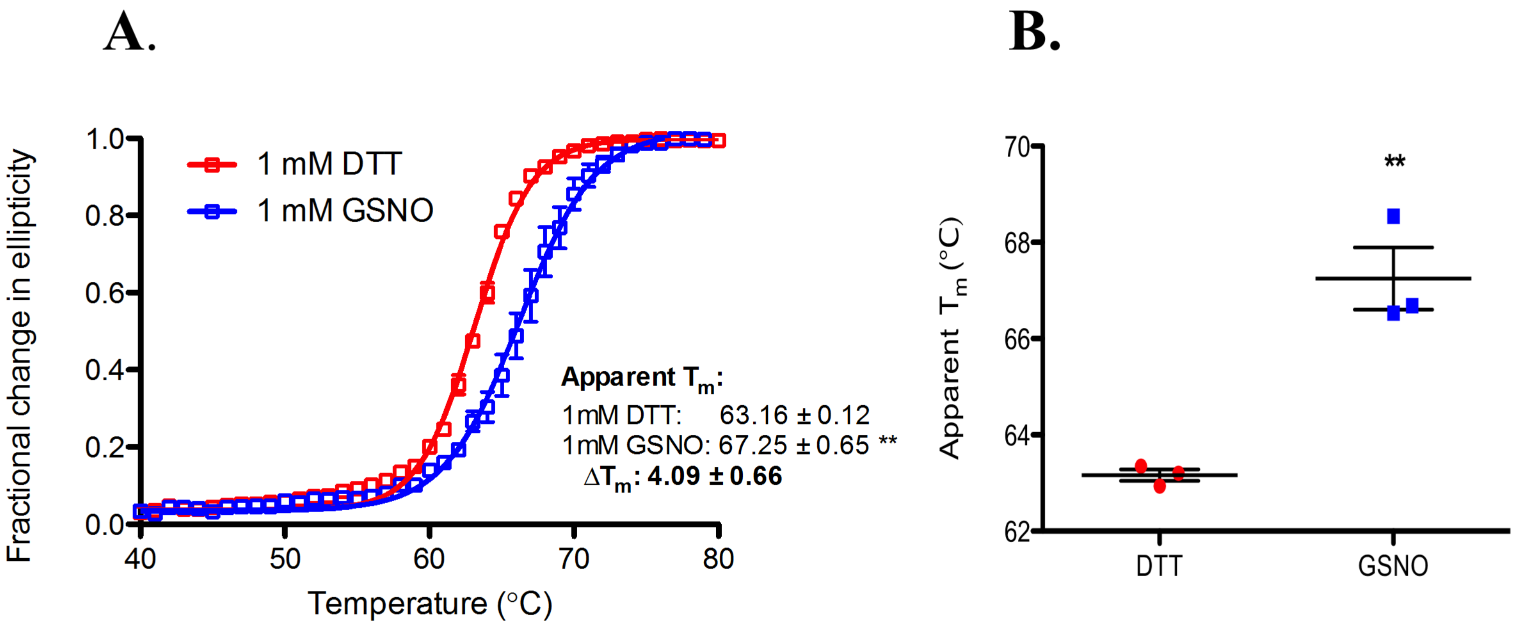

WT STIM2 15-217, Ca^{2+} Depleted

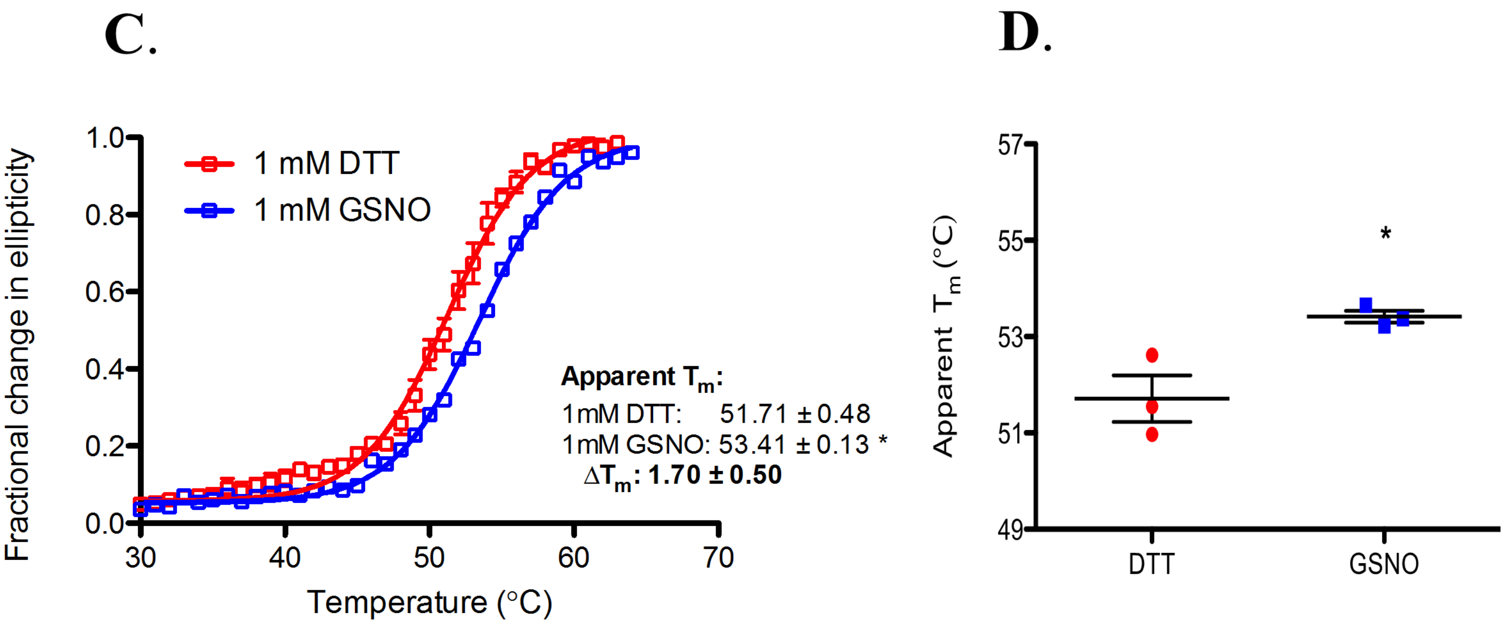

Figure 3.2.1 Excess NO enhances the thermal stability of wildtype STIM2 15-217 under Ca^{2+} depleted and loaded conditions. Thermal melts were acquired at 225 nm from 20 to 80 °C in a 0.1 cm pathlength cuvette using 0.5 mg mL^{-1} protein. **(A, C)** Fractional change in CD ellipticity and **(B, D)** Apparent Melting Temperature (T_m) analysis for reduced (1 mM DTT) and *S*-nitrosylated (1 mM GSNO) wildtype STIM2 15-217 under Ca^{2+} depleted and Ca^{2+} loaded (5 mM $CaCl_2$) conditions. T_m was calculated by fitting a Boltzmann Sigmoidal equation to thermal denaturation curves. Statistical analysis was performed using an unpaired Students *t*-test ($*p < 0.05$, $**p < 0.01$ against DTT control). Excess NO significantly enhances the T_m of wildtype STIM2 15-217 compared to control treatment in Ca^{2+} depleted and loaded conditions.

WT STIM2 15-217, Ca^{2+} Loaded

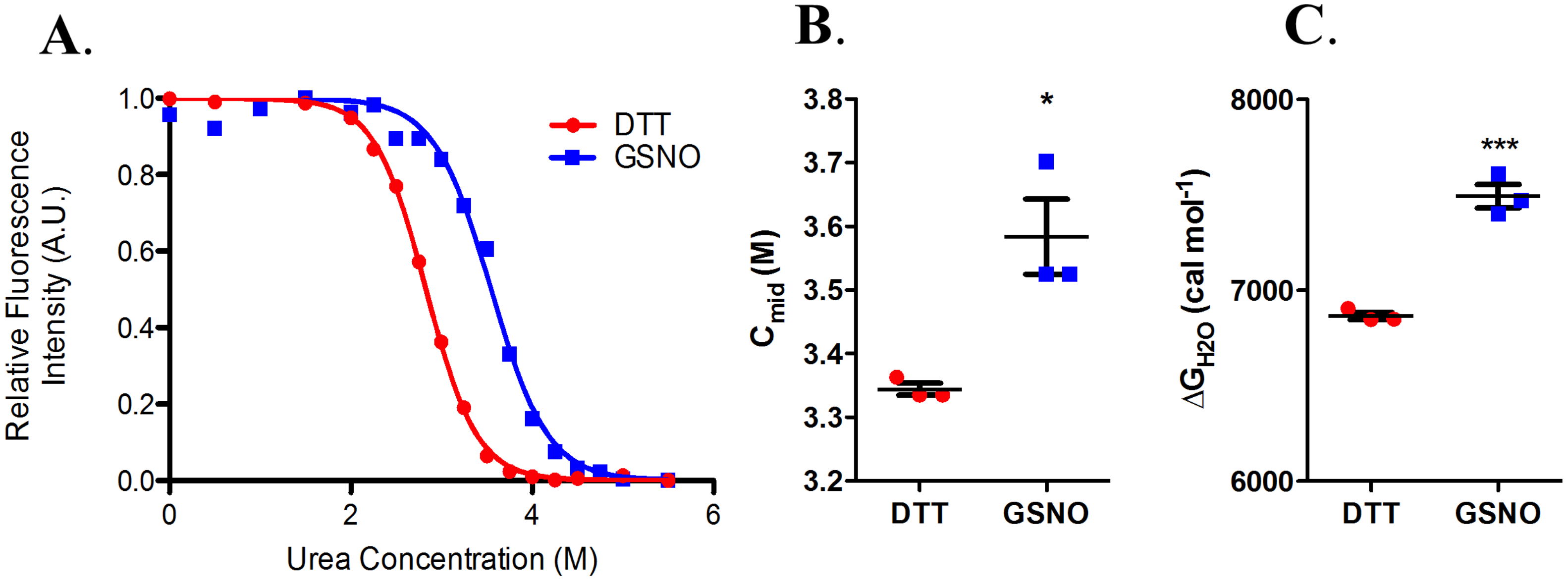

WT STIM2 15-217, Ca^{2+} Depleted

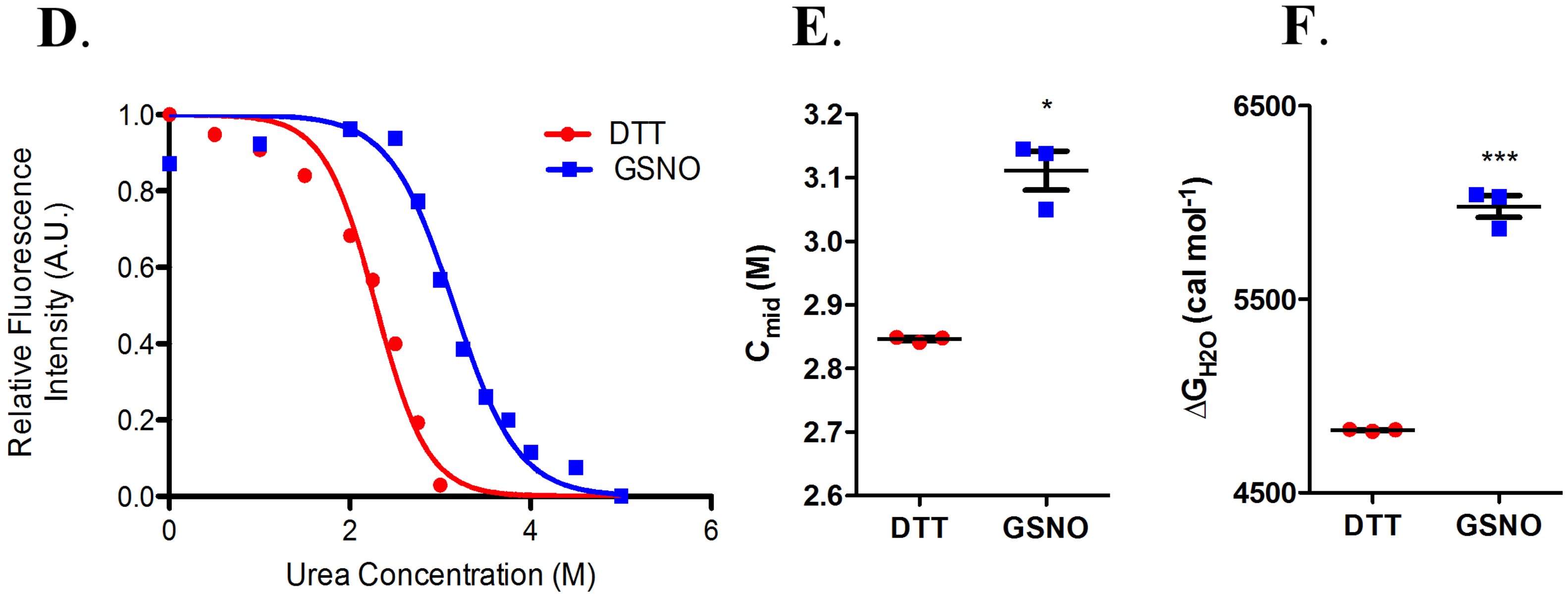

Figure 3.2.2 Excess NO enhances the thermodynamic stability of wildtype STIM2 15-217 under Ca^{2+} depleted and loaded conditions. **(A, D)** Representative equilibrium denaturation curves. **(B, E)** Midpoint of chemical denaturation (C_{mid}) and **(C, F)** change in Gibbs Free Energy of unfolding in water (ΔG_{H2O} [cal mol^{-1}]) for reduced (1 mM DTT) and *S*-nitrosylated wildtype STIM2 15-217 (5 μM) under Ca^{2+} depleted and Ca^{2+} loaded (5 mM $CaCl_2$) conditions. The ΔG_{H2O} was calculated using a two-state unfolding equilibrium model while the C_{mid} was calculated by dividing ΔG_{H2O} by a globally fitted *m*-value. Statistical analysis was performed using an unpaired *t*-test ($*p < 0.05$, $***p < 0.001$ against DTT control). Excess NO enhances the thermodynamic stability of wildtype STIM2 15-217 in both Ca^{2+} depleted and loaded conditions. Data are reported as mean ± SEM; n = 3 for all groups.

3.3 Ca^{2+} depleted wildtype STIM2 15-217 is resistant to higher order oligomerization

Ca^{2+} depletion induced dimerization and/or oligomerization is a key induction step prior to the formation of puncta at ER/PM junctions, where STIMs couple to Orai1 and mediate SOCE (Liou et al., 2007; Liou et al., 2005). Furthermore, molecular and structural differences of both the EFSAM and variable N-terminal region between STIMs contribute to their distinct oligomerization propensities, where STIM1 reaches a steady oligomeric state ~70× faster than STIM2 (Stathopulos et al., 2009). As a result, I examined whether *S*-nitrosylation could affect the oligomerization propensity of the full luminal domain of STIM2, which contains both the variable N-terminal region and EFSAM domain, through dynamic light scattering (DLS) experiments. The DLS autocorrelation functions were fit to the regularization algorithm to deconvolute the polydisperse distribution of hydrodynamic radii sizes in solution. Because light scattering intensity is proportional to the radius of particle size to the power of 6, the majority (*i.e.* > 95% by mass) of solubilized protein is represented by the first peak of distribution sizes. No shift in hydrodynamic radii size distribution is observed in the presence of excess NO donor for Ca^{2+} depleted wildtype STIM2 15-217 protein compared to control, unmodified protein (Fig. 3.3). Assuming globularity, the theoretical hydrodynamic radius for the ~24.0 kDa STIM2 15-217 monomer is ~2.4 nm. In the absence of Ca^{2+}, DLS revealed a distribution of sizes centered at ~5 nm, which could represent a mixture of monomers, dimers and higher order oligomers. This distribution of sizes was largely unaffected by the presence of 1 mM GSNO, in contrast to previous studies using the luminal domain of STIM1 (*i.e.* residues 23-213) that showed a shift to smaller hydrodynamic sizes in the presence of GSNO (Zhu et al., 2018). It should be noted that the Ca^{2+} depleted luminal domain of STIM1 exhibits a main distribution of hydrodynamic radii centered at ~10 nm under similar experimental conditions (Zhu et al., 2018), making the GSNO-dependent shifts to monomeric radii easily detectable using the identical experimental parameters.

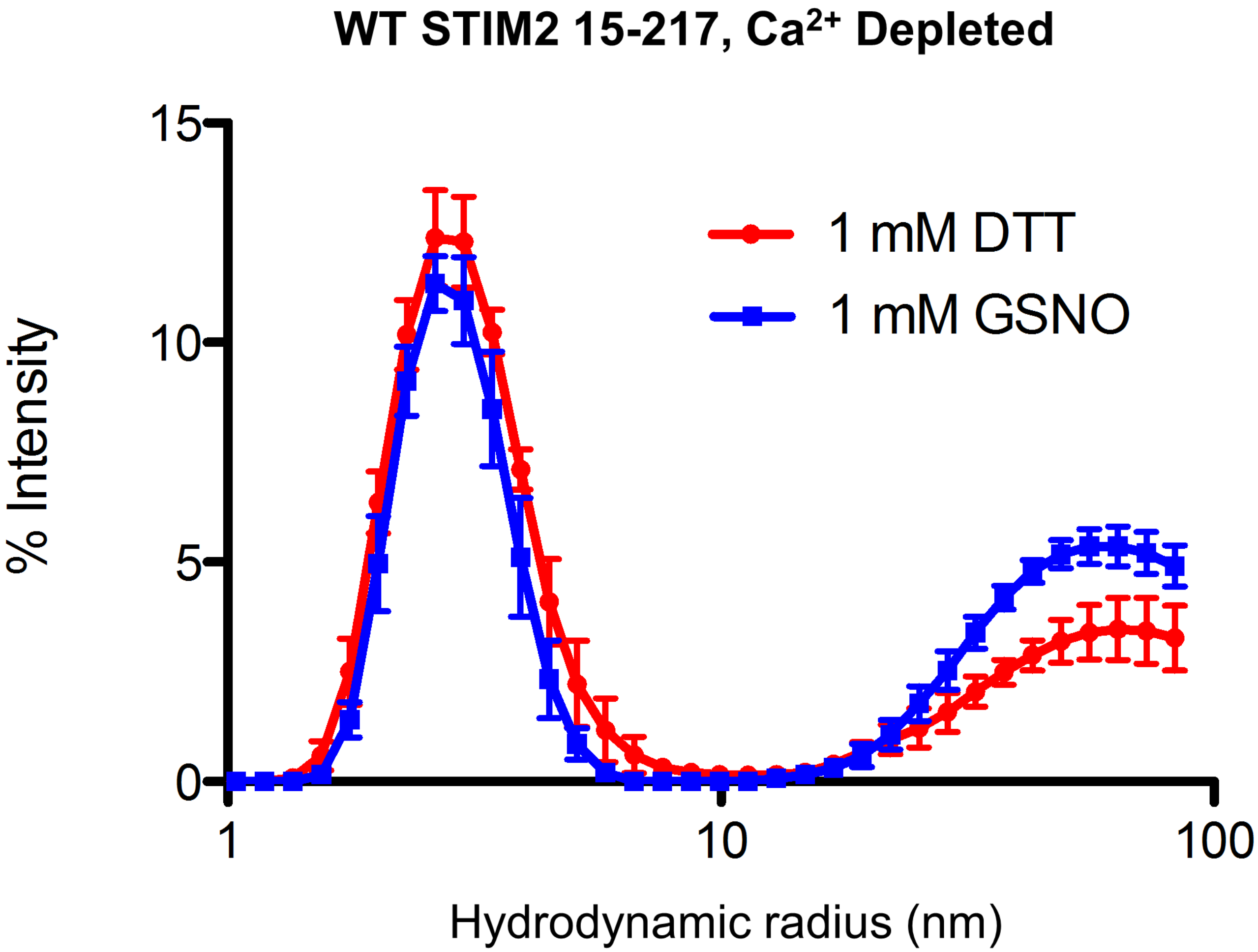

Figure 3.3. Dynamic Light Scattering (DLS) analysis of Ca^{2+} depleted STIM2 15-217. The contribution of the particle size distributions to the light scattering intensity of Ca^{2+} depleted STIM2 15-217 (0.5 mg/mL) in either reducing (1 mM DTT) or *S*-nitrosylating (1 mM GSNO) conditions. Since light scattering intensity is proportional to radius of the particle size to the power of 6, the majority (i.e. > 95 % by mass) of solubilized protein is represented by the first peak of distribution sizes. No difference in the distribution of hydrodynamic radii of STIM2 15-217 was apparent for samples exchanged into GSNO-containing compared to DTT-containing buffer. Excess NO does not alter the main distribution of hydrodynamic sizes of wildtype STIM2 15-217 in the Ca^{2+} depleted state under the experimental conditions tested. Data are reported as mean ± SEM; n = 3 for both groups.

3.4 Excess NO donor minimally affects the level of solvent-exposed hydrophobicity of wildtype STIM2 15-217

Oligomerization induced by Ca^{2+} depletion is driven by an increase in exposed hydrophobic regions of STIM EFSAM domains (Stathopulos et al., 2006). Therefore, I sought to determine the level of solvent exposed hydrophobicity of Ca^{2+} loaded and depleted STIM2 15-217 in the presence and absence of excess NO donor using the extrinsic fluorescent probe ANS. When ANS binds to solvent-exposed hydrophobic protein regions, the extrinsic fluorescence emission spectrum of ANS exhibits higher fluorescence and a blue-shifted peak maximum. Thus, a lower fluorescence intensity and a peak maximum at higher wavelengths is indicative of a protein conformation with less exposed hydrophobic residues. Here, incubating ANS in the presence of wild-type STIM2 15-217 under reducing conditions (*i.e.* 1 mM DTT) and in the absence of Ca^{2+} resulted in higher ANS fluorescence intensity and concomitant shift of the peak maximum to lower wavelength. The addition of 5 mM $CaCl_2$ decreased the fluorescence intensity and shifted the peak maximum to a higher wavelength, indicative of a conformational change that decreased the solvent-exposed hydrophobicity (Fig. 3.4A). Similar ANS experiments performed in the presence of 1 mM GSNO instead of 1 mM DTT showed analogous fluorescence intensities and locations of the peak maxima (Fig. 3.4B). The ANS fluorescence properties in the presence of 1 mM GSNO- or DTT-containing buffer was insensitive to 5 mM $CaCl_2$.

Collectively, my ANS experiments suggest that excess NO minimally affects the level of solvent-exposed hydrophobicity of Ca^{2+} depleted wildtype STIM2 15-217 and that the addition of 5 mM $CaCl_2$ to these samples induces a conformational change with less solvent-exposed hydrophobicity, both in the presence and absence of excess GSNO.

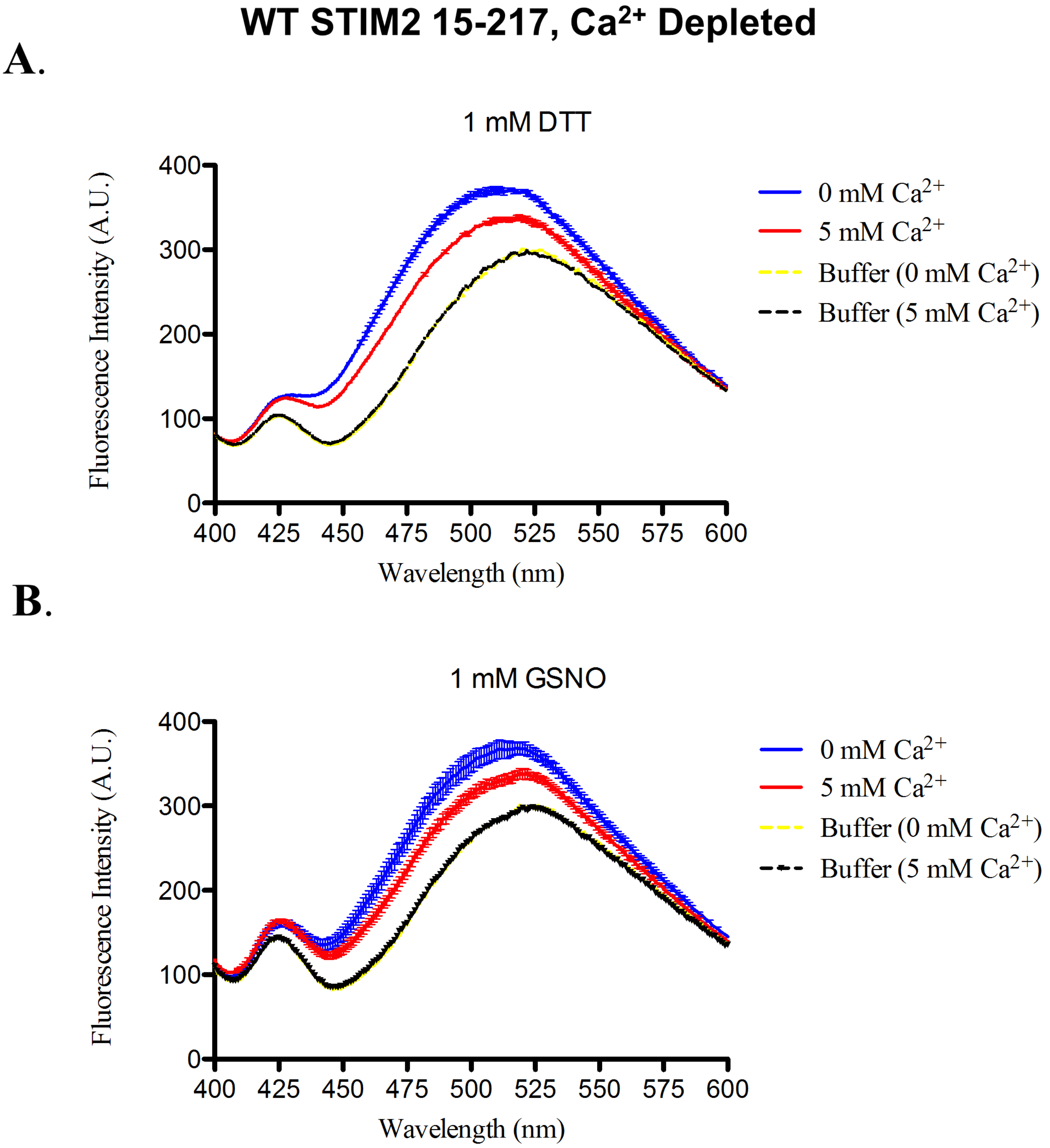

Figure 3.4. Extrinsic ANS-induced fluorescence ($\lambda_{excitation}$ = 372 nm) of wildtype STIM2 15-217 under reducing or *S*-nitrosylating conditions in the presence or absence of Ca^{2+}. Each sample contained 0.15 mg mL^{-1} protein, 0.05 mM ANS, and 0.5 mM EDTA. Fluorescence intensity was measured at 37 °C between 400-600 nm emission wavelengths in a buffer containing (**A**) 1 mM DTT or (**B**) 1 mM GSNO, 20 mM TRIS HCl, and 150 mM NaCl at pH = 7.4. No differences in ANS fluorescence intensity was observed between 1 mM GSNO versus 1 mM DTT treatments, suggesting that GSNO minimally affects the solvent exposed hydrophobicity of the luminal domain of STIM2 under the experimental conditions tested. Data are reported as mean ± SEM; n = 3 for all groups.

3.5 Excess NO induces chemical shift perturbations on the STIM2 EFSAM core, far from the N-terminal Cys residues

Having discovered that excess NO donor enhances the stability of the luminal STIM2 domain, but does not affect the exposed surface hydrophobicity and oligomerization, I next used solution nuclear magnetic resonance (NMR) spectroscopy to confirm that protein structural changes underlie the observed stabilization. In the presence of Ca^{2+} and under reducing conditions, the wildtype STIM2 15-217 ^{1}H-^{15}N-HSQC spectrum exhibited highly dispersed amide $^{1}H(^{15}N)$ crosspeaks ranging from ~11.0 to 6.5 ppm in the ^{1}H dimension, indicative of a well-folded conformation (Fig. 3.5A). After exchange of the protein into a 1 mM GSNO containing buffer, the spectrum showed numerous $^{1}H(^{15}N)$ chemical shift perturbations (CSP)s, indicative of structural changes. To determine whether the structural changes were localized on the variable N-terminal region or on the EFSAM core domain, I compared the ^{1}H-^{15}N-HSQC spectrum in the presence of 1 mM DTT to the previously assigned spectrum of Ca^{2+}-loaded STIM2 EFSAM (*i.e.* residues 62-206) (Zheng et al., 2011a) [Biological Magnetic Resonance Bank (BMRB) accession number 17289]. Most $^{1}H(^{15}N)$ resonance signals of the full STIM2 15-217 luminal domain were the same as those observed for the EFSAM in isolation (*i.e.* residues 62-206), suggesting this core sensing domain adopts a similar conformation in the presence of the variable N-terminal and C-terminal extensions.

Given these spectral similarities, I determined the total CSP for each EFSAM $^{1}H(^{15}N)$ resonance within the full STIM2 15-217 luminal domain caused by the excess GSNO (Fig. 3.5B). Mapping the CSPs relative to the EFSAM amino acid sequence revealed two major clusters of residue-specific perturbations: one on the entering helix of the canonical EF-hand and a second on the exiting helix of the non-canonical EF-hand and the adjacent SAM linking helix. Mapping the CSPs on the three-dimensional (3D) backbone ribbon and surface structures of STIM2 EFSAM [Protein Data Bank (PDB) accession identification 2L5Y] revealed that the majority changes were localized to one face of the domain (Fig. 3.5C and 3.5D). The three Cys residues that can undergo *S*-nitrosylation (*i.e.* Cys15, Cys53 and Cys60) are located in the variable N-terminal region of the luminal domain, outside the EFSAM core. Thus, the data suggest that excess GSNO causes global structural changes within the luminal domain, likely due to an interaction between the modified variable region containing three Cys residues and one side of the EFSAM core.

A.

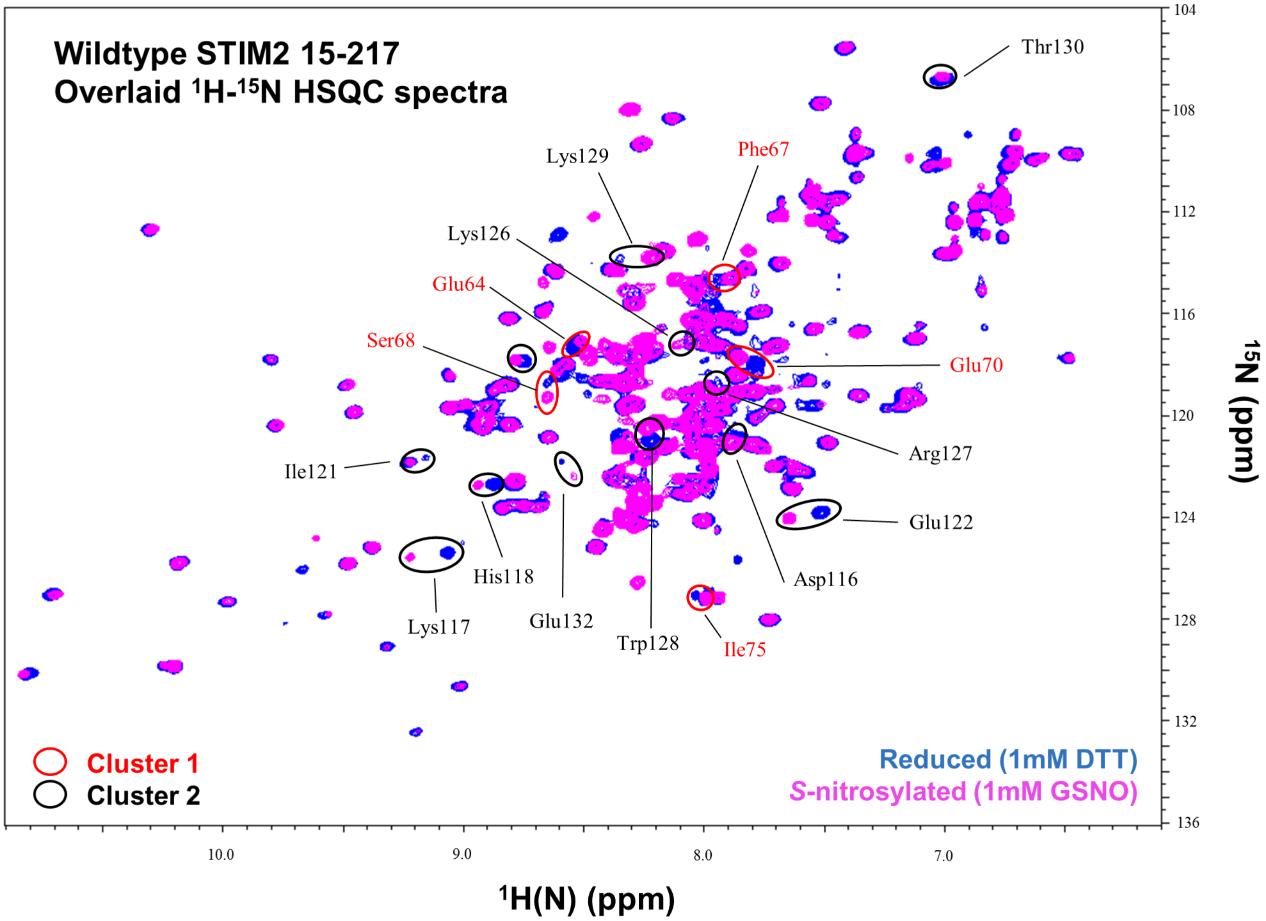
Wildtype STIM2 15-217
Overlaid ¹H-¹⁵N HSQC spectra
Thr130
Lys129
Phe67
Lys126
Glu64
Ser68
Glu70
Arg127
Ile121
Glu122
His118
Asp116
Lys117
Glu132
Trp128
Ile75
Cluster 1
Cluster 2
Reduced (1mM DTT)
S-nitrosylated (1mM GSNO)
104
108
112
116
120
124
128
132
136
¹⁵N (ppm)
10.0
9.0
8.0
7.0
¹H(N) (ppm)

B.

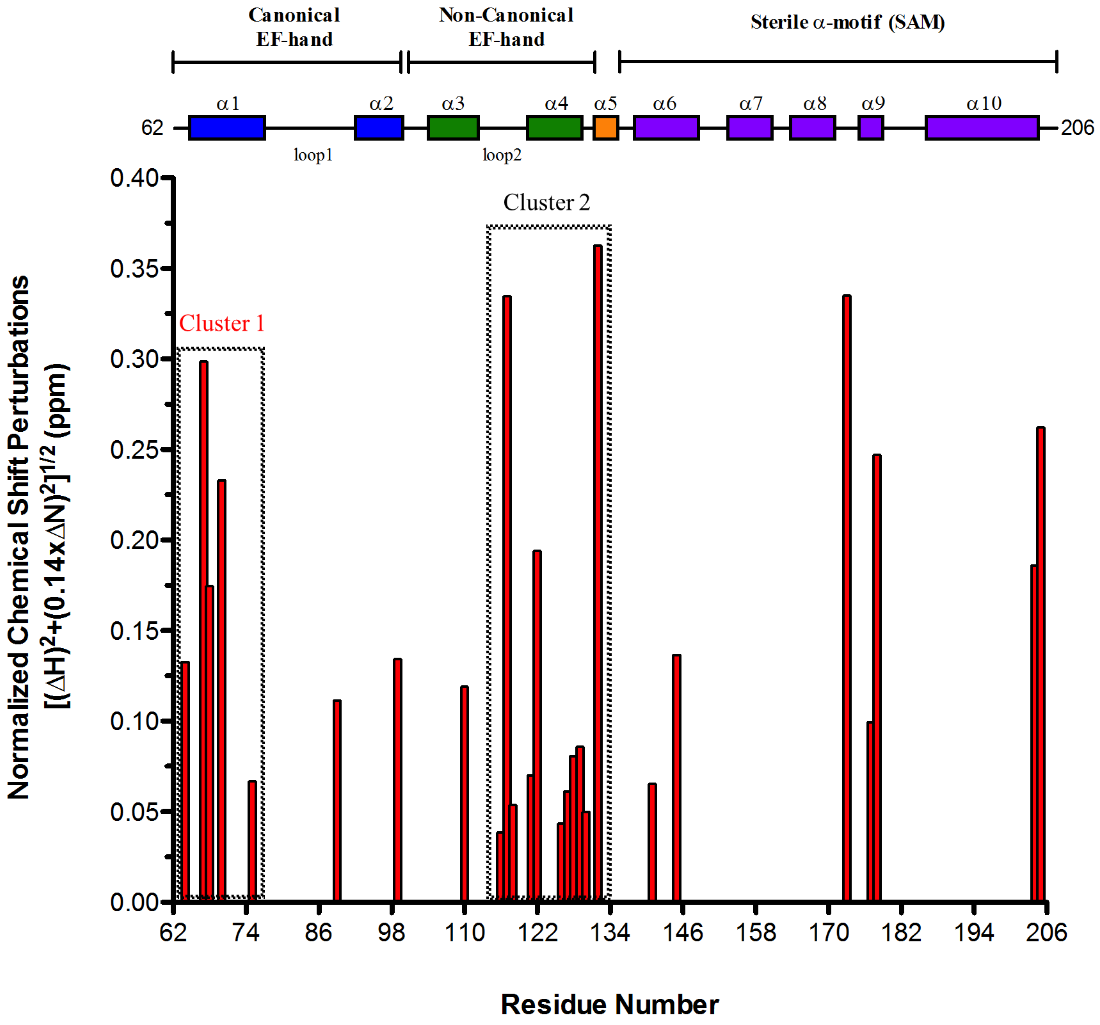
Canonical EF-hand
Non-Canonical EF-hand
Sterile α-motif (SAM)
α1
α2
α3
α4
α5
α6
α7
α8
α9
α10
62
206
loop1
loop2
Cluster 1
Cluster 2
Normalized Chemical Shift Perturbations
[(ΔH)²+(0.14xΔN)²]^1/2 (ppm)
0.40
0.35
0.30
0.25
0.20
0.15
0.10
0.05
0.00
62
74
86
98
110
122
134
146
158
170
182
194
206
Residue Number

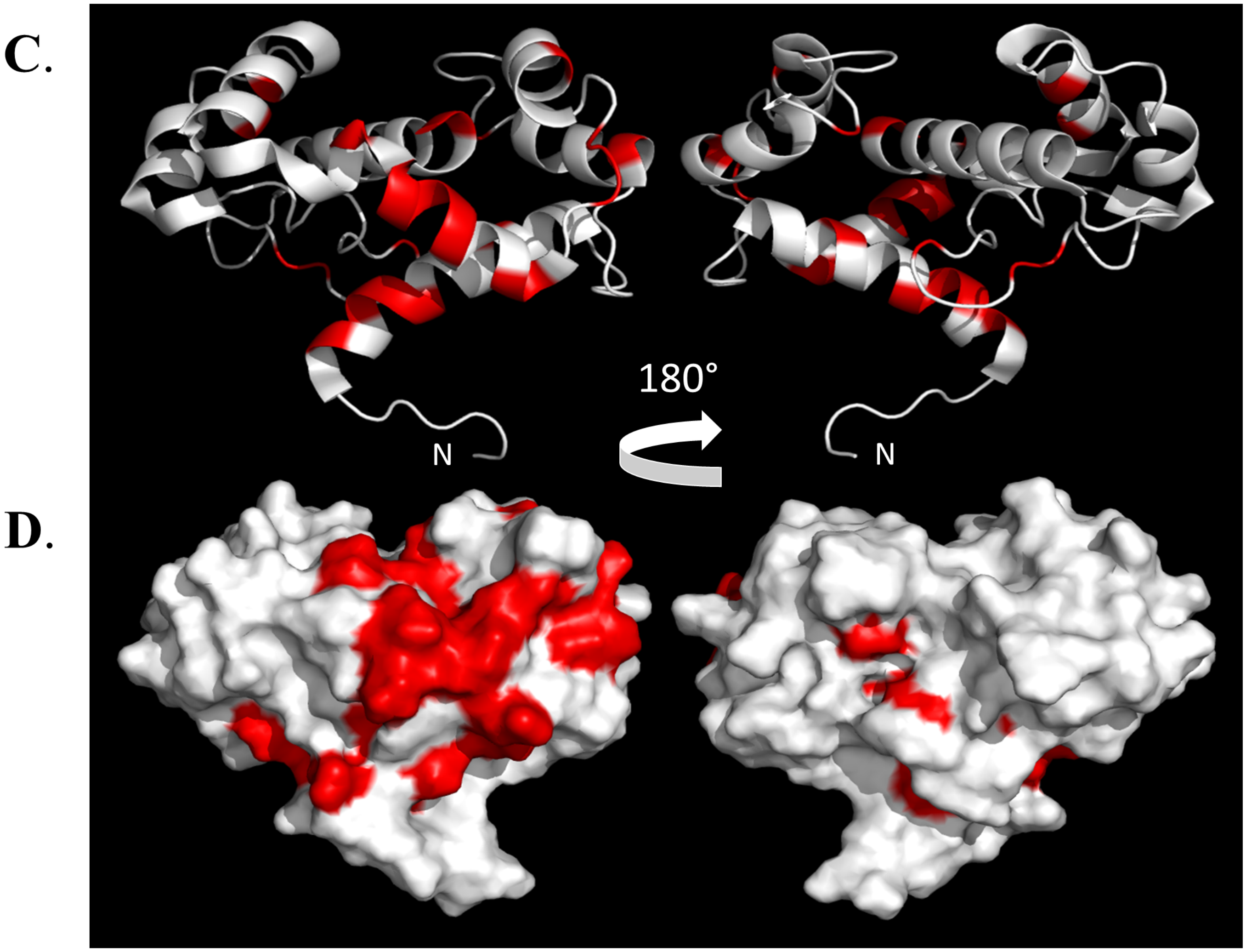

Figure. 3.5. Solution nuclear magnetic resonance spectroscopy assessment of wildtype STIM2 15-217 structural perturbations induced under *S*-nitrosylating conditions. (A) Overlaid representative ^{1}H-^{15}N Heteronuclear Single Quantum Coherence (HSQC) spectra of STIM2 15-217 (~3.0 mg/mL) protein under reducing and *S*-nitrosylating conditions. Spectra were acquired at 600MHz (Varian Inova) and 20 ºC in buffers (pH=7.4) containing 100 mM NaCl, 10 mM $CaCl_2$, 20 mM TRIS and either 1 mM DTT (blue) or 1 mM GSNO (magenta). Assignable residue specific chemical shift perturbations (CSPs) are highlighted by red and black circles. **(B)** Normalized CSPs due to GSNO treatment. Differences in CSP were calculated from spectra under reducing compared to the *S*-nitrosylating conditions. CSPs are shown relative to the STIM2 EFSAM core residue number. The relative location of STIM2 EFSAM secondary structural elements are shown at the top of the panel where rectangles represent helices. Dashed boxes indicate the location of two clusters of residues that were perturbed. **(C)** Cartoon representation of the protein backbone trace and **(D)** surface structure of the STIM2 EFSAM domain (*i.e.* residues 62-206) mapped with chemical shift perturbations (red) derived from *A* and *B* caused by GSNO treatment. Most chemical shift perturbations were observed in two clusters which correspond to the entering helix of the canonical EF-hand and the exiting helix of the non-canonical EF-hand and the adjacent SAM linking helix. Mapping the CSPs on the three-dimensional surface structure reveals that perturbations are localized to one side of STIM2 EFSAM. Assigned chemical shift and protein atom coordinate data of STIM2 EFSAM are from BMRB and PDB accession number 17289 and 2L5Y.pdb, respectively.

3.6 Excess NO donor enhances the thermal and thermodynamic stability of STIM2 15-217 in a Cys-specific manner

Having found that excess GSNO causes structural perturbation far from the variable N-terminal region of STIM2 that contains the Cys residues, I next assessed whether the stabilization observed was Cys specific. *S*-nitrosylation of specific Cys residues is known to affect stability, structure, localization and function of the protein modified (Gould et al., 2013). *S*-Nitrosylation of Cys49 and Cys56 in STIM1 was found to suppresses Ca^{2+} sensitivity and inhibit SOCE (Zhu et al., 2018). STIM2 not only contains Cys residues at similar positions in the variable N-terminal region (*i.e.* Cys53 and Cys60), but also has an additional Cys residue at the N-terminus (*i.e.* Cys15), which I posit is also susceptible to *S*-nitrosylation. Accordingly, *S*-nitrosylation of this unique Cys residue may underlie distinct structural and functional differences between STIM homologs. To test whether the stabilization observed for STIM2 in the presence of excess NO occurs in a Cys-specific manner, I created a series of Cys to Ser mutant STIM2 15-217 proteins. In total, I expressed and purified five different mutant proteins: Cys15Ser, Cys53Ser, Cys60Ser (single mutants), Cys53Ser/Cys60Ser (double mutant) and Cys15Ser/Cys53Ser/Cys60Ser (triple mutant). For all variants, protein expression levels and purities were similar to wild-type.

First, I assessed the thermal stability of each of the Ca^{2+}-loaded proteins in the presence and absence of excess GSNO. The Cys15Ser and Cys53Ser single mutants minimally affected the thermal stability of STIM2 15-217, with the proteins showing only marginally higher T_m values of ~+0.2 and +0.4 °C, respectively, compared to wild-type (Fig. 3.6.1). The Cys60Ser, Cys53Ser/Cys60Ser and Cys15Ser/Cys53Ser/Cys60Ser mutations affected stability to a larger extent, with T_m values indicating destabilization of ~-1.2, -3.2 and -2.4 °C, respectively, compared to wild-type (Fig. 3.6.1).

Next, I assessed the thermal stability of these proteins in the presence of 1 mM GSNO. The difference in T_m between *S*-nitrosylation promoting and reducing conditions (*i.e.* ΔT_m) for each protein variant was calculated as a measure of the effect of *S*-nitrosylation on protein stability. Recall that excess GSNO induced a thermal stabilization of Ca^{2+} loaded wildtype STIM2 15-217 of ~+4.1 °C (Fig. 3.2.1A and 3.2.1B). The same data is reproduced here as a readily accessible reference to the mutant T_m data (Fig. 3.6.2A and 3.6.2B). Remarkably, excess GSNO induced a smaller increase in T_m of only ~+2.2 °C for the Cys15Ser mutant protein compared to wild-type, indicating that the unique Cys15 of STIM2 15-217 plays a role in the GSNO-mediated stabilization (Fig. 3.6.2C and 3.6.2D). In contrast, the Cys53Ser and Cys60Ser single mutant proteins showed no apparent enhancement in stability with T_m values significantly decreasing by ~-1.0 °C (Fig. 3.6.2E-H). Both the Cys53Ser/Cys60Ser double mutant and Cys15Ser/Cys53Ser/Cys60Ser thermal stabilities appeared largely insensitive to excess GSNO with T_m values marginally increasing by ~+0.1 and +0.4 °C, respectively (Fig. 3.6.2I-L).

Collectively, these data show that mutation of Cys53 or Cys60, which are conserved with Cys residues at analogous positions in STIM1, abrogates the GSNO-mediated thermal stabilization. However, the Cys15, which is unique to STIM2, also contributes to GSNO-mediated stabilization when the Cys53 and/or Cys60 sulfhydryls remain modifiable. Importantly, Ca^{2+} loaded Cys15Ser/Cys53Ser/Cys60Ser STIM2 15-217 does not undergo a significant change in thermal stability, indicating a Cys-specific response to the NO donor.

The thermal stability assessments were performed in the presence of Ca^{2+} where GSNO caused a larger apparent stabilization compared to the absence of Ca^{2+} for the wild-type protein. Next, I performed equilibrium chemical denaturation experiments using the Cys variants to quantify the stability changes in the absence of Ca^{2+} where GSNO caused a larger thermodynamic stabilization for the wild-type protein. Here, I used the difference in the ΔG_{H2O} and C_{mid} (*i.e.* $\Delta\Delta G_{H2O}$ and ΔC_{mid}) between *S*-nitrosylation promoting and reducing conditions as indicators of the stability changes. Excess GSNO induced an increase ΔG_{H2O} for Ca^{2+} depleted wildtype STIM2 15-217 of ~+1.2 kcal mol^{-1}, which corresponded to an increase in C_{mid} of ~+0.3 M urea (Fig. 3.2.2D-F). The same data are reproduced here as a readily accessible reference to the mutant data (Fig. 3.6.3A-C). The Cys15Ser protein showed less pronounced stabilization compared to wild type, reflected by a ΔC_{mid} of only ~+0.2 M and $\Delta\Delta G_{H2O}$ of ~+0.5 kcal mol^{-1} (Fig. 3.6.3D-F). As observed with the Ca^{2+}-loaded thermal stability assessments, the Ca^{2+}-depleted Cys49Ser/Cys60Ser double mutation largely abrogated any Cys15-mediated stabilization in the presence of excess GSNO (Fig. 3.6.2G-I), showing a $\Delta\Delta G_{H2O}$ of ~+0.1 kcal mol^{-1}. Interestingly, ΔC_{mid} for this double mutant was slightly increased (+0.1 M; $p < 0.05$) due to lower cooperativity of unfolding (*m*-value). The Ca^{2+} depleted

Cys15Ser/Cys53Ser/Cys60Ser triple mutant did not exhibit any GSNO-mediated differences in ΔG_{H2O} or C_{mid} (Fig. 3.6.3J-L).

Collectively, these data demonstrate that the stability of Ca^{2+}-depleted STIM2 15-217 is enhanced in the presence of excess NO, and the greatest stabilization occurs when all native Cys are available for modification. Moreover, this enhanced stability is a Cys-specific response, and the unique Cys15 residue contributes to stabilization only when the conserved Cys53 and Cys60 residues are available for *S*-nitrosylation. These trends are similar to those observed using the Ca^{2+} loaded proteins and assessed by temperature denaturation.

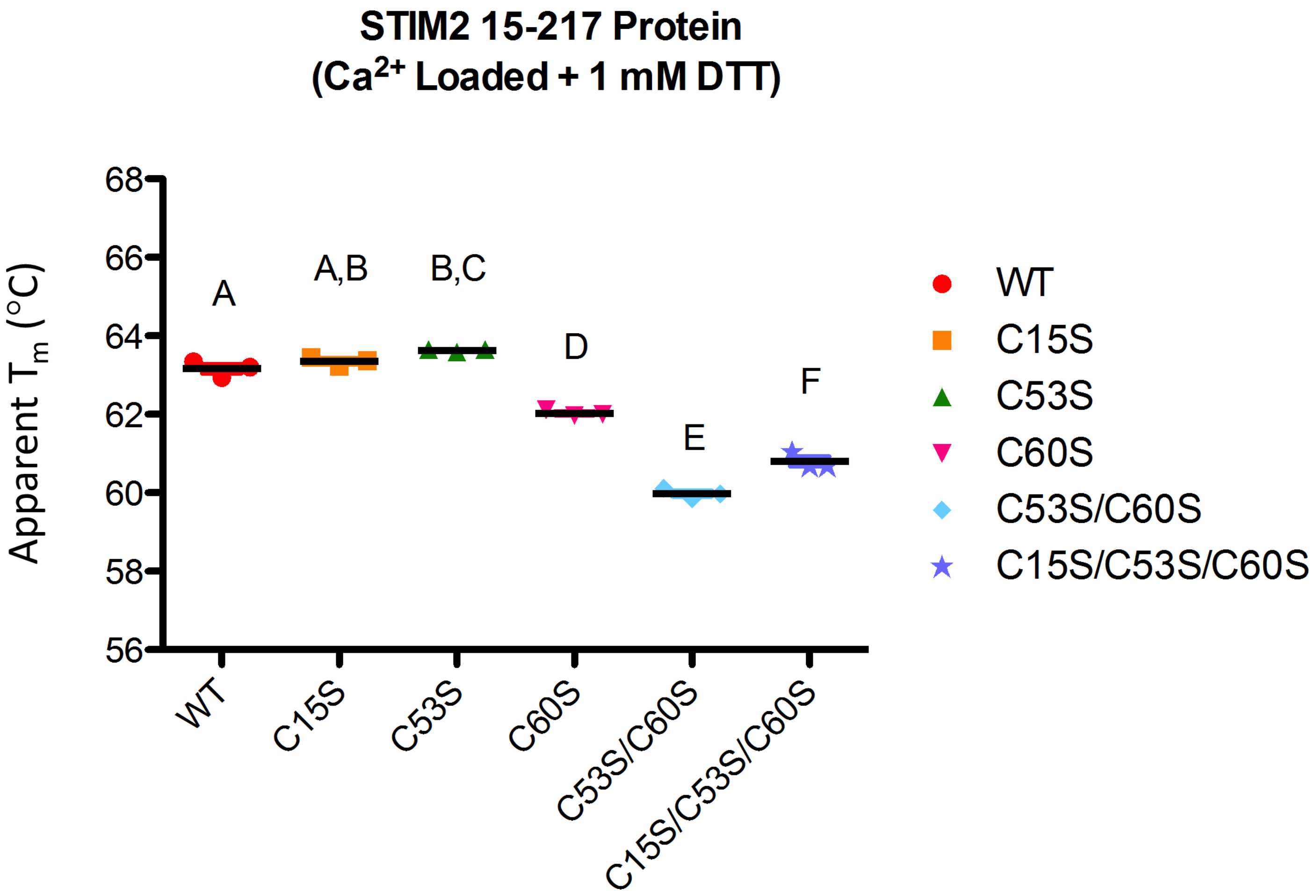

Figure. 3.6.1. Thermal stability comparison for Ca^{2+} loaded wildtype and Cys to Ser mutant STIM2 15-217 proteins under reducing conditions. Thermal melts were acquired at 225 nm from 20 to 80 °C in a 0.1 cm pathlength cuvette using 0.5 mg mL^{-1} protein in a buffer at pH = 7.4 containing 5 mM $CaCl_2$, 10 mM TRIS-HCl and 1 mM DTT. Apparent Melting Temperature (T_m) analysis for Ca^{2+} loaded wildtype, C15S, C53S, C60S single-mutant, C53S/C60S double-mutant, and C15S/C53S/C60S triple-mutant STIM2 15-217 protein under reducing conditions. Data are represented as mean ± SEM; $n = 3$ for each group. Statistical analysis was performed using a one-way ANOVA followed by a Tukey's post-hoc test. $P < 0.05$ was considered statistically significant. Groups with the same letter are not significantly different from one another. C53S/C60S double mutant protein had the lowest intrinsic thermal stability reflected by the lowest apparent T_m.

A.

WT STIM2 15-217

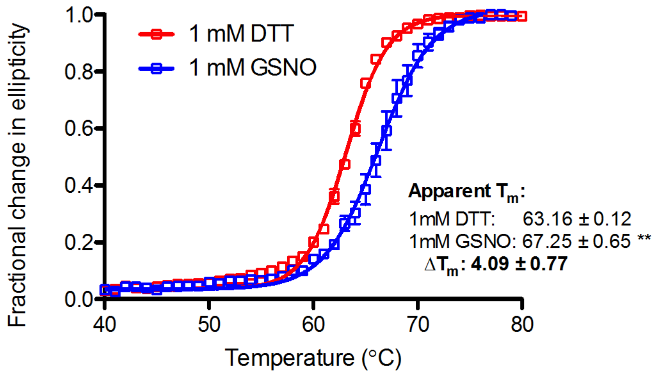

B.

WT STIM2 15-217

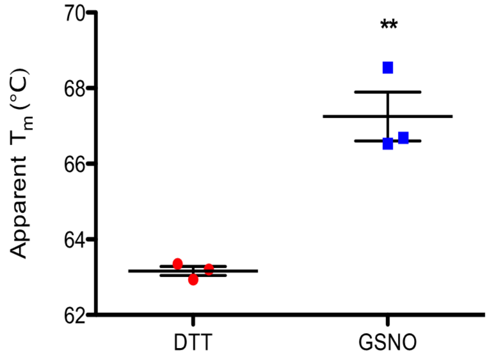

C.

C15S STIM2 15-217

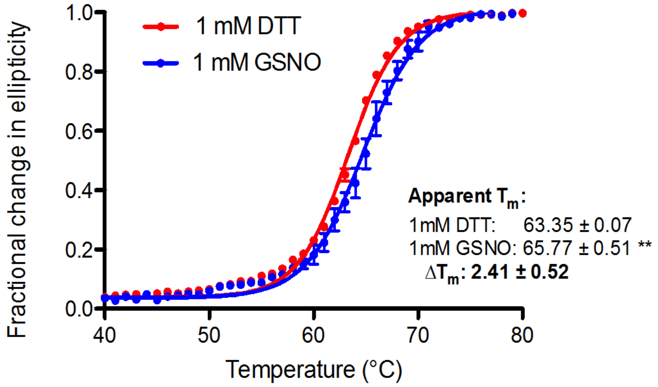

D.

C15S STIM2 15-217

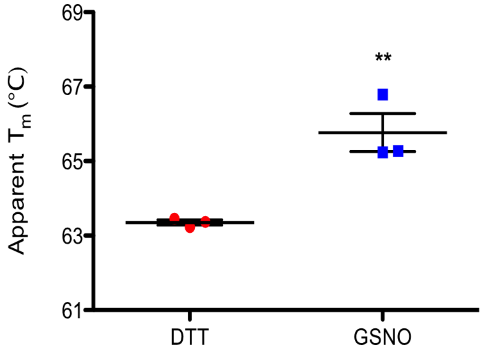

E.

C53S STIM2 15-217

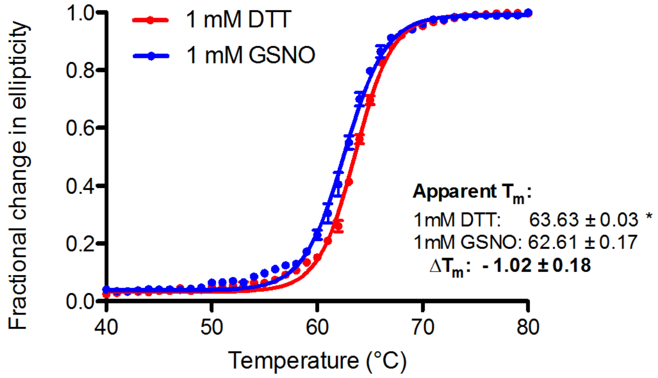

F.

C53S STIM2 15-217

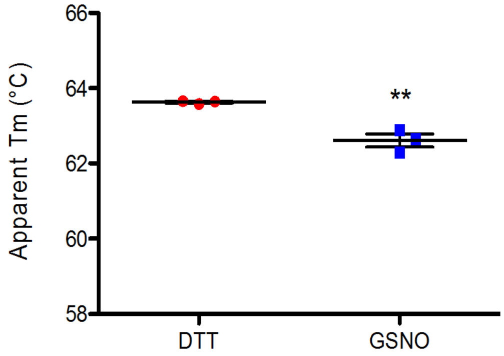

G.

C60S STIM2 15-217

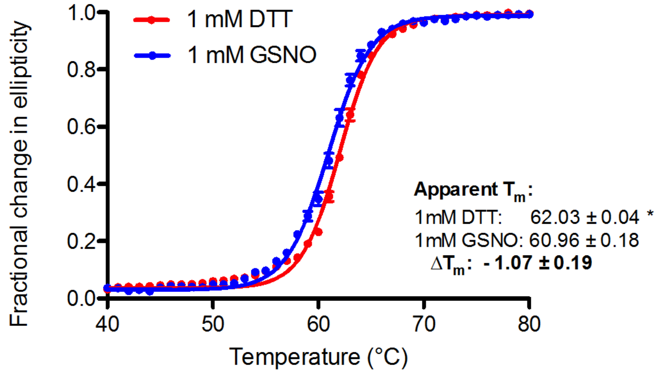

H.

C60S STIM2 15-217

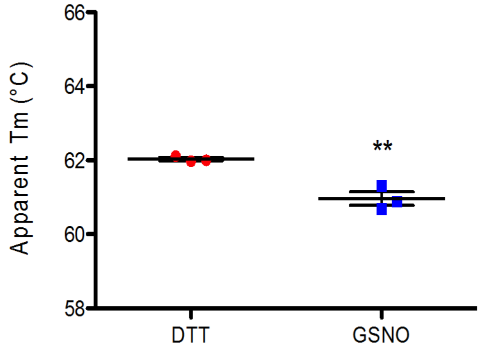

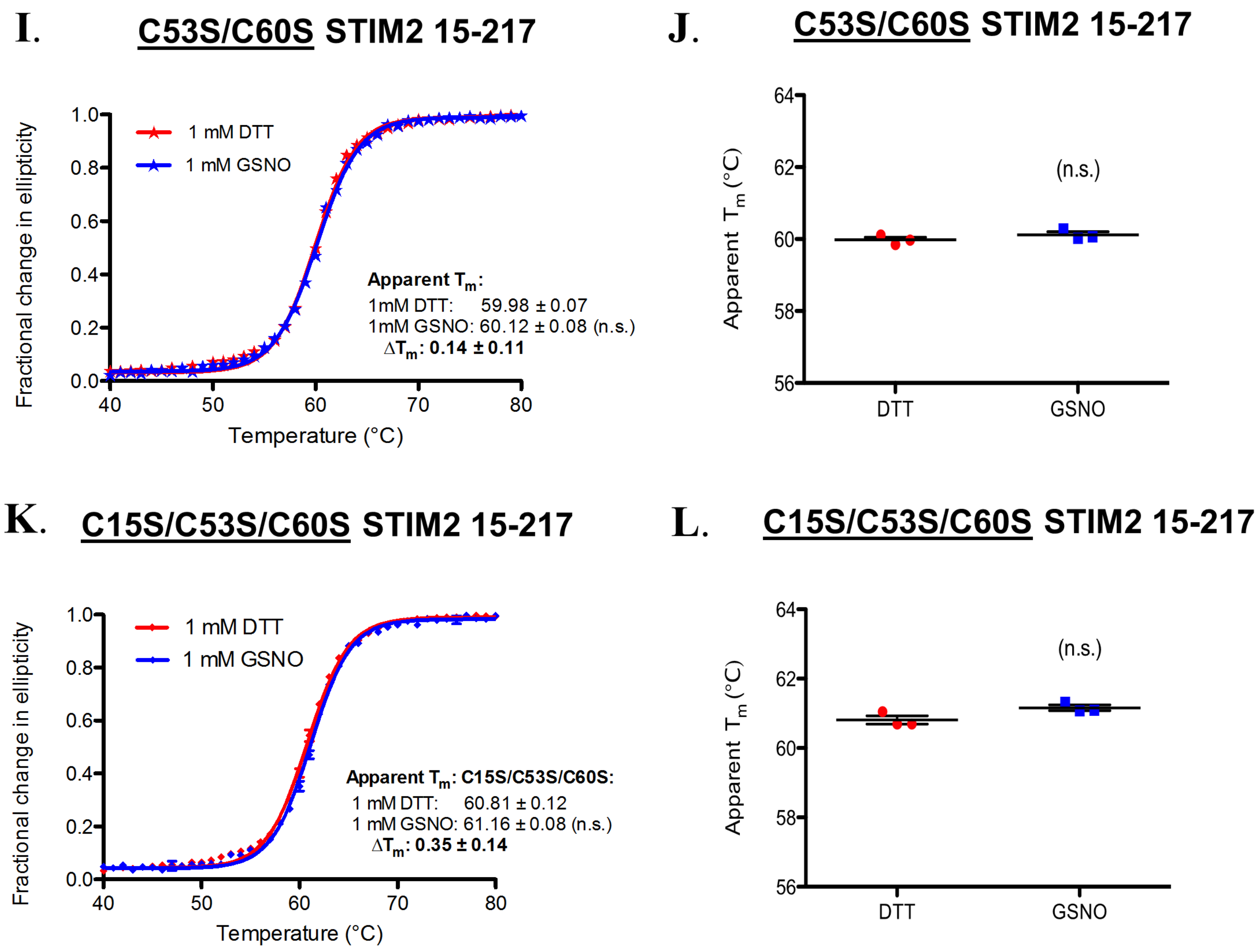

Figure. 3.6.2 Excess NO donor enhances the thermal stability of Ca^{2+} loaded STIM2 15-217 in a Cys-dependent manner. Thermal melts were acquired at 225 nm from 20 to 80 °C in a 0.1 cm pathlength cuvette using 0.5 mg mL^{-1} protein. **(A, C, E, G, I, K)** Fractional change in ellipticity and **(B, D, F, H, J, L)** apparent T$_m$ comparisons for Ca^{2+} loaded (5 mM CaCl$_2$) wildtype (WT), C15S, C53S, C60S single-mutant, C53S/C60S double-mutant, and C15S/C53S/C60S triple-mutant STIM2 15-217 protein under reducing (1 mM DTT) or *S*-nitrosylating (1 mM GSNO) conditions. Data are represented as mean ± SEM; $n = 3$ separate experiments for each group. Statistical analysis was performed using an unpaired *t*-test ($^*p < 0.05$, $^{**}p < 0.01$ against DTT control). Excess NO significantly increased the apparent T$_m$ of wildtype and C15S single mutant protein by +4.09 ± 0.66 °C and +2.41 ± 0.52 °C, respectively, significantly decreased the apparent T$_m$ of C53S and C50S single mutant proteins by -1.02 ± 0.18 °C and -1.07 ± 0.19 °C, respectively, and did not change the apparent T$_m$ of C53S/C60S double mutant or C15S/C53S/C60S triple mutant protein. Excess NO had no effect when all Cys residues present in STIM2 15-217 were mutated to Ser (*i.e.* C15S/C53S/C60S triple mutant), further suggesting a Cys-specific effect.

Table 3.1. Apparent denaturation midpoint (T_m) of wildtype, single-, double-, and triple-mutant STIM2 15-217 protein with or without Ca^{2+} and/or GSNO.

STIM2 15-217	Condition	Apparent T_m (°C) (Mean ± SEM)
Wildtype	**Ca^{2+} Depleted**	
	1 mM DTT (*n*=3)	51.71 ± 0.48
	1 mM GSNO (*n*=3)	53.41 ± 0.13 *
	$\Delta_{GSNO-DTT}$:	**+1.70 ± 0.50**
	Ca^{2+} Loaded	
	1 mM DTT (*n*=3)	63.16 ± 0.12
	1 mM GSNO (*n*=3)	67.25 ± 0.65 **
	$\Delta_{GSNO-DTT}$:	**+4.09 ± 0.66**
Single-Mutant Cys15Ser	**Ca^{2+} Loaded**	
	1 mM DTT (*n*=3)	63.35 ± 0.07
	1 mM GSNO (*n*=3)	65.77 ± 0.51 **
	$\Delta_{GSNO-DTT}$:	**+2.41 ± 0.52**
Single-Mutant Cys53Ser	**Ca^{2+} Loaded**	
	1 mM DTT (*n*=3)	63.63 ± 0.03
	1 mM GSNO (*n*=3)	62.61 ± 0.17 **
	$\Delta_{GSNO-DTT}$:	**-1.02 ± 0.18**
Single-Mutant Cys60Ser	**Ca^{2+} Loaded**	
	1 mM DTT (*n*=3)	62.03 ± 0.04
	1 mM GSNO (*n*=3)	60.96 ± 0.18 **
	$\Delta_{GSNO-DTT}$:	**-1.07 ± 0.19**
Double-Mutant Cys53/60Ser	**Ca^{2+} Loaded**	
	1 mM DTT (*n*=3)	59.98 ± 0.07
	1 mM GSNO (*n*=3)	60.12 ± 0.08 (n.s.)
	$\Delta_{GSNO-DTT}$:	**+0.14 ± 0.11**
Triple Mutant Cys15/53/60Ser	**Ca^{2+} Loaded**	
	1 mM DTT (*n*=3)	60.81 ± 0.12
	1 mM GSNO (*n*=3)	61.16 ± 0.08 (n.s.)
	$\Delta_{GSNO-DTT}$:	**+0.35 ± 0.14**

Statistical analyses were performed using a student's t-test.
*$p < 0.05$, **$p < 0.01$ versus 1 mM DTT control.

WT STIM2 15-217, Ca^{2+} Depleted

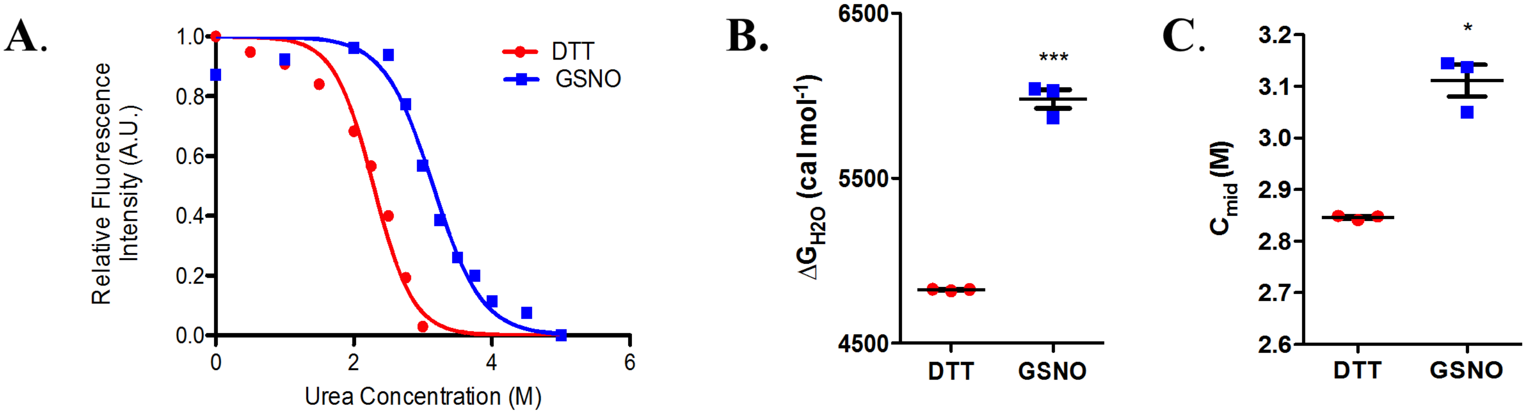

C15S STIM2 15-217, Ca^{2+} Depleted

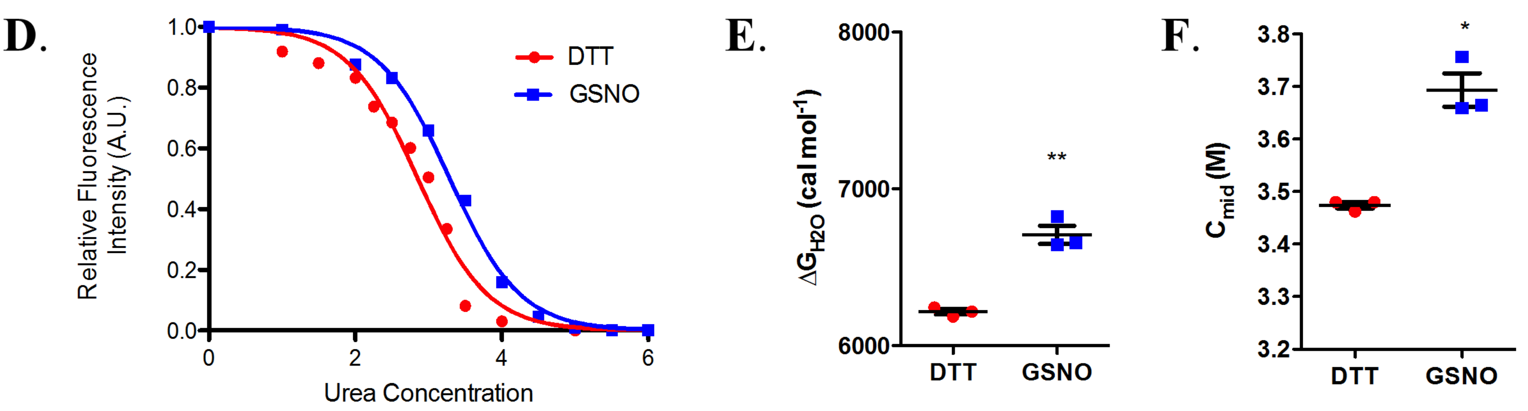

C53S/C60S STIM2 15-217, Ca^{2+} Depleted

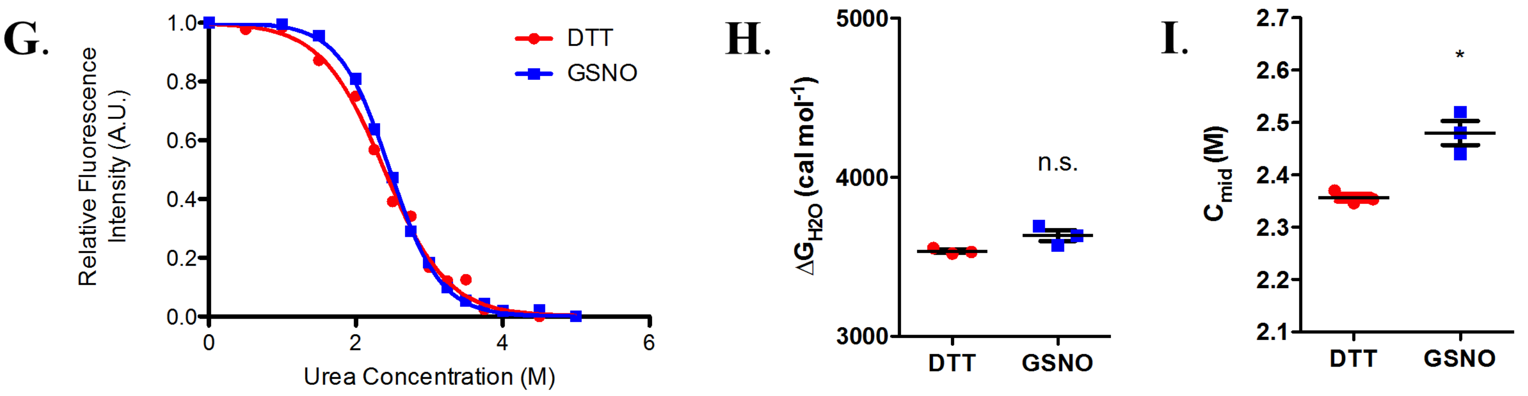

C15S/C53S/C60S STIM2 15-217, Ca^{2+} Depleted

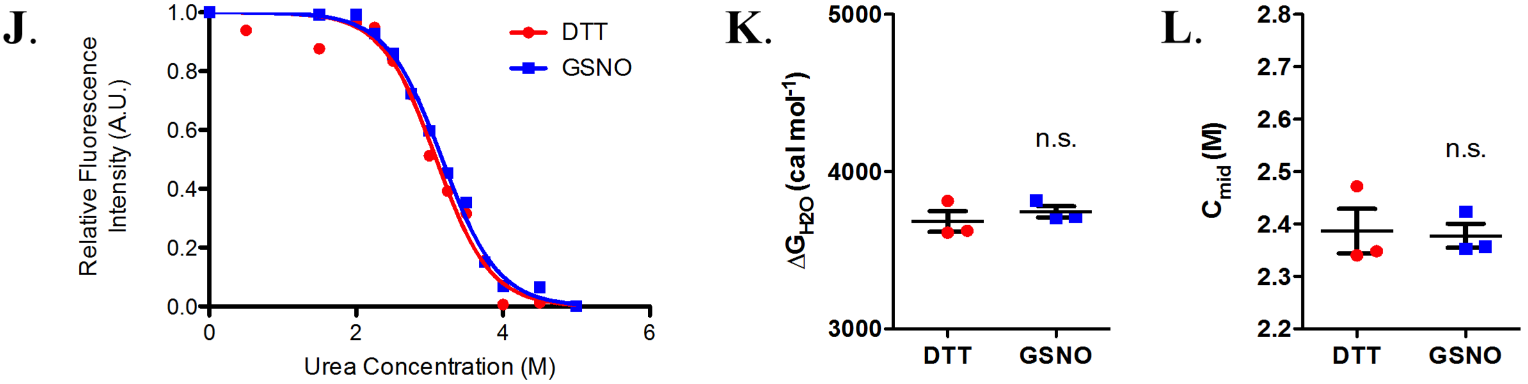

Figure. 3.6.3. Excess NO donor thermodynamically stabilizes Ca^{2+} depleted STIM2 15-217 in a Cys-dependent manner. (A, D, G, J) Representative urea denaturation curves of Ca^{2+} depleted wildtype (WT), C15S single-mutant, C53S/C60S double-mutant, and C15S/C53S/C60S triple-mutant STIM2 15-217 protein under reducing (1 mM DTT) or *S*-nitrosylating (1 mM GSNO) conditions. **(B, E, H, K)** The Gibbs free energy of unfolding in water [ΔG_{H2O} (cal mol^{-1})] for each sample was calculated using a two-state unfolding equilibrium model. **(C, F, I, L)** The midpoint of chemical denaturation (C_{mid}) was calculated by dividing ΔG_{H2O} by a globally fitted *m*-value. Data are represented as mean ± SEM; $n = 3$ separate experiments for each group. Statistical analysis was performed using an unpaired *t*-test ($^{*}p < 0.05$, $^{**}p < 0.01$ $^{***}p < 0.001$ against DTT control). Excess NO donor significantly enhances the ΔG_{H2O} and C_{mid} of both wildtype and C15S STIM2 15-217 in the Ca^{2+} depleted state, though the thermodynamic stabilization of C15S is to a lesser degree than wild-type. When only the unique Cys was available for modification (*i.e.* C53S/C60S), the thermodynamic stability of the double mutant protein was minimally affected in the presence of excess NO. Thermodynamic stability of the triple mutant STIM 15-217 protein with all modifiable Cys replaced to Ser (*i.e.* C15S/C53S/C60S) was minimally affected in the presence of excess NO, further suggesting a Cys-dependent effect.

Table 3.2. Thermodynamic stability values for wildtype and mutant STIM2 15-217 with or without Ca^{2+} and/or GSNO.

STIM2 15-217	**Condition**	**ΔG_{H2O} [kcal mol^{-1}] (Mean ± SEM)**	***m*-value [kcal mol^{-1}M^{-1}] (Mean ± SEM)**	**C_{mid} [M] (Mean ± SEM)**
Wildtype	**Ca^{2+} Loaded**			
	1 mM DTT (*n*=3)	6.87 ± 0.02	2.05 ± 0.11	3.34 ± 0.01
	1 mM GSNO (*n*=3)	7.49 ± 0.06 ***	2.00 ± 0.17	3.58 ± 0.06 *
	$\Delta_{GSNO-DTT}$:	**+0.63 ± 0.06**		**+0.24 ± 0.06**
	Ca^{2+} Depleted			
	1 mM DTT (*n*=3)	4.82 ± 0.02	1.69 ± 0.08	2.85 ± 0.01
	1 mM GSNO (*n*=3)	5.98 ± 0.06 ***	1.92 ± 0.19	3.11 ± 0.03 **
	$\Delta_{GSNO-DTT}$:	**+1.16 ± 0.06**		**+0.27 ± 0.03**
Single-Mutant Cys15Ser	**Ca^{2+} Depleted**			
	1 mM DTT (*n*=3)	6.22 ± 0.02	1.78 ± 0.12	3.47 ± 0.01
	1 mM GSNO (*n*=3)	6.71 ± 0.02 **	1.82 ± 0.27	3.69 ± 0.03 **
	$\Delta_{GSNO-DTT}$:	**+0.49 ± 0.06**		**+0.22 ± 0.03**
Double-Mutant Cys53/60Ser	**Ca^{2+} Depleted**			
	1 mM DTT (*n*=3)	3.54 ± 0.01	1.50 ± 0.07	2.36 ± 0.01
	1 mM GSNO (*n*=3)	3.63 ± 0.03 (n.s.)	1.47 ± 0.08	2.48 ± 0.02 *
	$\Delta_{GSNO-DTT}$:	**+0.10 ± 0.04**		**+0.12 ± 0.02**
Triple Mutant Cys15/53/60Ser	**Ca^{2+} Depleted**			
	1 mM DTT (*n*=3)	3.41 ± 0.17	1.54 ± 0.17	2.39 ± 0.04
	1 mM GSNO (*n*=3)	3.40 ± 0.15 (n.s.)	1.58 ± 0.11	2.38 ± 0.02 (n.s.)
	$\Delta_{GSNO-DTT}$:	**+0.01 ± 0.23**		**+0.01 ± 0.02**

Statistical analyses were performed using a student's t-test.
*$p < 0.05$, **$p < 0.01$, ***$p < 0.001$ versus. 1 mM DTT control.

3.7 Excess NO prevents intramolecular disulfide bond formation of the STIM2 15-217 luminal domain

Thiols that have undergone *S*-nitrosylation are intrinsically unstable and have the propensity to form disulfide bonds in the presence of an electron acceptor, such as reduced metals and thiols (Arnelle and Stamler, 1995; Wolhuter et al., 2018). Additionally, GSNO not only acts as an NO donor, but also provides a glutathione group that could covalently link to a thiol under oxidizing conditions. Consequentially, it is possible that disulfide bond formation or *S*-glutathionylation, rather than *S*-nitrosylation, caused the augmented stability observed herein for STIM2 15-217. Therefore, I next checked for the possibility of disulfide bond formation and *S*-glutathionylation using an SDS-PAGE mobility shift assay.

STIM2 15-217 migrates in SDS-PAGE gels slightly above its theoretical molecular weight of ~24.0 kDa due to a high enrichment of acidic residues, similar to STIM1 (Zhu et al., 2018). The presence of intramolecular disulfide bonds would increase the compactness of the protein chain resulting in higher mobility in SDS-PAGE gels. In contrast, *S*-glutathionylation would increase the molecular weight of the protein by as much as 918 Da (*i.e.* 3 moieties at 306 Da), decreasing mobility in SDS-PAGE. I prepared three wild-type STIM2 15-217 samples using the same ultrafiltration procedure I routinely used for GSNO exchange (see Section 2.3): one sample in 1 mM DTT (reducing condition), one sample in 1 mM GSNO (*S*-nitrosylating condition) and one sample containing neither GSNO nor DTT (non-reducing condition). SDS PAGE of these samples revealed a migration shift only for the protein sample in the non-reducing condition, likely reflecting intramolecular disulfide bond formation (Fig. 3.7). As a negative control, the Cys15Ser/Cys53Ser/Cys60Ser triple mutant protein was processed in the identical manner. In contrast to the increased mobility observed for the wild-type protein under non-reducing conditions, the migration of the triple mutant protein remained unchanged. Note that samples were not boiled for this experiment due to the labile nature of *S*-nitrosylation, and samples were separated by empty lanes to minimize contamination of GSNO and DTT across lanes.

Collectively, these data indicate that 1 mM GSNO is likely to favour *S*-nitrosylation of STIM2 15-217 over oxidation and *S*-glutathionylation under the buffer conditions used in this research.

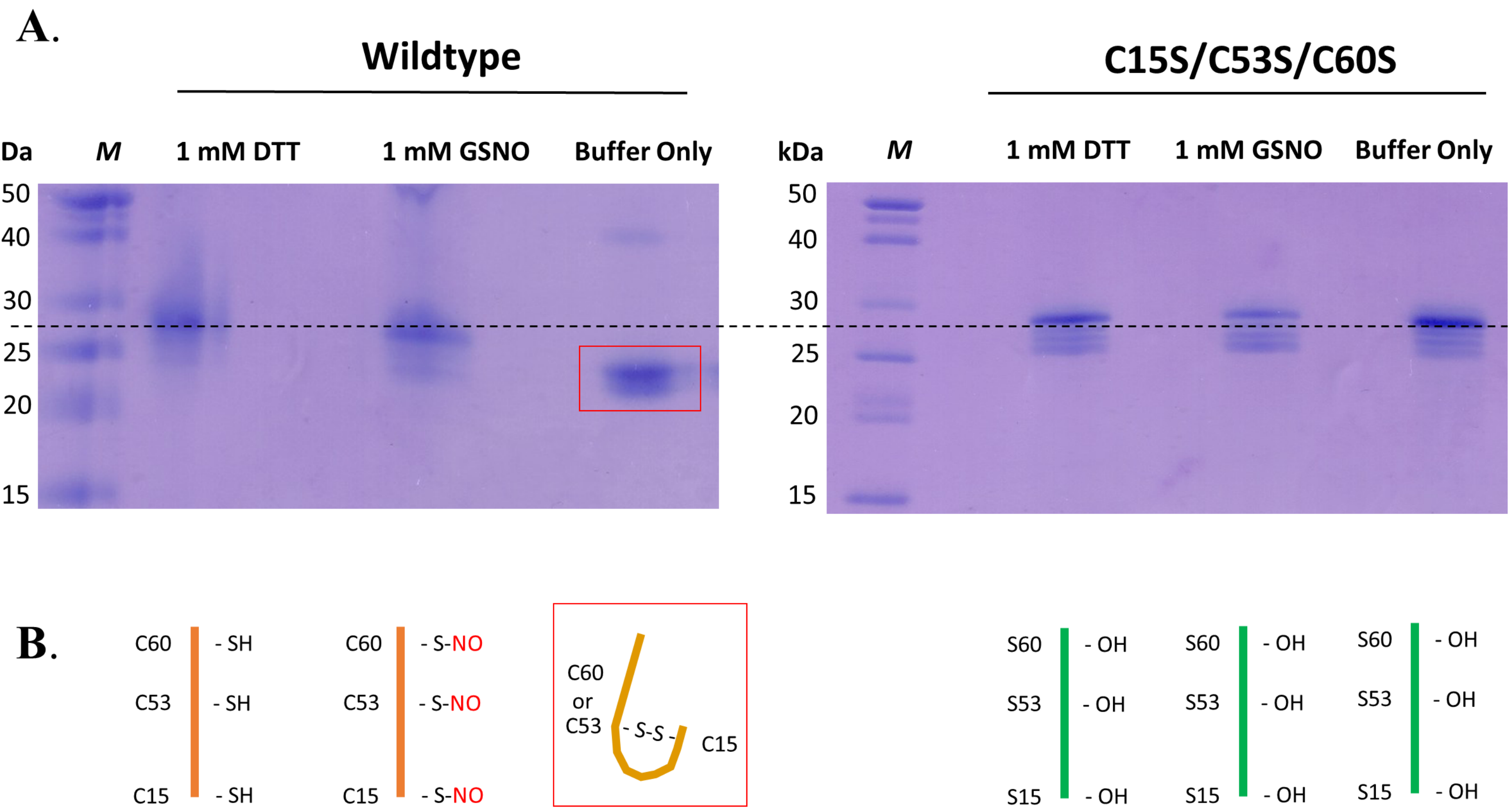

Figure. 3.7. Excess NO prevents STIM2 15-217 intramolecular luminal disulfide bond formation. (A) Wildtype and C15S/C53S/C60S triple mutant STIM2 15-217 protein were exchanged into buffers at pH = 8 containing either 20 mM TRIS-HCl and 5 mM $CaCl_2$ alone (non-reducing conditions) or supplemented with 1 mM DTT (reducing condition) or 1 mM GSNO (*S*-nitrosylating condition). Protein samples (0.25 mg/mL were separated on a 12.5 % (w/v) SDS-PAGE gel for 90 minutes and subsequently stained with Coomassie Brilliant Blue R-250 to visualize protein mobility. **(B)** Cartoon representation of the proposed modification states of wildtype and C15S/C53S/C60S triple mutant STIM2 15-217 protein in reducing, *S*-nitrosylating and non-reducing conditions. The proposed side-chain modification states in *B* are shown relative to the migration in the corresponding lane immediately above the depiction in panel *A*. The presence of an intramolecular disulfide bond is expected to increase the mobility. *S*-Glutathionylation is expected to decrease the mobility. A shift in apparent size was observed in the non-reducing condition of wildtype, but not C15S/C53S/C60S triple mutant protein, consistent with a disulfide bond. Wildtype STIM2 15-217 under *S*-nitrosylating conditions did not display a characteristic shift in apparent size compared to migration in the presence of DTT, suggesting that neither an intramolecular disulfide bond nor *S*-glutathionylation was present. No characteristic migration shift was detected for the triple-mutant under any condition. The expected theoretical monomer molecular weight of STIM2 15-217 is ~24 kDa. Samples were not boiled due to the labile nature of *S*-nitrosylation and were separated by empty lanes to minimize contamination of GSNO and DTT across lanes. *M* denotes Wide Range Protein Protein Molecular Weight Marker (BioBasic). In *A* and *B*, data are representative of 2 separate experiments.

3.8 Excess NO suppresses STIM2-mediated basal Ca^{2+} homeostasis and SOCE in live HEK293T cells

After establishing that excess GSNO causes a Cys-dependent thermodynamic stabilization concomitant with structural perturbations in the STIM2 15-217 luminal domain that is likely due to *S*-nitrosylation, I next investigated whether this effect has any functional consequences. Fura-2 ratiometric fluorimetry was used to probe basal Ca^{2+} and SOCE in HEK293T cells transiently co-overexpressing enhanced green fluorescent protein tagged Orai1 (*i.e.* eGFP-Orai1) and monomeric cherry fluorescent protein tagged STIM2 (*i.e.* mChSTIM2). Together, STIM2 and Orai1 can form and gate Ca^{2+} channels on the PM.

Cells loaded with Fura-2 (see Section 2.10) were bathed in HBSS media supplemented with 0.5 mM Ca^{2+} 24 hours after transfection, transferred into a quartz cuvette and temperature equilibrated for 10 minutes. Following this equilibration time, basal Ca^{2+} levels were measured by averaging Fura-2 fluorescence ratios over 50 s. Consistent with previous studies, cells overexpressing wild-type mChSTIM2 with eGFP-Orai1 had significantly higher basal Ca^{2+} levels when compared to control cells overexpressing monomeric cherry fluorescence protein (mCh) with eGFP-Orai1 (*i.e.* ~210 nM compared to ~117 nM, respectively; $p < 0.001$). Overnight incubation of HEK293T cells overexpressing wild-type mChSTIM2 and eGFP-Orai1 with 250 μM GSNO supplemented into the growth medium muted the basal Ca^{2+} level enhancement (Fig. 3.8.1A and 3.8.1B). To determine whether this inhibition of basal Ca^{2+} was dependent on Cys15, Cys53 and Cys60 of STIM2, similar experiments were performed using a Cys15Ser/Cys53Ser/Cys60Ser triple mutant mChSTIM2. Basal Ca^{2+} levels of HEK293T cells expressing the triple mutant STIM2 protein and eGFP-Orai1 did not significantly differ from those in control cells overexpressing mCh and eGFP-Orai1 either in the presence or absence of GSNO (Fig. 3.8.1A and 3.8.1B).

Increased basal Ca^{2+} levels mediated by STIM2 are accompanied by higher intracellular Ca^{2+} store concentrations within the ER (Brandman et al., 2007). Thus, I next assessed whether cells overexpressing mChSTIM2 had elevated ER Ca^{2+} store levels and whether GSNO affected this phenomenon. To assess ER Ca^{2+} levels, EGTA was added to the cell bathing medium to chelate all extracellular Ca^{2+}. Subsequently, 2 μM TG was used to passively deplete ER Ca^{2+} stores by blockade of SERCA pumps. Since basal Ca^{2+} levels differed among groups, the Fura-2 response was normalized as F/F_0 to determine the fractional increase in cytosolic Ca^{2+} over baseline induced by TG, where F and F_0 are the Fura-2 fluorescence ratios after and before (*i.e.* baseline) the addition of TG, respectively. Consistent with my observation that cells overexpressing wild-type mChSTIM2 and eGFP-Orai1 exhibited higher basal Ca^{2+} levels, this same group displayed a significantly higher TG-induced ER Ca^{2+} release when compared to control cells overexpressing mCh and eGFP-Orai1. Furthermore, overnight treatment with 250 μM GSNO attenuated this enhancement back to control levels (Fig. 3.8.2A and 3.8.2B). Also in agreement with my basal Ca^{2+} measurements, the TG-induced ER Ca^{2+} release from cells overexpressing the Cys15Ser/Cys53Ser/Cys60Ser triple mutant mChSTIM2 and eGFP-Orai1 did not significantly differ from the control cells and was not affected by GSNO.

While STIM2 chiefly regulates basal Ca^{2+} levels, it also mediates SOCE, albeit to a lesser degree compared to STIM1 in HEK293T cells (Emrich et al., 2019). To assess SOCE, 2 mM of net Ca^{2+} was added back to the extracellular medium to elicit influx into the cytosol through PM Orai1 channels. As anticipated, cells overexpressing wild-type mChSTIM2 and eGFP-Orai1 displayed significantly higher levels of SOCE compared to control cells overexpressing mCh and eGFP-Orai1 (Fig. 3.8.2A and 3.8.2C). As observed with basal and ER stored Ca^{2+} release, overnight incubation of wild-type mChSTIM2 and eGFP-Orai1 expressing cells with 250 μM GSNO abrogated this SOCE enhancement (Fig. 3.8.2A and 3.8.2C). Cells overexpressing the Cys15Ser/Cys53Ser/Cys60Ser triple mutant mChSTIM2 and eGFP-Orai1 failed to elicit SOCE above levels observed in the control group with and without GSNO treatment.

Note that similar experiments were attempted with single Cys15Ser and double Cys53Ser/Cys60Ser mutant versions of mChSTIM2. However, for unknown reasons, a low proportion of these cell suspensions responded to TG (*i.e.* < 20%), and cell preparations that did respond exhibited atypical release from ER stores and high variability in the level of SOCE. Thus, these groups were not included in the analysis.

To ensure that the changes in Fura ratios mediated by mChSTIM2 and eGFP-Orai1 were not due to differences in protein expression levels, eGFP and mCh fluorescence emission spectra of the cell suspensions were acquired. My laboratory has previously shown that mChSTIM1 fluorescence correlates with protein expression levels via western blotting (Zhu et al., 2018). Here, eGFP-Orai1 fluorescence did not differ significantly among all groups tested, regardless of GSNO incubation (Fig. 3.8.2D). Due to the cytosolic localization, cells expressing mCh showed significantly higher mCh fluorescence compared to cells expressing mChSTIM2 proteins that were inserted into the ER membrane (Fig. 3.8.2E). However, GSNO did not affect the expression levels of either the mCh or mChSTIM2 proteins.

Taken together, these results demonstrate that GSNO alters STIM2-mediated basal Ca^{2+} homeostasis concomitant with decreased ER Ca^{2+} stores, as well as SOCE activation, which is consistent with the GSNO mediated thermal and thermodynamic stabilization of the STIM2 luminal domain. Additionally, these cell experiments reveal a remarkable sensitivity of STIM2 function to variations in the three Cys residues located in the luminal domain.

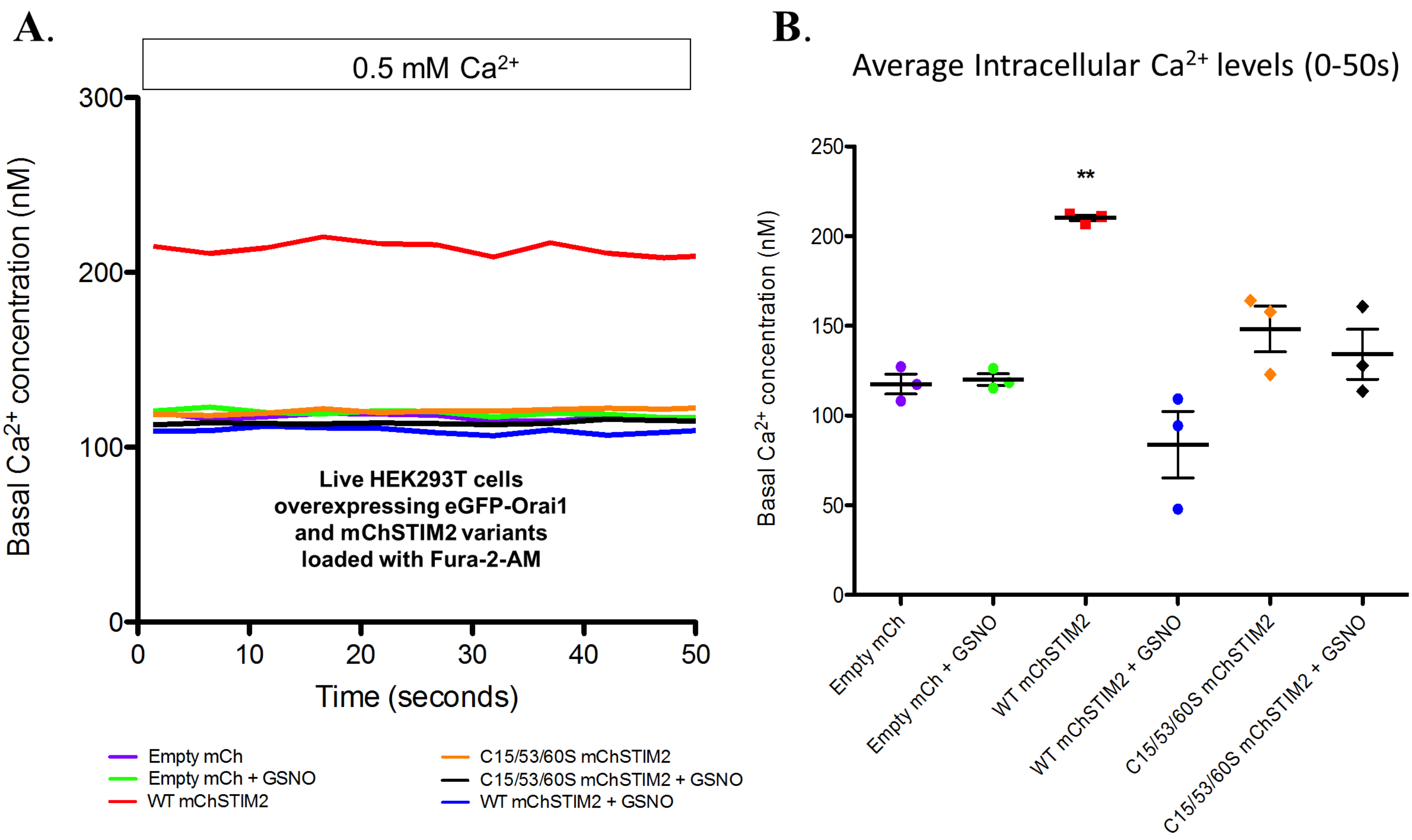

Figure. 3.8.1. Excess NO donor suppresses STIM2-mediated basal Ca^{2+} homeostasis in live HEK293T cells transiently co-overexpressing eGFP-Orai1 and mChSTIM2. (A) Representative Fura-2 ratiometric fluorescence traces reporting calibrated resting intracellular Ca^{2+} concentrations (nM). The cells were temperature equilibrated in HBSS buffer supplemented with 0.5 mM Ca^{2+} at 22.5 °C for 10 minutes prior to measurement. **(B)** Average intracellular Ca^{2+} levels over 50s. In *A* and *B*, wildtype (WT) STIM2 data are coloured red and blue and C15S/C53S/C60S triple mutant STIM2 are coloured orange and black for cells incubated in the absence and presence of GSNO, respectively. In *B*, the data are reported as means ± SEM; $n = 3$ separate experiments. **, $p < 0.01$ versus empty control mCh using One-way ANOVA and Tukey's multiple comparisons test.

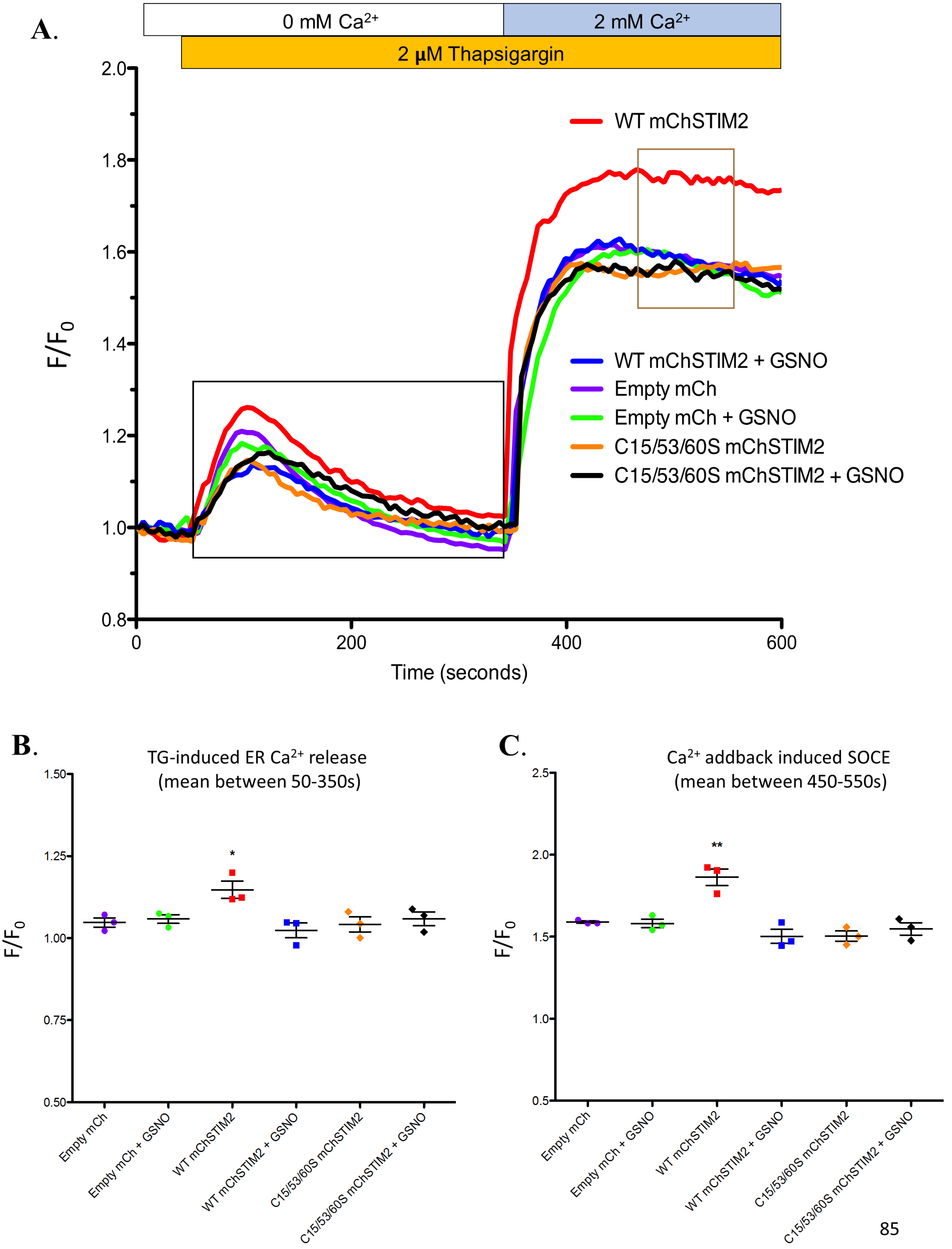
A.
0 mM Ca²⁺
2 mM Ca²⁺
2 µM Thapsigargin
WT mChSTIM2
WT mChSTIM2 + GSNO
Empty mCh
Empty mCh + GSNO
C15/53/60S mChSTIM2
C15/53/60S mChSTIM2 + GSNO
F/F0
Time (seconds)
0.8
1.0
1.2
1.4
1.6
1.8
2.0
0
200
400
600
B.
TG-induced ER Ca²⁺ release
(mean between 50-350s)
F/F0
0.50
0.75
1.00
1.25
1.50
*
Empty mCh
Empty mCh + GSNO
WT mChSTIM2
WT mChSTIM2 + GSNO
C15/53/60S mChSTIM2
C15/53/60S mChSTIM2 + GSNO
C.
Ca²⁺ addback induced SOCE
(mean between 450-550s)
F/F0
0.5
1.0
1.5
2.0
2.5
**
Empty mCh
Empty mCh + GSNO
WT mChSTIM2
WT mChSTIM2 + GSNO
C15/53/60S mChSTIM2
C15/53/60S mChSTIM2 + GSNO

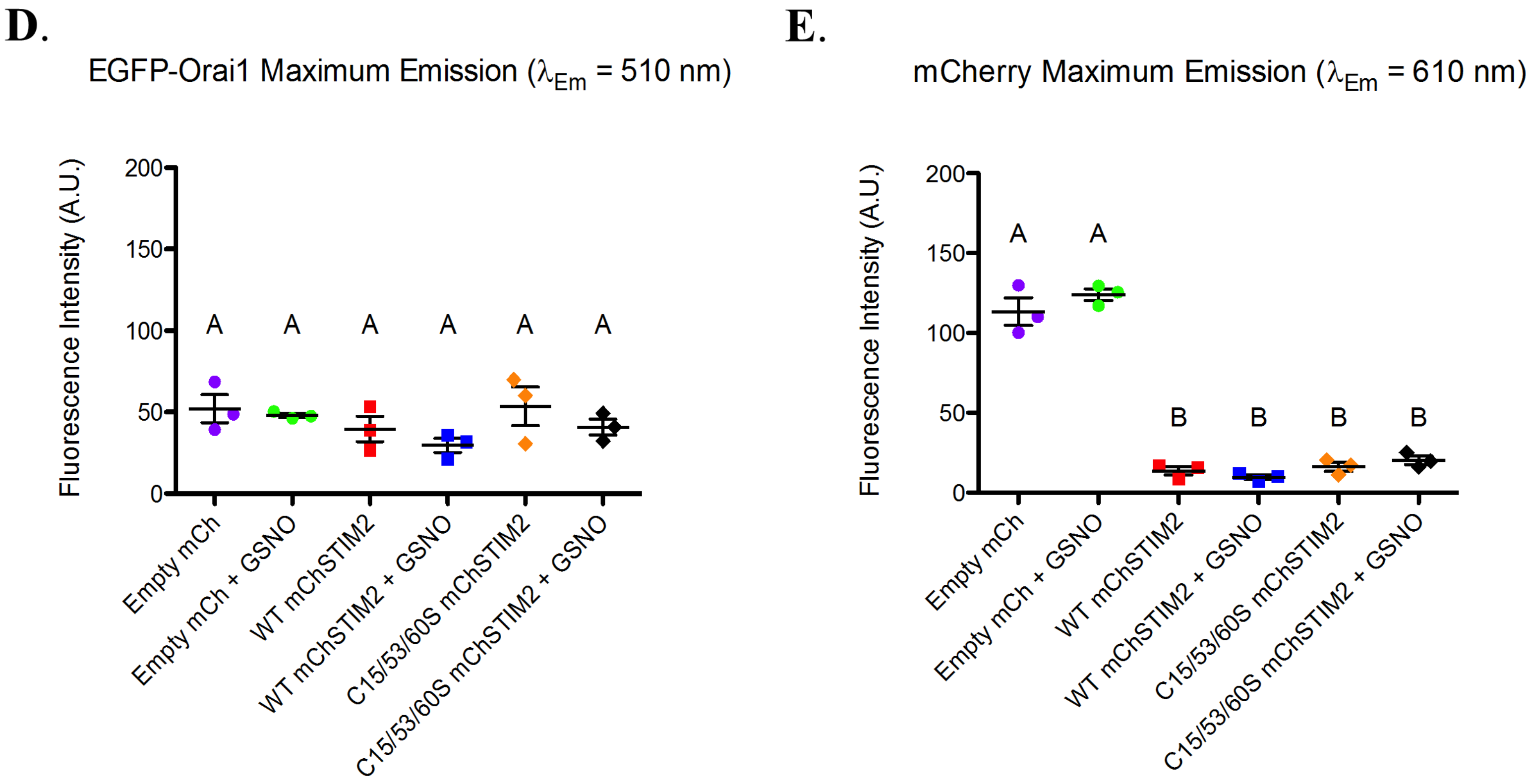

Figure. 3.8.2. Excess NO donor suppresses STIM2-mediated SOCE in live HEK293T cells transiently co-overexpressing eGFP-Orai1 and mChSTIM2. (A) Representative Fura-2 ratiometric fluorescence traces reporting relative changes in intracellular Ca^{2+} levels. The relative change in Fura-2 fluorescence was monitored after 2 µM thapsigargin (black box) and subsequently 2 mM Ca^{2+} additions to the extracellular media (brown box). **(B)** Average TG-induced ER Ca^{2+} release (*i.e.* average F/F_0 taken after TG addition in 0 mM extracellular Ca^{2+} for 300s). **(C)** Average SOCE taken after 2 mM extracellular Ca^{2+} addback for 100s. **(D)** Maximum eGFP fluorescence emission of cell suspensions ($\lambda_{excitation} = 470$ nm, $\lambda_{emission} = 510$ nm). **(E)** Maximum mCh fluorescence emission of cell suspensions ($\lambda_{excitation} = 565$ nm, $\lambda_{emission} = 610$ nm). In *A-E*, wildtype (WT) mChSTIM2 data are coloured red and blue and C15S/C53S/C60S triple mutant STIM2 are coloured orange and black for cells incubated in the absence and presence of GSNO, respectively. Data in *B-E* are reported as means ± SEM; $n = 3$ separate experiments. All statistical analyses were performed using One-way ANOVA and Tukey's multiple comparisons test. In *B* and *C*, * $p < 0.05$ and ** $p < 0.01$. In *D* and *E*, groups with the same letters are not significantly different from one another.

Chapter 4: Discussion

4.1. Summary

Hyperactivation of the STIM-mediated SOCE pathway results in dysregulated Ca^{2+} homeostasis, underlying many pathological conditions including cardiovascular and neurodegenerative diseases (Luo et al., 2012; Secondo et al., 2018). Recent evidence demonstrates that *S*-nitrosylating conditions increase STIM1 full luminal domain protein stability, suppress Ca^{2+} dependent STIM1 oligomerization and inhibit SOCE by maintaining a quiescent STIM1 luminal domain conformation by promoting interactions between the variable N-terminal region and the EFSAM core (Zhu et al., 2018). Here, my data reveals that the STIM2 luminal domain is also sensitive to *S*-nitrosylation promoting conditions, exhibiting changes in stability, structure and function in the presence of excess NO donor. In contrast to STIM1 which contains two modifiable Cys residues, STIM2 contains three modifiable Cys residues within the luminal domain (*i.e.* Cys49 and Cys56 compared to Cys15, Cys53 and Cys60, respectively). My data suggest that all three of these Cys residues play a role in modulating STIM2 biophysical attributes due to *S*-nitrosylation. Specifically, the NO donor GSNO promotes a STIM2 luminal domain migration on SDS-PAGE that is most consistent with *S*-nitrosylation, when compared to protein with intramolecular disulfides or the expected migration of *S*-glutathionylated protein. Further, I show that these *S*-nitrosylation favouring conditions thermally and thermodynamically stabilize the domain via new or changed interactions between the STIM2 variable N-terminal region and one face of the EFSAM core. Importantly, the effects at the biophysical and structural levels were Cys-dependent, and loss of the unique Cys residue to STIM2 (*i.e.* Cys15) attenuated excess GSNO induced stabilization compared to wildtype protein. Interestingly, Cys15 alone failed to induce STIM2 luminal domain stabilization in the presence of excess GSNO, suggesting that Cys15 mediates an increase in protein stability that is dependent on Cys53 and Cys60 residues in the presence of excess NO. I propose that, under *S*-nitrosylating conditions, Cys53 and Cys60 work in concert to interact with one side of the EFSAM core (*i.e.* residues 62-206) such that Cys15 is brought into close apposition to the same region, facilitating further interactions and protein stabilization.

Consistent with my work using the isolated STIM2 luminal domain, I found that GSNO attenuates full-length STIM2 mediated basal Ca^{2+} homeostasis and SOCE in mammalian HEK293T cells. Interestingly, full length STIM2 protein with all three modifiable Cys residues in the variable N-terminal region mutated to Ser (*i.e.* Cys15Ser/Cys53Ser/Cys60Ser) failed to elicit SOCE and increase basal Ca^{2+} levels associated with increased ER Ca^{2+} stores, highlighting the functional sensitivity of the molecule to variations at these residue positions. Ultimately, my work suggests that excess GSNO promotes *S*-nitrosylation, which can attenuate STIM2-mediated basal Ca^{2+} levels and SOCE by stabilizing the full luminal domain via specific interactions between nitrosylated Cys residues within the variable N-terminal region and one face of the EFSAM core.

4.2. Excess NO promoted protein *S*-nitrosylation

S-Nitrosylation is a transient and reversible post-translational modification, where an NO moiety is covalently attached to the sulfur atom of a Cys residue to form *S*-nitrosothiols (*i.e.* –SNO groups). *S*-Nitrosothiol formation is thought to occur via a recombination between a thiyl radical and NO or via oxidation of NO to N_2O_3 in the presence of an electron acceptor (Broniowska and Hogg, 2012; Madej et al., 2008). While the exact mechanism by which endogenous *S*-nitrosothiols form remains largely unknown, protein *S*-nitrosylation in the presence of NO is well supported by several lines of evidence. First, different types of NO donors have been used to demonstrate *S*-nitrosylation of STIM1 including sodium nitroprusside (SNP) and GSNO. Second, *in vitro* NO donor promoted *S*-nitrosylation occurs in a concentration-dependent manner. In other words, lower concentrations (*i.e.* 1 mM) of SNP were shown to have a smaller biophysical effect than higher concentrations (*i.e.* 2 mM) (Zhu et al., 2018). Third, neuronal NOS was shown to co-localize with its target protein in neuronal synapses to produce NO thereby promoting protein *S*-nitrosylation (Dejanovic and Schwarz, 2014). Fourth, *in vivo* knockout mice models of neuronal NOS decreased cellular NO levels concomitant with a decrease in protein *S*-nitrosylation (Burger et al., 2009). Fifth, nNOS knockout cardiomyocytes show no evidence for STIM1 *S*-nitrosylation whereas cardiomyocytes from wild-type mice show *S*-nitrosylated STIM1 (Gui et al., 2018). Thus, the presence of NO promotes protein *S*-nitrosylation both *in vitro* and *in vivo*, despite the chemical mechanism being poorly understood.

In my current study, I utilized molar excess amounts of the NO donor, GSNO, to promote *S*-nitrosylation of STIM2 at Cys15, Cys53, and Cys60 *in vitro*. The use of excess GSNO as a treatment to successfully promote *S*-nitrosylation has been previously used in the literature (Bocedi et al., 2004; Erickson et al., 2015; Feng et al., 2011; Hao et al., 2004) and by my lab (Zhu et al., 2018). Despite the well-established use of GSNO treatment to promote *S*-nitrosylation induced structural and functional effects on proteins, reports suggest that disulfide bond formation, rather than *S*-nitrosylation, could underlie the observed changes in protein function (Wolhuter et al., 2018). Moreover, GSNO treatment can also promote another protein post-translational modification, *S*-glutathionylation, by donating a glutathione moiety. However, *S*-glutathionylation by GSNO is a much slower reaction and is thermodynamically unfavourable (Hawkins et al., 2010). Additionally *S*-glutathionylation has been shown to destabilize the luminal domain of STIM1 (Hawkins et al., 2010). Nevertheless, in order to confirm that the biophysical and functional effects in my study were due to excess GSNO promoted *S*-nitrosylation and not disulfide bond formation or *S*-glutathionylation, a mobility assay was devised, relying on the phenomena that intramolecular disulfide bonds increase protein mobility while *S*-glutathionylation decrease protein mobility (Betz, 1993). For this mobility assay, I used the same ultrafiltration process to exchange the samples into reducing, non-reducing and *S*-nitrosylation favouring conditions. Indeed, GSNO treatment did not affect wildtype STIM2 15-217 protein mobility, suggesting that GSNO prevented intramolecular disulfide bond formation and *S*-glutathionylation. On the contrary, the absence of DTT or GSNO (*i.e.* buffer alone; non-reducing conditions) noticeably increased the mobility of wildtype STIM2 15-217 protein, consistent with the formation of an intramolecular disulfide bond (Fig. 3.7). Therefore, GSNO treatment prevented wildtype STIM2 15-217 intramolecular disulfide bond formation, and there was no evidence for decreased mobility caused by *S*-glutathionylation, collectively suggesting that the biophysical and functional effects detected in my study were mediated by STIM2 *S*-nitrosylation due to the presence of excess NO.

My data demonstrating that luminal domain *S*-nitrosylation by GSNO treatment, rather than disulfide bond formation or *S*-glutathionylation, is the primary modification regulating STIM2 structure and function is well supported by published literature. Disulfide bond formation in the luminal domain of STIM1 (*i.e.* Cys49-Cys56) has been demonstrated to enhance, rather than inhibit, STIM1 mediated SOCE (Prins et al., 2011). Similarly, *S*-glutathionylation promotes STIM1-mediated SOCE (Hawkins et al., 2010). Consistent with the results of my mobility assay, STIM1 proteins from heart tissue homogenates of wildtype mice, but not eNOS$^{-/-}$ or nNOS$^{-/-}$ mice, show a mobility shift under non-reducing conditions, in agreement with intramolecular disulfide bond formation (Gui et al., 2018).

4.3. Biophysical comparison of the full luminal domain between STIM homologs in the presence of NO

The Ca^{2+} sensing luminal domain of STIM2 (*i.e.* 15-217) becomes activated upon ER luminal Ca^{2+} depletion and adopts a destabilized conformation, which ultimately triggers downstream SOCE activation (Stathopulos et al., 2013; Stathopulos et al., 2009; Stathopulos et al., 2008b; Zheng et al., 2008). Thus, modifications affecting luminal domain stability can profoundly impact STIM2 activity.

My investigation demonstrated that the highly α-helical structure of the full luminal domain of STIM2 is attenuated upon Ca^{2+} depletion (Fig. 3.1A), congruent with previous studies demonstrating that a loss in α-helical structure is associated with STIM2 activation (Stathopulos and Ikura, 2013b; Stathopulos et al., 2009; Zheng et al., 2008). In agreement with my secondary structure analysis, Ca^{2+} depletion markedly decreased the thermal and thermodynamic stability of wildtype STIM 15-217. Treatment with GSNO to promote *S*-nitrosylation at Cys15, Cys53 and Cys60 significantly increased both the thermal and thermodynamic stability compared to the respective reduced sulfhydryl condition in both Ca^{2+} replete and deplete conditions (Fig. 3.2.1 and 3.2.2). The increased thermodynamic stability is more apparent under Ca^{2+} depleted states, when the majority of STIM2 molecules become activated. To confirm that the enhanced stabilization was mediated by *S*-nitrosylation of Cys15, Cys53, and Cys60, a triple mutant STIM2 15-217 protein with all Cys residues mutated to Ser (*i.e.* Cys15Ser/Cys53Ser/Cys60Ser) was created, effectively removing all modifiable sulfhydryls. Despite the triple mutation producing an inherent thermal and thermodynamic destabilization compared to wildtype protein, the thermal and thermodynamic stability of this triple mutant STIM2 15-217 was not affected by GSNO treatment (Fig. 3.6.2F 3.6.2L and Fig. 3.6.3D 3.6.3H 3.6.3L), suggesting that the excess GSNO induced stabilization reported in this thesis is Cys specific.

Because equilibrium chemical denaturation of the STIM2 luminal domain is reversible, thermodynamic stability parameters, such as ΔG_{H2O}, were estimated using a two-state, folded to unfolded model. The Feng and Stathopulos groups have previously employed the same experimental model to compare the thermodynamic stability of the full luminal domain of STIM1 (*i.e*. residues 23-213) under reducing and *S*-nitrosylating conditions (*i.e*. residues 23-213) (Zhu et al., 2018), thus making STIM1-STIM2 comparative analyses feasible. In the absence of Ca^{2+}, STIM2 EFSAM retains a well folded structure compared to unstructured STIM1 EFSAM (Zheng et al., 2008). Moreover, previous urea-induced kinetics of unfolding studies indicate that Ca^{2+} loaded STIM1 EFSAM unfolds significantly faster than STIM2 EFSAM (Stathopulos et al., 2009). In agreement with these phenomena, reduced STIM2 15-217 displays a higher ΔG_{H2O} compared to reduced STIM1 23-213, in both Ca^{2+} replete (*i.e.* 6.87 kcal/mol versus 5.91 kcal/mol, respectively) and deplete (*i.e.* 4.82 kcal/mol versus 1.73 kcal/mol) conditions (Zhu et al., 2018). Interestingly, excess NO enhanced the thermodynamic stability of the STIM1 luminal domain to a larger degree compared to the STIM2 luminal domains in both Ca^{2+} replete (*i.e.* $\Delta\Delta G_{H2O}$ = +1.9 kcal/mol versus $\Delta\Delta G_{H2O}$ = +0.63 kcal/mol) and deplete (*i.e.* $\Delta\Delta G_{H2O}$ = +1.6 kcal/mol versus $\Delta\Delta G_{H2O}$ = +1.2 kcal/mol) conditions (Zhu et al., 2018).

GSNO promotes *S*-nitrosylation of both Cys49 and Cys56 in STIM1, which enhances the thermodynamic stability of the full luminal domain (*i.e.* residues 23-213) (Zhu et al., 2018). Interestingly, either Cys49Ser or Cys56Ser STIM1 23-213 single mutations abrogate any GSNO-mediated detectable changes in thermal stability of the isolated luminal domain; however, separately integrating these single mutations into full-length STIM1 diminishes the NO-mediated suppression of CRAC entry and simultaneously introducing both mutations is required to completely abolish the NO-mediated suppression of CRAC entry measured using whole cell patch clamp electrophysiology experiments (Gui et al., 2018). Based on my data, this stabilization of STIM1 is analogous to that of STIM2, despite STIM2 containing an additional modifiable Cys residue within this domain (*i.e.* Cys15, Cys53 and Cys60 in STIM2 as opposed to Cys49 and Cys56 in STIM1). I found that mutating the additional modifiable Cys in STIM2 (*i.e.* Cys15Ser) attenuated the GSNO-mediated thermodynamic stabilization of Ca^{2+} depleted single-mutant STIM2 15-217 compared to wildtype protein (*i.e.* $\Delta\Delta G_{H2O}$ = +0.49 kcal/mol versus +1.16 kcal/mol). To my surprise, when only the unique Cys15 was available for modification (*i.e.* Cys53Ser/Cys60Ser), *S*-nitrosylating conditions failed to thermodynamically stabilize the Ca^{2+} depleted double-mutant STIM2 15-217 protein. It is likely that, in conditions with excess NO, Cys15 mediates an increase in protein thermodynamic stability which is dependent on Cys53 and

Cys60, essentially serving as a supplemental modification site to further stabilize STIM2 15-217. Alternatively, as observed for STIM1, it is possible that my *in vitro* stability assays lack the sensitivity to detect differences and other analyses such as functional electrophysiological experiments are required to reveal any differences with single mutant proteins. Nevertheless, my study reveals that the supplemental post-translational modification site specific to the STIM2 paralog is modifiable and may contribute to differential regulation between STIM proteins endogenously.

Having observed that excess NO mediates enhanced stability, the effects of GSNO treatment on STIM2 full luminal domain oligomerization propensity and exposed hydrophobicity were also explored using the same experimental techniques and parameters previously used to study the full luminal domain of STIM1 in the presence of excess NO (Zhu et al., 2018). While excess NO mediated clear de-oligomerization of the Ca^{2+} depleted STIM1 luminal domain concomitant with a decrease in the level of solvent exposed hydrophobicity (Zhu et al., 2018), these phenomena were not observed for the STIM2 luminal domain under similar conditions. My inability to detect an effect of NO on these properties may be related to the much more modest changes in solvent accessible hydrophobicity (*i.e.* ~4-fold enhancement in ANS fluorescence intensity for STIM1 compared to ~1.2-fold enhancement for STIM2) and oligomerization state (*i.e.* distribution of hydrodynamic radii centered at ~10 nm for STIM1 compared to ~5 nm for STIM2) caused by Ca^{2+} depletion (Zhu et al., 2018).

4.4. Structural mechanism by which excess NO stabilizes the full luminal domain of STIM2

Previous studies indicate that *S*-nitrosylation profoundly affects the structure of proteins. It has been demonstrated that *S*-nitrosylation of the cytoplasmic rhodanese domain at Cys63 from the *E. coli* membrane bound sulfur-transferase protein (YgaP) elicits structural alterations associated with enhanced protein stability (Eichmann et al., 2016). Specifically, NMR spectroscopy demonstrated that *S*-nitrosylation of rhodanese disrupts the electrostatically unstable interaction between the C-terminal α5 helix and the active site, thus enhancing stability (Eichmann et al., 2016). In a more recent study, spectroscopic techniques revealed that *S*-nitrosylation of galectin-2 (Gal-2) at Cys57 increases thermal stability concomitant with structural alterations (Sakakura et al., 2018). Similar to my thermal stability assessment, CD spectroscopy determined that *S*-nitrosylation mediated an increase in protein thermal stability of Gal-2 by ~+5 °C compared to unmodified protein (Sakakura et al., 2018). This enhanced thermal stability was mediated by *S*-nitrosylation induced structural changes detected by NMR spectroscopy, wherein stabilization of the hydrophobic pocket around Cys57 prevents oxidation induced destabilization (Sakakura et al., 2018).

Likewise, I utilized solution NMR spectroscopy to characterize the structural changes associated with STIM2 15-217 thermal and thermodynamic stabilization after GSNO treatment. The presence of excess NO induced structural changes downstream of the variable N-terminal region, which largely clustered on the entering helix of the canonical EF-hand and on the exiting helix of the non-canonical EF-hand and the adjacent SAM linking helix (Fig. 3.5A and 3.5B). Mapping the CSPs on the surface of the STIM2 EFSAM structure revealed that a majority of these residues are localized to one face of the EFSAM core (Fig. 3.5D). These data indicate that the variable N-terminal region encompassing the three modifiable Cys sulfhydryls may be looping around to interact with one face of the EFSAM core, which ultimately promotes enhanced thermodynamic stability of the entire luminal domain (Fig 4.1A). The presence of excess NO may be either mediating new interactions between these regions or changing the interactions between these regions in some manner to facilitate the enhanced thermodynamic stability. Remarkably, the STIM2 interface identified in my study using CSP mapping is the analogous to the interface identified in NMR experiments of isolated STIM1 variable N-terminal peptides titrated into solutions of EFSAM core proteins (Zhu et al., 2018).

Because excess NO thermodynamically stabilizes wildtype STIM2 15-217 to a larger degree compared to Cys15Ser STIM2 15-217, it is likely that the loss of the Cys15 modifiable sulfhydryl perturbs the interaction of this residue with the EFSAM core, mediating a relatively decreased thermodynamic stability enhancement of single mutant STIM2 luminal domain protein in the presence of excess NO (Fig. 4.1B). On the other hand, STIM2 15-217 protein with only the unique Cys15 sulfhydryl available for *S*-nitrosylation (*i.e.* Cys53Ser/Cys60Ser double mutant protein) appeared thermodynamically insensitive to excess GSNO treatment (Fig. 3.6.3G-I), suggesting that the changes mediated by Cys15 are dependent on the interaction of Cys53 and Cys60 with the EFSAM core in the presence of excess NO (Fig. 4.2C). When all modifiable Cys sulfhydryls were mutated (*i.e.* Cys15Ser/Cys53Ser/Cys60Ser triple mutant protein), excess GSNO treatment did not affect thermodynamic stability (Fig. 3.6.3J-L), suggesting that the NO mediated structural perturbations which enhance STIM2 luminal domain stability are Cys-specific (Fig. 4.2D).

It is interesting to note that STIM1 disulfide bond formation between Cys49 and Cys56 destabilizes this protein, thereby enhancing STIM1-mediated SOCE (Prins et al., 2011). The luminal domain of STIM proteins are located within the moderately oxidizing environment of the ER. As opposed to the cytosol, the ER contains a relatively higher ratio of oxidized glutathione (*i.e.* GSSG) to reduced glutathione (*i.e.* GSH), which is conducive for protein disulfide bond formation, required for nascent protein folding of numerous proteins. Perhaps the structural perturbations demonstrated by excess GSNO treatment not only served to stabilize the full luminal domain of STIM2, but also promoted a conformation which is unfavourable for disulfide bond formation, thereby preventing potential STIM2 activation mediated by intramolecular luminal disulfide bond formation.

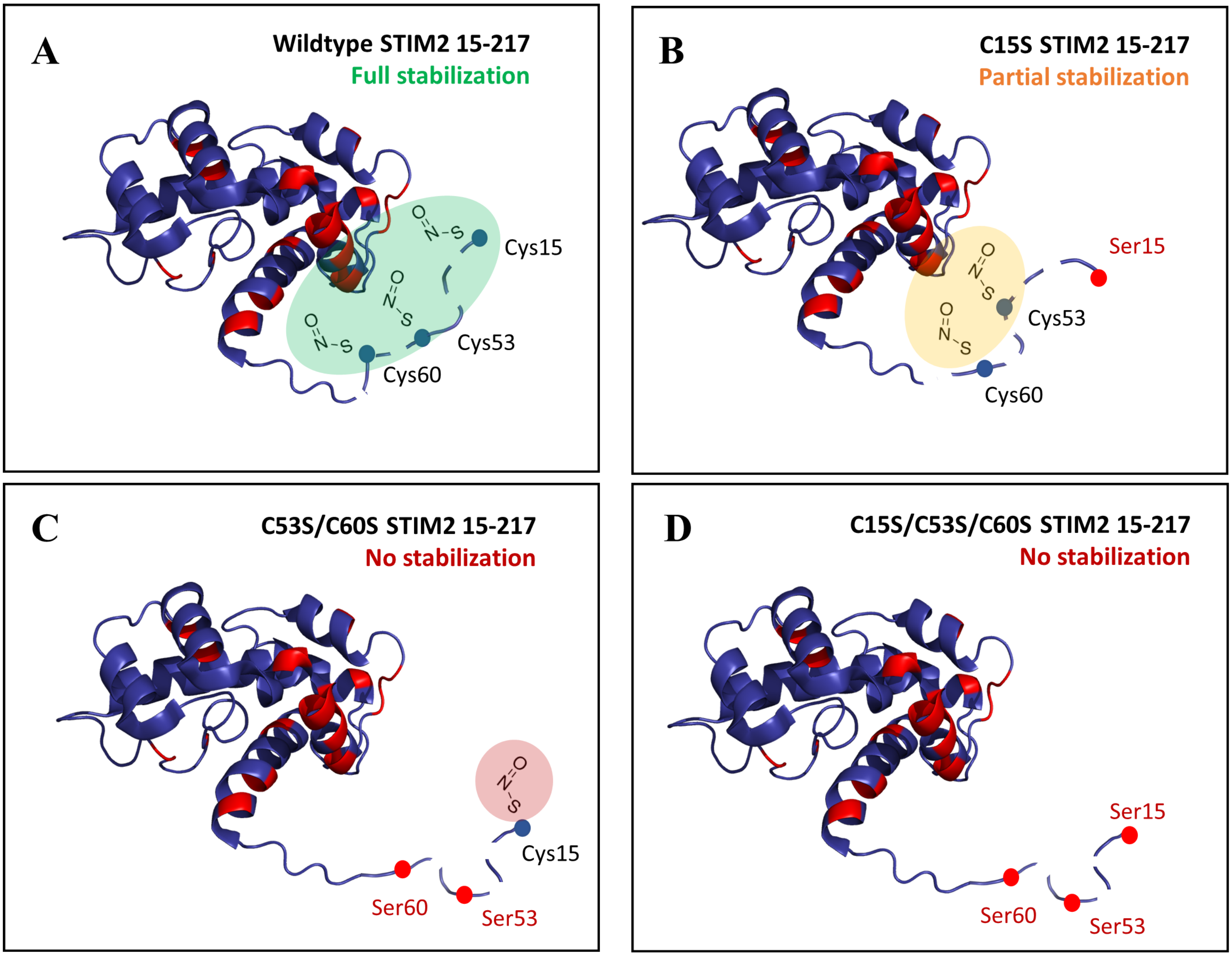

Figure. 4.1. Proposed structural mechanism of excess NO mediated thermodynamic stabilization of the STIM2 full luminal domain (i.e. residues 15-217) in the absence of Ca^{2+}. (A) Because the *S*-nitrosylation modifiable sites (i.e. residues Cys15, Cys53, and Cys60) within the intrinsically disordered variable N-terminal region (i.e. residues 15-66) are proximal to the EFSAM core (i.e. residues 62-205), it is likely that in the presence of excess NO, the variable N-terminal region loops around to form new or alter the nature of contacts with one side of the EFSAM core, ultimately enhancing thermodynamic stability. **(B)** Since excess NO thermodynamically stabilizes wildtype STIM2 15-217 to a larger degree compared to C15S STIM2 15-217, it is likely that the loss of the Cys15 modifiable sulfhydryl prevents the interaction of this residue with the EFSAM core, mediating a relatively decreased thermodynamic stability enhancement of the single mutant protein. **(C)** On the other hand, STIM2 15-217 protein with only the unique Cys15 sulfhydryl available for *S*-nitrosylation (i.e. C53S/C60S double mutant protein) appeared thermodynamically insensitive to excess NO, suggesting that these changes mediated by Cys15 are dependent on the interaction of Cys53 and Cys60 with the EFSAM core. **(D)** When all modifiable Cys sulfhydrls were mutated (*i.e.* C15S/C53/C60S triple mutant protein), excess NO did not affect thermodynamic stability, suggesting that the NO mediated structural perturbations which enhance STIM2 luminal domain stability are Cys-specific. Note that structurally unresolved and intrinsically disordered variable N-terminal region (i.e. residues 15-66) is included for visualization purposes, and is represented by a dashed structure.

4.5. Implications of excess NO mediated STIM2 functional suppression in health and disease

Given that the NO donor, GSNO, enhanced the thermodynamic stability of wildtype STIM2 15-217, I anticipated that GSNO treatment of mammalian cells overexpressing full length STIM2 and Orai1 would attenuate basal Ca^{2+} levels and SOCE. As expected, cells co-overexpressing full length STIM2 and Orai1 showed enhanced basal, ER stored Ca^{2+} and SOCE compared to cells expressing Orai1 and mCh in the absence of STIM2. Treating the STIM2/Orai1 co-overexpressing cells with GSNO reduced the basal Ca^{2+} levels, TG-induced ER Ca^{2+} release and maximal Ca^{2+} uptake after extracellular Ca^{2+} addback (*i.e.* SOCE) back to levels observed in the cells without STIM2 expression (Fig. 3.8.1 and 3.8.2). Surprisingly, co-overexpressing Cys15Ser/Cys53Ser/Cys60Ser STIM2 with Orai1 did not enhance resting or stimulated Ca^{2+} levels, despite the luminal domain destabilization caused by this triple mutation. To my knowledge, this is the first example of a variation in either STIM2 or STIM1 that caused a decreased luminal domain stability without promoting SOCE (Gui et al., 2018; Stathopulos et al., 2008a; Zheng et al., 2008; Zhu et al., 2018). Given that the Cys15 is located immediately adjacent to the ER signal peptide of STIM2, it is possible that the Cys15Ser variation prevented or perturbed the ER localization of STIM2. Interestingly, past studies have found that a fraction of wild-type STIM2 escapes ER targeting and accumulates in the cytosol (Graham et al., 2011). Thus, the Cys15Ser mutations may alter the ER versus cytosolic accumulation levels.

STIM2 functions not only to elicit agonist-induced SOCE, but also acts as a basal Ca^{2+} homeostatic feedback regulator (Brandman et al., 2007). Therefore, alternations to STIM2 function in cells have the potential to play roles in diseases with dysregulated Ca^{2+} homeostasis. While there are currently no identified pathologies caused by single mutations to human *STIM2* alleles, upregulated and hyperactivated STIM2 has been linked to numerous pathological conditions, especially within the nervous system. Mice models established that in the presence of STIM2, neuronal damage under transient anoxic conditions is amplified (Berna-Erro et al., 2009). Moreover, mouse neurons deficient in STIM2, but not STIM1, demonstrated an enhanced resistance to Ca^{2+} dependent apoptosis induced by anoxic conditions, possibly by preventing cytosolic Ca^{2+} overload (Berna-Erro et al., 2009). Similarly, traumatic brain injury upregulated STIM2 expression in mice neurons, and selective knockdown of STIM2, but not STIM1, improved neuronal survival after this pathology (Rao et al., 2015), likely due to restoring Ca^{2+} homeostasis within these neurons. In medium spiny neurons (MSN) isolated from mouse models of Huntington's disease (*i.e.* YAC128 MSNs), hyperactive STIM2 mediates sustained and cytotoxic SOCE (Wu et al., 2016). Knockout of STIM2 rescued spine loss in YAC128 MSNs by restoring dysregulated Ca^{2+} homeostasis (Wu et al., 2016).

Within the vascular system, STIM2 expression was shown to be upregulated in pulmonary arterial smooth muscle cells (PASMCs) from patients with pulmonary arterial hypertension (PAH) (Song et al., 2011). STIM2, together with Orai2, increases cytosolic Ca^{2+} levels which triggers the transition of contractile PASMCs to the proliferative phenotype, thus contributing to PAH (Fernandez et al., 2015). The pathological molecular mechanism was later discovered, whereby upregulated STIM2 in PAH-PASMCs elevates basal Ca^{2+} levels to activate the CREB, STAT3, AKT, NFAT and Bcl-2 signalling pathways, which ultimately stimulate proliferation and inhibit apoptosis (Song et al., 2018). It is possible that excess NO-mediated STIM2 inhibition could ameliorate these conditions with hyperactive or upregulated STIM2, and that endogenous NO production could act as a protective mechanism by maintaining STIM2 in a quiescent state through *S*-nitrosylation mediated stabilization of the luminal domain.

4.6. Future directions and limitations

In my current study, I revealed the structural mechanism by which the excess NO donor, GSNO, thermally and thermodynamically stabilized the full luminal domain of STIM2, which suppressed function in the full-length molecular context. Furthermore, compared to STIM1, I revealed an additional modifiable Cys residue within the variable N-terminal region of STIM2, which supplements the enhanced stabilization mediated by the Cys residues conserved with STIM1 in the presence of excess NO. While my NMR data identified regions within the EFSAM core that were structurally perturbed in the presence of excess NO, solving the 3D structure of the EFSAM core in the modified state(s) would reveal precisely how the tertiary structure and fold of EFSAM changes in response to this modification. Nevertheless, *S*-nitrosylation is an exceptionally labile modification, making these studies difficult. Upon ER Ca^{2+} depletion, STIM2 co-localizes with Orai1 in ER-PM junctions to mediate SOCE. Therefore, cell microscopy studies clarifying whether GSNO treatment disrupts this STIM2:Orai1 co-localization in mammalian cells would complement my Ca^{2+} assessments and reveal whether the Cys mutations alter the localization of

STIM2. Previous studies indicate that STIM proteins are able to undergo a plethora of post-translational modifications that can either activate or inactivate the molecule. Understanding the precise biological environments which promotes specific post-translational modifications that affect STIM function would further refine our understanding on how STIM proteins are regulated. The work described in this thesis represents the first study to my knowledge that reports the effects of GSNO treatment on STIM2 function. However, my work focuses only on mechanism in the physiological context. Because upregulated and hyperactive STIM2 underlie the pathogenesis of multiple diseases (see above), investigating whether NO can affect these conditions *in vitro* and/or *in vivo* would greatly enhance our understanding of these diseases in the pathological context and potentially reveal new treatment avenues.

There are some notable limitations within this present study. First, during expression and purification procedures, human proteins expressed in bacteria were denatured and subsequently refolded outside their native environment; thus, the proteins may not have adopted a true native state. Second, my *in vitro* biophysical characterization studies used isolated STIM2 protein fragments, which does not fully recapitulate the ER-tethered environment of most STIM2 molecules. Third, all experiments were performed using and maintaining high levels of the NO donor, GSNO, due to the labile nature of protein *S*-nitrosylation, which limited the types of investigations that could be conducted. Specifically, Ca^{2+} binding affinity via CD spectroscopy was not assessed due to the marked increase in high tension associated with GSNO-containing buffers. Moreover, direct mass spectrometry measurements to unequivocally detect the protein *S*-nitrosylation was not possible. Fourth, my full-length STIM2 protein harbouring the Cys mutations could not be used to confirm the Cys-dependence of the NO-mediated suppression of basal and stimulated cytosolic Ca^{2+} due to the inability of the triple mutant to enhance SOCE and the wildly variable responses observed with the single Cys15Ser mutant.

4.7. Conclusions

Calcium signalling is ubiquitous and involved in a wide range of physiological processes such as apoptosis, muscle contraction and gene transcription. In order to tightly regulate these processes, Ca^{2+} is effectively segregated in intracellular stores, most notably within the ER. STIM2 is an ER resident Ca^{2+} sensing protein which, together with the PM Orai1-composed Ca^{2+} channels, responds to ER Ca^{2+} levels in order to regulate cytosolic Ca^{2+}. Under ER Ca^{2+} store replete conditions STIM2 regulates basal Ca^{2+} levels. Upon ER Ca^{2+} store depletion due to a cellular stimulus, STIM2 mediates SOCE. Hence, modifications influencing STIM2 activity can influence both resting and stimulated Ca^{2+} levels within cells.

Post-translational modifications profoundly impact protein structure and function, which underlie important biological roles, such as cellular trafficking, signalling cascades, and protein activation and localization. Perhaps the most commonly studied post-translational modification is protein phosphorylation; however, until recently, few studies have examined the role of *S*-nitrosylation, which is the covalent attachment of a NO moiety to a sulfhydryl. Recently, *S*-nitrosylation has been demonstrated to reduce the activity of STIM1, but knowledge on how this modification may affect STIM2 function was completely lacking.

Therefore, this thesis investigated the biophysical, structural and functional consequences that *S*-nitrosylation has on the Ca^{2+} sensing luminal domain of STIM2 to enhance our understanding of Orai1 Ca^{2+} channel regulation. Biophysically, my data reveal that excess NO donor stabilizes the full luminal domain of STIM2 in a Cys-specific manner, whereby a unique Cys residue present in the Ca^{2+} sensing region of STIM2 but not STIM1, is involved in the stabilization. Structurally, the presence of excess NO induces changes to the full luminal domain of STIM2 which were predominantly localized to one face of the EFSAM core. Functionally, GSNO treatment of mammalian cells co-overexpressing wildtype mChSTIM2 and eGFP-Orai1 attenuated basal Ca^{2+} levels, decreased ER stored Ca^{2+} levels as well as SOCE (Fig. 4.2).

In conclusion, my thesis not only advances our biophysical, structural, and functional knowledge of the effects excess NO has on STIM2-mediated Ca^{2+} flux (Table 4.1), but also brings us to the forefront of the field with new and important questions that must be answered in order to fully understand STIM2 function and the role of *S*-nitrosylation in regulating its structure and function in health and disease. NO has long been known to confer physiological benefits, including stimulation of oxygen and blood flow, reduction of blood pressure, and boosted endurance; however, my research demonstrates a novel mechanism by which NO can regulate STIM2-mediated Ca^{2+} homeostasis.

Table 4.1. Summary of GSNO mediated effects on various properties associated with STIM2

	Reducing conditions (1 mM DTT; -S-H)[a]	***S*-nitrosylating conditions (1 mM GSNO; -S-N=O)**[a]
Thermal stability [b]	↓	↑
Oligomerization [b]	**-**	**-**
Exposed hydrophobicity [b]	**-**	**-**
Thermodynamic stability [b]	↓	↑
Basal Ca^{2+} levels [c]	↑	↓
SOCE activation [c]	↑	↓

(↓) Relatively lower, **(↑)** Relatively higher, **(-)** No apparent change

[a] properties of 1 mM DTT treatment compared to 1 mM GSNO treatment

[b] experiments using recombinant human STIM2 15-217 protein

[c] experiments using HEK293T cells co-overexpressing mChSTIM2 variants and eGFP-Orai1

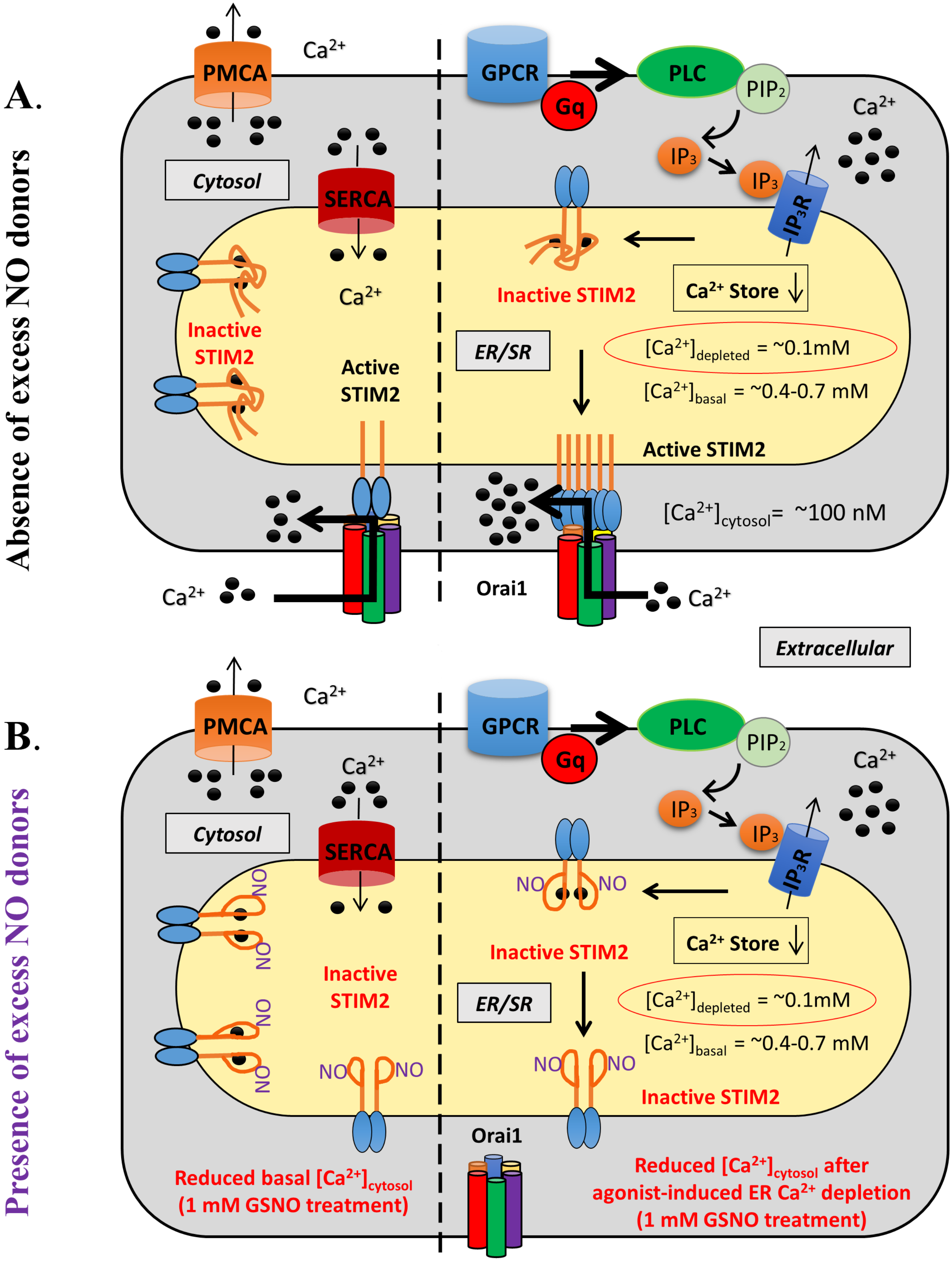

Fig. 4.2. Proposed model of excess NO mediated suppression of STIM2 function. (A) Normally, a small subset of STIM2 is in an active state, gating Orai1 channels to mediate an increase in basal calcium levels. STIMs become activated to mediate SOCE after agonist-induced ER store Ca^{2+} depletion. (**B**) Under resting conditions and in the presence of excess NO, the small subset of STIM2 normally active is inhibited which prevents elevations in basal Ca^{2+} levels. After agonist induced ER Ca^{2+} store depletion and in the presence of excess NO, STIM2 is inhibited which attenuates SOCE.

References:

1. Anand, P., and Stamler, J.S. (2012). Enzymatic mechanisms regulating protein S-nitrosylation: implications in health and disease. *J Mol Med (Berl).* 90 (3), 233-244.

2. Arnelle, D.R., and Stamler, J.S. (1995). NO+, NO, and NO- donation by S-nitrosothiols: implications for regulation of physiological functions by S-nitrosylation and acceleration of disulfide formation. *Arch Biochem Biophys.* 318 (2), 279-285.

3. Baba, Y., Hayashi, K., Fujii, Y., Mizushima, A., Watarai, H., Wakamori, M., Numaga, T., Mori, Y., Iino, M., Hikida, M., and Kurosaki, T. (2006). Coupling of STIM1 to store-operated Ca2+ entry through its constitutive and inducible movement in the endoplasmic reticulum. *Proc Natl Acad Sci U S A.* 103 (45), 16704-16709.

4. Barnett, S.D., and Buxton, I.L.O. (2017). The role of S-nitrosoglutathione reductase (GSNOR) in human disease and therapy. *Crit Rev Biochem Mol Biol.* 52 (3), 340-354.

5. Barr, V.A., Bernot, K.M., Shaffer, M.H., Burkhardt, J.K., and Samelson, L.E. (2009). Formation of STIM and Orai complexes: puncta and distal caps. *Immunol Rev.* 231 (1), 148-159.

6. Bauer, M.C., O'Connell, D., Cahill, D.J., and Linse, S. (2008). Calmodulin binding to the polybasic C-termini of STIM proteins involved in store-operated calcium entry. *Biochemistry.* 47 (23), 6089-6091.

7. Benhar, M., Forrester, M.T., and Stamler, J.S. (2006). Nitrosative stress in the ER: a new role for S-nitrosylation in neurodegenerative diseases. *ACS Chem Biol.* 1 (6), 355-358.

8. Berna-Erro, A., Braun, A., Kraft, R., Kleinschnitz, C., Schuhmann, M.K., Stegner, D., Wultsch, T., Eilers, J., Meuth, S.G., Stoll, G., and Nieswandt, B. (2009). STIM2 regulates capacitive Ca2+ entry in neurons and plays a key role in hypoxic neuronal cell death. *Sci Signal.* 2 (93), ra67.

9. Berridge, M.J., Bootman, M.D., and Roderick, H.L. (2003). Calcium signalling: dynamics, homeostasis and remodelling. *Nat Rev Mol Cell Biol.* 4 (7), 517-529.

10. Betz, S.F. (1993). Disulfide bonds and the stability of globular proteins. *Protein Sci.* 2 (10), 1551-1558.

11. Bhardwaj, R., Muller, H.M., Nickel, W., and Seedorf, M. (2013). Oligomerization and Ca2+/calmodulin control binding of the ER Ca2+-sensors STIM1 and STIM2 to plasma membrane lipids. *Biosci Rep.* 33 (5).

12. Bocedi, A., Gradoni, L., Menegatti, E., and Ascenzi, P. (2004). Kinetics of parasite cysteine proteinase inactivation by NO-donors. *Biochem Biophys Res Commun.* 315 (3), 710-718.

13. Boyman, L., Williams, G.S., Khananshvili, D., Sekler, I., and Lederer, W.J. (2013). NCLX: the mitochondrial sodium calcium exchanger. *J Mol Cell Cardiol.* 59, 205-213.

14. Brandman, O., Liou, J., Park, W.S., and Meyer, T. (2007). STIM2 is a feedback regulator that stabilizes basal cytosolic and endoplasmic reticulum Ca2+ levels. *Cell.* 131 (7), 1327-1339.

15. Braun, A., Gessner, J.E., Varga-Szabo, D., Syed, S.N., Konrad, S., Stegner, D., Vogtle, T., Schmidt, R.E., and Nieswandt, B. (2009). STIM1 is essential for Fcgamma receptor activation and autoimmune inflammation. *Blood.* 113 (5), 1097-1104.

16. Broniowska, K.A., and Hogg, N. (2012). The chemical biology of S-nitrosothiols. *Antioxid Redox Signal.* 17 (7), 969-980.

17. Bueno, O.F., Brandt, E.B., Rothenberg, M.E., and Molkentin, J.D. (2002). Defective T cell development and function in calcineurin A beta -deficient mice. *Proc Natl Acad Sci U S A.* 99 (14), 9398-9403.

18. Burette, A., and Weinberg, R.J. (2007). Perisynaptic organization of plasma membrane calcium pumps in cerebellar cortex. *J Comp Neurol.* 500 (6), 1127-1135.

19. Burger, D.E., Lu, X., Lei, M., Xiang, F.L., Hammoud, L., Jiang, M., Wang, H., Jones, D.L., Sims, S.M., and Feng, Q. (2009). Neuronal nitric oxide synthase protects against myocardial infarction-induced ventricular arrhythmia and mortality in mice. *Circulation.* 120 (14), 1345-1354.

20. Cahalan, M.D., and Chandy, K.G. (2009). The functional network of ion channels in T lymphocytes. *Immunol Rev.* 231 (1), 59-87.

21. Cai, X. (2007). Molecular evolution and functional divergence of the Ca(2+) sensor protein in store-operated Ca(2+) entry: stromal interaction molecule. *PLoS One.* 2 (7), e609.

22. Cai, X., Zhou, Y., Nwokonko, R.M., Loktionova, N.A., Wang, X., Xin, P., Trebak, M., Wang, Y., and Gill, D.L. (2016). The Orai1 Store-operated Calcium Channel Functions as a Hexamer. *J Biol Chem.* 291 (50), 25764-25775.

23. Calloway, N., Owens, T., Corwith, K., Rodgers, W., Holowka, D., and Baird, B. (2011). Stimulated association of STIM1 and Orai1 is regulated by the balance of PtdIns(4,5)P(2) between distinct membrane pools. *J Cell Sci.* 124 (Pt 15), 2602-2610.

24. Cheng, H., Lederer, W.J., and Cannell, M.B. (1993). Calcium sparks: elementary events underlying excitation-contraction coupling in heart muscle. *Science.* 262 (5134), 740-744.

25. Choi, Y.J., Zhao, Y., Bhattacharya, M., and Stathopulos, P.B. (2017a). Structural perturbations induced by Asn131 and Asn171 glycosylation converge within the EFSAM

core and enhance stromal interaction molecule-1 mediated store operated calcium entry. *Biochim Biophys Acta.* 1864 (6), 1054-1063.

26. Choi, Y.J., Zhao, Y., Bhattacharya, M., and Stathopulos, P.B. (2017b). Structural perturbations induced by Asn131 and Asn171 glycosylation converge within the EFSAM core and enhance stromal interaction molecule-1 mediated store operated calcium entry. *Biochim Biophys Acta Mol Cell Res.* 1864 (6), 1054-1063.

27. Choi, Y.J., Zhu, J., Chung, S., Siddiqui, N., Feng, Q., and Stathopulos, P.B. (2017c). Targeting Cysteine Thiols for in Vitro Site-specific Glycosylation of Recombinant Proteins. *J Vis Exp.*(128).

28. Chung, S., Zhang, M., and Stathopulos, P.B. (2018). The 2beta Splice Variation Alters the Structure and Function of the Stromal Interaction Molecule Coiled-Coil Domains. *Int J Mol Sci.* 19 (11).

29. Csutora, P., Peter, K., Kilic, H., Park, K.M., Zarayskiy, V., Gwozdz, T., and Bolotina, V.M. (2008). Novel role for STIM1 as a trigger for calcium influx factor production. *J Biol Chem.* 283 (21), 14524-14531.

30. Cui, B., Yang, X., Li, S., Lin, Z., Wang, Z., Dong, C., and Shen, Y. (2013). The inhibitory helix controls the intramolecular conformational switching of the C-terminus of STIM1. *PLoS One.* 8 (9), e74735.

31. Czyz, A., Brutkowski, W., Fronk, J., Duszynski, J., and Zablocki, K. (2009). Tunicamycin desensitizes store-operated Ca2+ entry to ATP and mitochondrial potential. *Biochem Biophys Res Commun.* 381 (2), 176-180.

32. Dalle-Donne, I., Rossi, R., Colombo, G., Giustarini, D., and Milzani, A. (2009). Protein S-glutathionylation: a regulatory device from bacteria to humans. *Trends Biochem Sci.* 34 (2), 85-96.

33. Davis, F.M., Goulding, E.H., D'Agostin, D.M., Janardhan, K.S., Cummings, C.A., Bird, G.S., Eddy, E.M., and Putney, J.W. (2016). Male infertility in mice lacking the store-operated Ca(2+) channel Orai1. *Cell Calcium.* 59 (4), 189-197.

34. Davlouros, P.A., Gkizas, V., Vogiatzi, C., Giannopoulos, G., Alexopoulos, D., and Deftereos, S. (2016). Calcium Homeostasis and Kinetics in Heart Failure. *Med Chem.* 12 (2), 151-161.

35. DeHaven, W.I., Smyth, J.T., Boyles, R.R., and Putney, J.W., Jr. (2007). Calcium inhibition and calcium potentiation of Orai1, Orai2, and Orai3 calcium release-activated calcium channels. *J Biol Chem.* 282 (24), 17548-17556.

36. Dejanovic, B., and Schwarz, G. (2014). Neuronal nitric oxide synthase-dependent S-nitrosylation of gephyrin regulates gephyrin clustering at GABAergic synapses. *J Neurosci.* 34 (23), 7763-7768.

37. Derler, I., Fahrner, M., Muik, M., Lackner, B., Schindl, R., Groschner, K., and Romanin, C. (2009). A Ca2(+)release-activated Ca2(+) (CRAC) modulatory domain (CMD) within STIM1 mediates fast Ca2(+)-dependent inactivation of ORAI1 channels. *J Biol Chem.* 284 (37), 24933-24938.

38. DiPolo, R., and Beauge, L. (2006). Sodium/calcium exchanger: influence of metabolic regulation on ion carrier interactions. *Physiol Rev.* 86 (1), 155-203.

39. Drexler, H., Kastner, S., Strobel, A., Studer, R., Brodde, O.E., and Hasenfuss, G. (1998). Expression, activity and functional significance of inducible nitric oxide synthase in the failing human heart. *J Am Coll Cardiol.* 32 (4), 955-963.

40. Ebashi, S., and Endo, M. (1968). Calcium ion and muscle contraction. *Prog Biophys Mol Biol.* 18, 123-183.

41. Eichmann, C., Tzitzilonis, C., Nakamura, T., Kwiatkowski, W., Maslennikov, I., Choe, S., Lipton, S.A., and Riek, R. (2016). S-Nitrosylation Induces Structural and Dynamical Changes in a Rhodanese Family Protein. *J Mol Biol.* 428 (19), 3737-3751.

42. Emrich, S.M., Yoast, R.E., Xin, P., Zhang, X., Pathak, T., Nwokonko, R., Gueguinou, M.F., Subedi, K.P., Zhou, Y., Ambudkar, I.S., Hempel, N., Machaca, K., Gill, D.L., and Trebak, M. (2019). Cross-talk between N-terminal and C-terminal domains in stromal interaction molecule 2 (STIM2) determines enhanced STIM2 sensitivity. *J Biol Chem.* 294 (16), 6318-6332.

43. Enomoto, M., Nishikawa, T., Siddiqui, N., Chung, S., Ikura, M., and Stathopulos, P.B. (2017). From Stores to Sinks: Structural Mechanisms of Cytosolic Calcium Regulation. *Adv Exp Med Biol.* 981, 215-251.

44. Erickson, J.R., Nichols, C.B., Uchinoumi, H., Stein, M.L., Bossuyt, J., and Bers, D.M. (2015). S-Nitrosylation Induces Both Autonomous Activation and Inhibition of Calcium/Calmodulin-dependent Protein Kinase II delta. *J Biol Chem.* 290 (42), 25646-25656.

45. Fahrner, M., Muik, M., Schindl, R., Butorac, C., Stathopulos, P., Zheng, L., Jardin, I., Ikura, M., and Romanin, C. (2014). A coiled-coil clamp controls both conformation and clustering of stromal interaction molecule 1 (STIM1). *J Biol Chem.* 289 (48), 33231-33244.

46. Feng, J.H., Jing, F.B., Fang, H., Gu, L.C., and Xu, W.F. (2011). Expression, purification, and S-nitrosylation of recombinant histone deacetylase 8 in Escherichia coli. *Biosci Trends.* 5 (1), 17-22.

47. Feng, Q., Fortin, A.J., Lu, X., and Arnold, J.M. (1999). Effects of L-arginine on endothelial and cardiac function in rats with heart failure. *Eur J Pharmacol.* 376 (1-2), 37-44.

48. Feng, Q., Lu, X., Jones, D.L., Shen, J., and Arnold, J.M. (2001). Increased inducible nitric oxide synthase expression contributes to myocardial dysfunction and higher mortality after myocardial infarction in mice. *Circulation.* 104 (6), 700-704.

49. Feng, Q., Song, W., Lu, X., Hamilton, J.A., Lei, M., Peng, T., and Yee, S.P. (2002). Development of heart failure and congenital septal defects in mice lacking endothelial nitric oxide synthase. *Circulation.* 106 (7), 873-879.

50. Fernandez, R.A., Wan, J., Song, S., Smith, K.A., Gu, Y., Tauseef, M., Tang, H., Makino, A., Mehta, D., and Yuan, J.X. (2015). Upregulated expression of STIM2, TRPC6, and Orai2 contributes to the transition of pulmonary arterial smooth muscle cells from a contractile to proliferative phenotype. *Am J Physiol Cell Physiol.* 308 (8), C581-593.

51. Feske, S., Gwack, Y., Prakriya, M., Srikanth, S., Puppel, S.H., Tanasa, B., Hogan, P.G., Lewis, R.S., Daly, M., and Rao, A. (2006). A mutation in Orai1 causes immune deficiency by abrogating CRAC channel function. *Nature.* 441 (7090), 179-185.

52. Frischauf, I., Muik, M., Derler, I., Bergsmann, J., Fahrner, M., Schindl, R., Groschner, K., and Romanin, C. (2009). Molecular determinants of the coupling between STIM1 and Orai channels: differential activation of Orai1-3 channels by a STIM1 coiled-coil mutant. *J Biol Chem.* 284 (32), 21696-21706.

53. Gallogly, M.M., and Mieyal, J.J. (2007). Mechanisms of reversible protein glutathionylation in redox signaling and oxidative stress. *Curr Opin Pharmacol.* 7 (4), 381-391.

54. Garcia-Sainz, J.A., Romero-Avila, M.T., and Medina Ldel, C. (2010). alpha(1D)-Adrenergic receptors constitutive activity and reduced expression at the plasma membrane. *Methods Enzymol.* 484, 109-125.

55. Ghosh, A., and Greenberg, M.E. (1995). Calcium signaling in neurons: molecular mechanisms and cellular consequences. *Science.* 268 (5208), 239-247.

56. Gonzalez, D.R., Beigi, F., Treuer, A.V., and Hare, J.M. (2007). Deficient ryanodine receptor S-nitrosylation increases sarcoplasmic reticulum calcium leak and arrhythmogenesis in cardiomyocytes. *Proc Natl Acad Sci U S A.* 104 (51), 20612-20617.

57. Gould, N., Doulias, P.T., Tenopoulou, M., Raju, K., and Ischiropoulos, H. (2013). Regulation of protein function and signaling by reversible cysteine S-nitrosylation. *J Biol Chem.* 288 (37), 26473-26479.

58. Graham, S.J., Dziadek, M.A., and Johnstone, L.S. (2011). A cytosolic STIM2 preprotein created by signal peptide inefficiency activates ORAI1 in a store-independent manner. *J Biol Chem.* 286 (18), 16174-16185.

59. Grynkiewicz, G., Poenie, M., and Tsien, R.Y. (1985). A new generation of Ca2+ indicators with greatly improved fluorescence properties. *J Biol Chem.* 260 (6), 3440-3450.

60. Gudlur, A., Zeraik, A.E., Hirve, N., Rajanikanth, V., Bobkov, A.A., Ma, G., Zheng, S., Wang, Y., Zhou, Y., Komives, E.A., and Hogan, P.G. (2018). Calcium sensing by the STIM1 ER-luminal domain. *Nat Commun.* 9 (1), 4536.

61. Gui, L., Zhu, J., Lu, X., Sims, S.M., Lu, W.Y., Stathopulos, P.B., and Feng, Q. (2018). S-Nitrosylation of STIM1 by Neuronal Nitric Oxide Synthase Inhibits Store-Operated Ca(2+) Entry. *J Mol Biol.* 430 (12), 1773-1785.

62. Hao, G., Xie, L., and Gross, S.S. (2004). Argininosuccinate synthetase is reversibly inactivated by S-nitrosylation in vitro and in vivo. *J Biol Chem.* 279 (35), 36192-36200.

63. Hawkins, B.J., Irrinki, K.M., Mallilankaraman, K., Lien, Y.C., Wang, Y., Bhanumathy, C.D., Subbiah, R., Ritchie, M.F., Soboloff, J., Baba, Y., Kurosaki, T., Joseph, S.K., Gill, D.L., and Madesh, M. (2010). S-glutathionylation activates STIM1 and alters mitochondrial homeostasis. *J Cell Biol.* 190 (3), 391-405.

64. Hoth, M., and Niemeyer, B.A. (2013). The neglected CRAC proteins: Orai2, Orai3, and STIM2. *Curr Top Membr.* 71, 237-271.

65. Hou, X., Pedi, L., Diver, M.M., and Long, S.B. (2012). Crystal structure of the calcium release-activated calcium channel Orai. *Science.* 338 (6112), 1308-1313.

66. Hu, J., Qin, K., Zhang, Y., Gong, J., Li, N., Lv, D., Xiang, R., and Tan, X. (2011). Downregulation of transcription factor Oct4 induces an epithelial-to-mesenchymal transition via enhancement of Ca2+ influx in breast cancer cells. *Biochem Biophys Res Commun.* 411 (4), 786-791.

67. Hunter, T. (1995). Protein kinases and phosphatases: the yin and yang of protein phosphorylation and signaling. *Cell.* 80 (2), 225-236.

68. Hunton, D.L., Lucchesi, P.A., Pang, Y., Cheng, X., Dell'Italia, L.J., and Marchase, R.B. (2002). Capacitative calcium entry contributes to nuclear factor of activated T-cells nuclear translocation and hypertrophy in cardiomyocytes. *J Biol Chem.* 277 (16), 14266-14273.

69. Ikura, M. (1996). Calcium binding and conformational response in EF-hand proteins. *Trends Biochem Sci.* 21 (1), 14-17.

70. Irie, T., Sips, P.Y., Kai, S., Kida, K., Ikeda, K., Hirai, S., Moazzami, K., Jiramongkolchai, P., Bloch, D.B., Doulias, P.T., Armoundas, A.A., Kaneki, M., Ischiropoulos, H., Kranias, E., Bloch, K.D., Stamler, J.S., and Ichinose, F. (2015). S-Nitrosylation of Calcium-Handling Proteins in Cardiac Adrenergic Signaling and Hypertrophy. *Circ Res.* 117 (9), 793-803.

71. Jardin, I., Dionisio, N., Frischauf, I., Berna-Erro, A., Woodard, G.E., Lopez, J.J., Salido, G.M., and Rosado, J.A. (2013). The polybasic lysine-rich domain of plasma membrane-resident STIM1 is essential for the modulation of store-operated divalent cation entry by extracellular calcium. *Cell Signal.* 25 (5), 1328-1337.

72. Kahler, J., Ewert, A., Weckmuller, J., Stobbe, S., Mittmann, C., Koster, R., Paul, M., Meinertz, T., and Munzel, T. (2001). Oxidative stress increases endothelin-1 synthesis in human coronary artery smooth muscle cells. *J Cardiovasc Pharmacol.* 38 (1), 49-57.

73. Kahler, J., Mendel, S., Weckmuller, J., Orzechowski, H.D., Mittmann, C., Koster, R., Paul, M., Meinertz, T., and Munzel, T. (2000). Oxidative stress increases synthesis of big endothelin-1 by activation of the endothelin-1 promoter. *J Mol Cell Cardiol.* 32 (8), 1429-1437.

74. Kawasaki, T., Lange, I., and Feske, S. (2009). A minimal regulatory domain in the C terminus of STIM1 binds to and activates ORAI1 CRAC channels. *Biochem Biophys Res Commun.* 385 (1), 49-54.

75. Kikkawa, U., Minakuchi, R., Takai, Y., and Nishizuka, Y. (1983). Calcium-activated, phospholipid-dependent protein kinase (protein kinase C) from rat brain. *Methods Enzymol.* 99, 288-298.

76. Kilch, T., Alansary, D., Peglow, M., Dorr, K., Rychkov, G., Rieger, H., Peinelt, C., and Niemeyer, B.A. (2013). Mutations of the Ca2+-sensing stromal interaction molecule STIM1 regulate Ca2+ influx by altered oligomerization of STIM1 and by destabilization of the Ca2+ channel Orai1. *J Biol Chem.* 288 (3), 1653-1664.

77. Lasorsa, F.M., Pinton, P., Palmieri, L., Scarcia, P., Rottensteiner, H., Rizzuto, R., and Palmieri, F. (2008). Peroxisomes as novel players in cell calcium homeostasis. *J Biol Chem.* 283 (22), 15300-15308.

78. Lin, Q.T., and Stathopulos, P.B. (2019). Molecular Mechanisms of Leucine Zipper EF-Hand Containing Transmembrane Protein-1 Function in Health and Disease. *Int J Mol Sci.* 20 (2).

79. Liou, J., Fivaz, M., Inoue, T., and Meyer, T. (2007). Live-cell imaging reveals sequential oligomerization and local plasma membrane targeting of stromal interaction molecule 1 after Ca2+ store depletion. *Proc Natl Acad Sci U S A.* 104 (22), 9301-9306.

80. Liou, J., Kim, M.L., Heo, W.D., Jones, J.T., Myers, J.W., Ferrell, J.E., Jr., and Meyer, T. (2005). STIM is a Ca2+ sensor essential for Ca2+-store-depletion-triggered Ca2+ influx. *Curr Biol.* 15 (13), 1235-1241.

81. Lis, A., Peinelt, C., Beck, A., Parvez, S., Monteilh-Zoller, M., Fleig, A., and Penner, R. (2007). CRACM1, CRACM2, and CRACM3 are store-operated Ca2+ channels with distinct functional properties. *Curr Biol.* 17 (9), 794-800.

82. Liu, L., Enright, E., Sun, P., Tsai, S.Y., Mehta, P., Beckman, D.L., and Terrian, D.M. (2002). Inactivation of annexin II tetramer by S-nitrosoglutathione. *Eur J Biochem.* 269 (17), 4277-4286.

83. Liu, Y., Zheng, X., Mueller, G.A., Sobhany, M., DeRose, E.F., Zhang, Y., London, R.E., and Birnbaumer, L. (2012). Crystal structure of calmodulin binding domain of orai1 in complex with Ca2+ calmodulin displays a unique binding mode. *J Biol Chem.* 287 (51), 43030-43041.

84. Lopez, E., Jardin, I., Berna-Erro, A., Bermejo, N., Salido, G.M., Sage, S.O., Rosado, J.A., and Redondo, P.C. (2012a). STIM1 tyrosine-phosphorylation is required for STIM1-Orai1 association in human platelets. *Cell Signal.* 24 (6), 1315-1322.

85. Lopez, E., Salido, G.M., Rosado, J.A., and Berna-Erro, A. (2012b). Unraveling STIM2 function. *J Physiol Biochem.* 68 (4), 619-633.

86. Lopez, J.J., Salido, G.M., Pariente, J.A., and Rosado, J.A. (2006). Interaction of STIM1 with endogenously expressed human canonical TRP1 upon depletion of intracellular Ca2+ stores. *J Biol Chem.* 281 (38), 28254-28264.

87. Luik, R.M., Wu, M.M., Buchanan, J., and Lewis, R.S. (2006). The elementary unit of store-operated Ca2+ entry: local activation of CRAC channels by STIM1 at ER-plasma membrane junctions. *J Cell Biol.* 174 (6), 815-825.

88. Luo, X., Hojayev, B., Jiang, N., Wang, Z.V., Tandan, S., Rakalin, A., Rothermel, B.A., Gillette, T.G., and Hill, J.A. (2012). STIM1-dependent store-operated Ca(2)(+) entry is required for pathological cardiac hypertrophy. *J Mol Cell Cardiol.* 52 (1), 136-147.

89. Ma, J., McCarl, C.A., Khalil, S., Luthy, K., and Feske, S. (2010). T-cell-specific deletion of STIM1 and STIM2 protects mice from EAE by impairing the effector functions of Th1 and Th17 cells. *Eur J Immunol.* 40 (11), 3028-3042.

90. Macian, F. (2005). NFAT proteins: key regulators of T-cell development and function. *Nat Rev Immunol.* 5 (6), 472-484.

91. Madej, E., Folkes, L.K., Wardman, P., Czapski, G., and Goldstein, S. (2008). Thiyl radicals react with nitric oxide to form S-nitrosothiols with rate constants near the diffusion-controlled limit. *Free Radic Biol Med.* 44 (12), 2013-2018.

92. Manji, S.S., Parker, N.J., Williams, R.T., van Stekelenburg, L., Pearson, R.B., Dziadek, M., and Smith, P.J. (2000). STIM1: a novel phosphoprotein located at the cell surface. *Biochim Biophys Acta.* 1481 (1), 147-155.

93. Matsumoto, M., Fujii, Y., Baba, A., Hikida, M., Kurosaki, T., and Baba, Y. (2011). The calcium sensors STIM1 and STIM2 control B cell regulatory function through interleukin-10 production. *Immunity.* 34 (5), 703-714.

94. Mattson, M.P. (2007). Calcium and neurodegeneration. *Aging Cell.* 6 (3), 337-350.

95. Mattson, M.P., and Chan, S.L. (2003). Calcium orchestrates apoptosis. *Nat Cell Biol.* 5 (12), 1041-1043.

96. Maus, M., Jairaman, A., Stathopulos, P.B., Muik, M., Fahrner, M., Weidinger, C., Benson, M., Fuchs, S., Ehl, S., Romanin, C., Ikura, M., Prakriya, M., and Feske, S. (2015). Missense mutation in immunodeficient patients shows the multifunctional roles of coiled-coil domain 3 (CC3) in STIM1 activation. *Proc Natl Acad Sci U S A.* 112 (19), 6206-6211.

97. McGuffin, L.J., Bryson, K., and Jones, D.T. (2000). The PSIPRED protein structure prediction server. *Bioinformatics.* 16 (4), 404-405.

98. Miederer, A.M., Alansary, D., Schwar, G., Lee, P.H., Jung, M., Helms, V., and Niemeyer, B.A. (2015). A STIM2 splice variant negatively regulates store-operated calcium entry. *Nat Commun.* 6, 6899.

99. Mignen, O., Thompson, J.L., and Shuttleworth, T.J. (2007). STIM1 regulates Ca2+ entry via arachidonate-regulated Ca2+-selective (ARC) channels without store depletion or translocation to the plasma membrane. *J Physiol.* 579 (Pt 3), 703-715.

100. Mikoshiba, K. (2007). The IP3 receptor/Ca2+ channel and its cellular function. *Biochem Soc Symp.*(74), 9-22.

101. Misceo, D., Holmgren, A., Louch, W.E., Holme, P.A., Mizobuchi, M., Morales, R.J., De Paula, A.M., Stray-Pedersen, A., Lyle, R., Dalhus, B., Christensen, G., Stormorken, H., Tjonnfjord, G.E., and Frengen, E. (2014). A dominant STIM1 mutation causes Stormorken syndrome. *Hum Mutat.* 35 (5), 556-564.

102. Mo, P., and Yang, S. (2018). The store-operated calcium channels in cancer metastasis: from cell migration, invasion to metastatic colonization. *Front Biosci (Landmark Ed).* 23, 1241-1256.

103. Moremen, K.W., Tiemeyer, M., and Nairn, A.V. (2012). Vertebrate protein glycosylation: diversity, synthesis and function. *Nat Rev Mol Cell Biol.* 13 (7), 448-462.

104. Mullins, F.M., Park, C.Y., Dolmetsch, R.E., and Lewis, R.S. (2009). STIM1 and calmodulin interact with Orai1 to induce Ca2+-dependent inactivation of CRAC channels. *Proc Natl Acad Sci U S A.* 106 (36), 15495-15500.

105. Negulescu, P.A., Shastri, N., and Cahalan, M.D. (1994). Intracellular calcium dependence of gene expression in single T lymphocytes. *Proc Natl Acad Sci U S A.* 91 (7), 2873-2877.

106. Neilson, J.R., Winslow, M.M., Hur, E.M., and Crabtree, G.R. (2004). Calcineurin B1 is essential for positive but not negative selection during thymocyte development. *Immunity.* 20 (3), 255-266.

107. Novello, M.J., Zhu, J., Feng, Q., Ikura, M., and Stathopulos, P.B. (2018). Structural elements of stromal interaction molecule function. *Cell Calcium.* 73, 88-94.

108. Oh-hora, M., and Rao, A. (2009). The calcium/NFAT pathway: role in development and function of regulatory T cells. *Microbes Infect.* 11 (5), 612-619.

109. Oh-Hora, M., Yamashita, M., Hogan, P.G., Sharma, S., Lamperti, E., Chung, W., Prakriya, M., Feske, S., and Rao, A. (2008). Dual functions for the endoplasmic reticulum calcium sensors STIM1 and STIM2 in T cell activation and tolerance. *Nat Immunol.* 9 (4), 432-443.

110. Orrenius, S., Gogvadze, V., and Zhivotovsky, B. (2015). Calcium and mitochondria in the regulation of cell death. *Biochem Biophys Res Commun.* 460 (1), 72-81.

111. Orrenius, S., Zhivotovsky, B., and Nicotera, P. (2003). Regulation of cell death: the calcium-apoptosis link. *Nat Rev Mol Cell Biol.* 4 (7), 552-565.

112. Pace, C.N. (1986). Determination and analysis of urea and guanidine hydrochloride denaturation curves. *Methods Enzymol.* 131, 266-280.

113. Pace, C.N., and Shaw, K.L. (2000). Linear extrapolation method of analyzing solvent denaturation curves. *Proteins.* Suppl 4, 1-7.

114. Park, C.Y., Hoover, P.J., Mullins, F.M., Bachhawat, P., Covington, E.D., Raunser, S., Walz, T., Garcia, K.C., Dolmetsch, R.E., and Lewis, R.S. (2009). STIM1 clusters and activates CRAC channels via direct binding of a cytosolic domain to Orai1. *Cell.* 136 (5), 876-890.

115. Pavez, M., Thompson, A.C., Arnott, H.J., Mitchell, C.B., D'Atri, I., Don, E.K., Chilton, J.K., Scott, E.K., Lin, J.Y., Young, K.M., Gasperini, R.J., and Foa, L. (2019). STIM1 Is Required for Remodeling of the Endoplasmic Reticulum and Microtubule Cytoskeleton in Steering Growth Cones. *J Neurosci.* 39 (26), 5095-5114.

116. Peng, T.I., and Jou, M.J. (2010). Oxidative stress caused by mitochondrial calcium overload. *Ann N Y Acad Sci.* 1201, 183-188.

117. Pinton, P., Giorgi, C., Siviero, R., Zecchini, E., and Rizzuto, R. (2008). Calcium and apoptosis: ER-mitochondria Ca2+ transfer in the control of apoptosis. *Oncogene.* 27 (50), 6407-6418.

118. Poenie, M., Alderton, J., Tsien, R.Y., and Steinhardt, R.A. (1985). Changes of free calcium levels with stages of the cell division cycle. *Nature.* 315 (6015), 147-149.

119. Pozo-Guisado, E., Campbell, D.G., Deak, M., Alvarez-Barrientos, A., Morrice, N.A., Alvarez, I.S., Alessi, D.R., and Martin-Romero, F.J. (2010). Phosphorylation of STIM1 at ERK1/2 target sites modulates store-operated calcium entry. *J Cell Sci.* 123 (Pt 18), 3084-3093.

120. Prakriya, M., Feske, S., Gwack, Y., Srikanth, S., Rao, A., and Hogan, P.G. (2006). Orai1 is an essential pore subunit of the CRAC channel. *Nature.* 443 (7108), 230-233.

121. Prins, D., Groenendyk, J., Touret, N., and Michalak, M. (2011). Modulation of STIM1 and capacitative Ca2+ entry by the endoplasmic reticulum luminal oxidoreductase ERp57. *EMBO Rep.* 12 (11), 1182-1188.

122. Pulver, R.A., Rose-Curtis, P., Roe, M.W., Wellman, G.C., and Lounsbury, K.M. (2004). Store-operated Ca2+ entry activates the CREB transcription factor in vascular smooth muscle. *Circ Res.* 94 (10), 1351-1358.

123. Putney, J.W., Jr. (1986). A model for receptor-regulated calcium entry. *Cell Calcium.* 7 (1), 1-12.

124. Putney, J.W., Steinckwich-Besancon, N., Numaga-Tomita, T., Davis, F.M., Desai, P.N., D'Agostin, D.M., Wu, S., and Bird, G.S. (2017). The functions of store-operated calcium channels. *Biochim Biophys Acta Mol Cell Res.* 1864 (6), 900-906.

125. Rana, A., Yen, M., Sadaghiani, A.M., Malmersjo, S., Park, C.Y., Dolmetsch, R.E., and Lewis, R.S. (2015). Alternative splicing converts STIM2 from an activator to an inhibitor of store-operated calcium channels. *J Cell Biol.* 209 (5), 653-669.

126. Rao, W., Zhang, L., Peng, C., Hui, H., Wang, K., Su, N., Wang, L., Dai, S.H., Yang, Y.F., Chen, T., Luo, P., and Fei, Z. (2015). Downregulation of STIM2 improves neuronal survival after traumatic brain injury by alleviating calcium overload and mitochondrial dysfunction. *Biochim Biophys Acta.* 1852 (11), 2402-2413.

127. Rimessi, A., Giorgi, C., Pinton, P., and Rizzuto, R. (2008). The versatility of mitochondrial calcium signals: from stimulation of cell metabolism to induction of cell death. *Biochim Biophys Acta.* 1777 (7-8), 808-816.

128. Rogers, S., Wells, R., and Rechsteiner, M. (1986). Amino acid sequences common to rapidly degraded proteins: the PEST hypothesis. *Science.* 234 (4774), 364-368.

129. Romero, M., Jimenez, R., Sanchez, M., Lopez-Sepulveda, R., Zarzuelo, M.J., O'Valle, F., Zarzuelo, A., Perez-Vizcaino, F., and Duarte, J. (2009). Quercetin inhibits vascular superoxide production induced by endothelin-1: Role of NADPH oxidase, uncoupled eNOS and PKC. *Atherosclerosis.* 202 (1), 58-67.

130. Roos, J., DiGregorio, P.J., Yeromin, A.V., Ohlsen, K., Lioudyno, M., Zhang, S., Safrina, O., Kozak, J.A., Wagner, S.L., Cahalan, M.D., Velicelebi, G., and Stauderman, K.A.

(2005). STIM1, an essential and conserved component of store-operated Ca2+ channel function. *J Cell Biol.* 169 (3), 435-445.

131. Sakakura, M., Tamura, M., Fujii, N., Takeuchi, T., Hatanaka, T., Kishimoto, S., Arata, Y., and Takahashi, H. (2018). Structural mechanisms for the S-nitrosylation-derived protection of mouse galectin-2 from oxidation-induced inactivation revealed by NMR. *FEBS J.* 285 (6), 1129-1145.

132. Santella, L., Lim, D., and Moccia, F. (2004). Calcium and fertilization: the beginning of life. *Trends Biochem Sci.* 29 (8), 400-408.

133. Santulli, G., Xie, W., Reiken, S.R., and Marks, A.R. (2015). Mitochondrial calcium overload is a key determinant in heart failure. *Proc Natl Acad Sci U S A.* 112 (36), 11389-11394.

134. Secondo, A., Bagetta, G., and Amantea, D. (2018). On the Role of Store-Operated Calcium Entry in Acute and Chronic Neurodegenerative Diseases. *Front Mol Neurosci.* 11, 87.

135. Shaw, P.J., and Feske, S. (2012). Physiological and pathophysiological functions of SOCE in the immune system. *Front Biosci (Elite Ed).* 4, 2253-2268.

136. Shuttleworth, T.J. (2017). Selective activation of distinct Orai channels by STIM1. *Cell Calcium.* 63, 40-42.

137. Smyth, J.T., Petranka, J.G., Boyles, R.R., DeHaven, W.I., Fukushima, M., Johnson, K.L., Williams, J.G., and Putney, J.W., Jr. (2009). Phosphorylation of STIM1 underlies suppression of store-operated calcium entry during mitosis. *Nat Cell Biol.* 11 (12), 1465-1472.

138. Soboloff, J., Rothberg, B.S., Madesh, M., and Gill, D.L. (2012). STIM proteins: dynamic calcium signal transducers. *Nat Rev Mol Cell Biol.* 13 (9), 549-565.

139. Soboloff, J., Spassova, M.A., Dziadek, M.A., and Gill, D.L. (2006). Calcium signals mediated by STIM and Orai proteins--a new paradigm in inter-organelle communication. *Biochim Biophys Acta.* 1763 (11), 1161-1168.

140. Song, M.Y., Makino, A., and Yuan, J.X. (2011). STIM2 Contributes to Enhanced Store-operated Ca Entry in Pulmonary Artery Smooth Muscle Cells from Patients with Idiopathic Pulmonary Arterial Hypertension. *Pulm Circ.* 1 (1), 84-94.

141. Song, S., Carr, S.G., McDermott, K.M., Rodriguez, M., Babicheva, A., Balistrieri, A., Ayon, R.J., Wang, J., Makino, A., and Yuan, J.X. (2018). STIM2 (Stromal Interaction Molecule 2)-Mediated Increase in Resting Cytosolic Free Ca(2+) Concentration Stimulates PASMC Proliferation in Pulmonary Arterial Hypertension. *Hypertension.* 71 (3), 518-529.

142. Spassova, M.A., Soboloff, J., He, L.P., Xu, W., Dziadek, M.A., and Gill, D.L. (2006a). STIM1 has a plasma membrane role in the activation of store-operated Ca(2+) channels. *Proc Natl Acad Sci U S A.* 103 (11), 4040-4045.

143. Spassova, M.A., Soboloff, J., He, L.P., Xu, W., Dziadek, M.A., and Gill, D.L. (2006b). STIM1 has a plasma membrane role in the activation of store-operated Ca(2+) channels. *Proc Natl Acad Sci U S A.* 103 (11), 4040-4045. Epub 2006 Mar 4046.

144. Stathopulos, P.B., and Ikura, M. (2009). Structurally delineating stromal interaction molecules as the endoplasmic reticulum calcium sensors and regulators of calcium release-activated calcium entry. *Immunol Rev.* 231 (1), 113-131.

145. Stathopulos, P.B., and Ikura, M. (2013a). Structural aspects of calcium-release activated calcium channel function. *Channels (Austin).* 7 (5), 344-353.

146. Stathopulos, P.B., and Ikura, M. (2013b). Structure and function of endoplasmic reticulum STIM calcium sensors. *Curr Top Membr.* 71, 59-93.

147. Stathopulos, P.B., and Ikura, M. (2019). Does stromal interaction molecule-1 have five senses? *Cell Calcium.* 77, 79-80.

148. Stathopulos, P.B., Li, G.Y., Plevin, M.J., Ames, J.B., and Ikura, M. (2006). Stored Ca2+ depletion-induced oligomerization of stromal interaction molecule 1 (STIM1) via the EF-SAM region: An initiation mechanism for capacitive Ca2+ entry. *J Biol Chem.* 281 (47), 35855-35862.

149. Stathopulos, P.B., Schindl, R., Fahrner, M., Zheng, L., Gasmi-Seabrook, G.M., Muik, M., Romanin, C., and Ikura, M. (2013). STIM1/Orai1 coiled-coil interplay in the regulation of store-operated calcium entry. *Nat Commun.* 4, 2963.

150. Stathopulos, P.B., Zheng, L., and Ikura, M. (2009). Stromal interaction molecule (STIM) 1 and STIM2 calcium sensing regions exhibit distinct unfolding and oligomerization kinetics. *J Biol Chem.* 284 (2), 728-732.

151. Stathopulos, P.B., Zheng, L., Li, G.-Y., Plevin, M.J., and Ikura, M. (2008a). Structural and mechanistic insights into STIM1-mediated initiation of store-operated calcium entry. *Cell.* 135 (1), 110-122.

152. Stathopulos, P.B., Zheng, L., Li, G.Y., Plevin, M.J., and Ikura, M. (2008b). Structural and mechanistic insights into STIM1-mediated initiation of store-operated calcium entry. *Cell.* 135 (1), 110-122.

153. Sun, S., Zhang, H., Liu, J., Popugaeva, E., Xu, N.J., Feske, S., White, C.L., 3rd, and Bezprozvanny, I. (2014). Reduced synaptic STIM2 expression and impaired store-operated calcium entry cause destabilization of mature spines in mutant presenilin mice. *Neuron.* 82 (1), 79-93.

154. Surroca, A., and Wolff, D. (2000). Inositol 1,4,5-trisphosphate but not ryanodine-receptor agonists induces calcium release from rat liver Golgi apparatus membrane vesicles. *J Membr Biol.* 177 (3), 243-249.

155. Taylor, C.T., Lawrence, Y.M., Kingsland, C.R., Biljan, M.M., and Cuthbertson, K.S. (1993). Oscillations in intracellular free calcium induced by spermatozoa in human oocytes at fertilization. *Hum Reprod.* 8 (12), 2174-2179.

156. Thompson, J.L., and Shuttleworth, T.J. (2015). Anchoring protein AKAP79-mediated PKA phosphorylation of STIM1 determines selective activation of the ARC channel, a store-independent Orai channel. *J Physiol.* 593 (3), 559-572.

157. Thompson, J.L., Zhao, Y., Stathopulos, P.B., Grossfield, A., and Shuttleworth, T.J. (2018). Phosphorylation-mediated structural changes within the SOAR domain of STIM1 enable specific activation of distinct Orai channels. *J Biol Chem.*

158. Vallejo-Illarramendi, A., Toral-Ojeda, I., Aldanondo, G., and Lopez de Munain, A. (2014). Dysregulation of calcium homeostasis in muscular dystrophies. *Expert Rev Mol Med.* 16, e16.

159. van Leeuwen, J.E., and Samelson, L.E. (1999). T cell antigen-receptor signal transduction. *Curr Opin Immunol.* 11 (3), 242-248.

160. Venkatachalam, K., van Rossum, D.B., Patterson, R.L., Ma, H.T., and Gill, D.L. (2002). The cellular and molecular basis of store-operated calcium entry. *Nat Cell Biol.* 4 (11), E263-272.

161. Vig, M., DeHaven, W.I., Bird, G.S., Billingsley, J.M., Wang, H., Rao, P.E., Hutchings, A.B., Jouvin, M.H., Putney, J.W., and Kinet, J.P. (2008). Defective mast cell effector functions in mice lacking the CRACM1 pore subunit of store-operated calcium release-activated calcium channels. *Nat Immunol.* 9 (1), 89-96.

162. Walleczek, J. (1992). Electromagnetic field effects on cells of the immune system: the role of calcium signaling. *FASEB J.* 6 (13), 3177-3185.

163. Wang, X., Wang, Y., Zhou, Y., Hendron, E., Mancarella, S., Andrake, M.D., Rothberg, B.S., Soboloff, J., and Gill, D.L. (2014). Distinct Orai-coupling domains in STIM1 and STIM2 define the Orai-activating site. *Nat Commun.* 5, 3183.

164. Williams, R.T., Manji, S.S., Parker, N.J., Hancock, M.S., Van Stekelenburg, L., Eid, J.P., Senior, P.V., Kazenwadel, J.S., Shandala, T., Saint, R., Smith, P.J., and Dziadek, M.A. (2001). Identification and characterization of the STIM (stromal interaction molecule) gene family: coding for a novel class of transmembrane proteins. *Biochem J.* 357 (Pt 3), 673-685.

165. Wolhuter, K., Whitwell, H.J., Switzer, C.H., Burgoyne, J.R., Timms, J.F., and Eaton, P. (2018). Evidence against Stable Protein S-Nitrosylation as a Widespread Mechanism of Post-translational Regulation. *Mol Cell.* 69 (3), 438-450 e435.

166. Wu, J., Ryskamp, D.A., Liang, X., Egorova, P., Zakharova, O., Hung, G., and Bezprozvanny, I. (2016). Enhanced Store-Operated Calcium Entry Leads to Striatal Synaptic Loss in a Huntington's Disease Mouse Model. *J Neurosci.* 36 (1), 125-141.

167. Yang, X., Jin, H., Cai, X., Li, S., and Shen, Y. (2012). Structural and mechanistic insights into the activation of Stromal interaction molecule 1 (STIM1). *Proc Natl Acad Sci U S A.* 109 (15), 5657-5662.

168. Yap, K.A., Shetty, M.S., Garcia-Alvarez, G., Lu, B., Alagappan, D., Oh-Hora, M., Sajikumar, S., and Fivaz, M. (2017). STIM2 regulates AMPA receptor trafficking and plasticity at hippocampal synapses. *Neurobiol Learn Mem.* 138, 54-61.

169. Yazbeck, P., Tauseef, M., Kruse, K., Amin, M.R., Sheikh, R., Feske, S., Komarova, Y., and Mehta, D. (2017). STIM1 Phosphorylation at Y361 Recruits Orai1 to STIM1 Puncta and Induces Ca(2+) Entry. *Sci Rep.* 7, 42758.

170. Yeromin, A.V., Roos, J., Stauderman, K.A., and Cahalan, M.D. (2004). A store-operated calcium channel in Drosophila S2 cells. *J Gen Physiol.* 123 (2), 167-182.

171. Yeromin, A.V., Zhang, S.L., Jiang, W., Yu, Y., Safrina, O., and Cahalan, M.D. (2006). Molecular identification of the CRAC channel by altered ion selectivity in a mutant of Orai. *Nature.* 443 (7108), 226-229.

172. Yuan, J.P., Zeng, W., Dorwart, M.R., Choi, Y.J., Worley, P.F., and Muallem, S. (2009). SOAR and the polybasic STIM1 domains gate and regulate Orai channels. *Nat Cell Biol.* 11 (3), 337-343.

173. Zhang, H., Wu, L., Pchitskaya, E., Zakharova, O., Saito, T., Saido, T., and Bezprozvanny, I. (2015). Neuronal Store-Operated Calcium Entry and Mushroom Spine Loss in Amyloid Precursor Protein Knock-In Mouse Model of Alzheimer's Disease. *J Neurosci.* 35 (39), 13275-13286.

174. Zhang, S.L., Yu, Y., Roos, J., Kozak, J.A., Deerinck, T.J., Ellisman, M.H., Stauderman, K.A., and Cahalan, M.D. (2005a). STIM1 is a Ca2+ sensor that activates CRAC channels and migrates from the Ca2+ store to the plasma membrane. *Nature.* 437 (7060), 902-905.

175. Zhang, S.L., Yu, Y., Roos, J., Kozak, J.A., Deerinck, T.J., Ellisman, M.H., Stauderman, K.A., and Cahalan, M.D. (2005b). STIM1 is a Ca2+ sensor that activates CRAC channels and migrates from the Ca2+ store to the plasma membrane. *Nature.* 437 (7060), 902-905.

176. Zheng, L., Stathopulos, P.B., Li, G.Y., and Ikura, M. (2008). Biophysical characterization of the EF-hand and SAM domain containing Ca2+ sensory region of STIM1 and STIM2. *Biochem Biophys Res Commun.* 369 (1), 240-246.

177. Zheng, L., Stathopulos, P.B., Schindl, R., Li, G.-Y., Romanin, C., and Ikura, M. (2011a). Auto-inhibitory role of the EF-SAM domain of STIM proteins in store-operated calcium entry. *Proceedings of the National Academy of Sciences.* 108 (4), 1337-1342.

178. Zheng, L., Stathopulos, P.B., Schindl, R., Li, G.Y., Romanin, C., and Ikura, M. (2011b). Auto-inhibitory role of the EF-SAM domain of STIM proteins in store-operated calcium entry. *Proc Natl Acad Sci U S A.* 108 (4), 1337-1342.

179. Zheng, S., Ma, G., He, L., Zhang, T., Li, J., Yuan, X., Nguyen, N.T., Huang, Y., Zhang, X., Gao, P., Nwokonko, R., Gill, D.L., Dong, H., Zhou, Y., and Wang, Y. (2018). Identification of molecular determinants that govern distinct STIM2 activation dynamics. *PLoS Biol.* 16 (11), e2006898.

180. Zhou, M.H., Zheng, H., Si, H., Jin, Y., Peng, J.M., He, L., Zhou, Y., Munoz-Garay, C., Zawieja, D.C., Kuo, L., Peng, X., and Zhang, S.L. (2014). Stromal interaction molecule 1 (STIM1) and Orai1 mediate histamine-evoked calcium entry and nuclear factor of activated T-cells (NFAT) signaling in human umbilical vein endothelial cells. *J Biol Chem.* 289 (42), 29446-29456.

181. Zhou, Y., Mancarella, S., Wang, Y., Yue, C., Ritchie, M., Gill, D.L., and Soboloff, J. (2009). The short N-terminal domains of STIM1 and STIM2 control the activation kinetics of Orai1 channels. *J Biol Chem.* 284 (29), 19164-19168.

182. Zhu, J., Lu, X., Feng, Q., and Stathopulos, P.B. (2018). A charge-sensing region in the stromal interaction molecule 1 luminal domain confers stabilization-mediated inhibition of SOCE in response to S-nitrosylation. *J Biol Chem.* 293 (23), 8900-8911.

183. Zhu-Mauldin, X., Marsh, S.A., Zou, L., Marchase, R.B., and Chatham, J.C. (2012). Modification of STIM1 by O-linked N-acetylglucosamine (O-GlcNAc) attenuates store-operated calcium entry in neonatal cardiomyocytes. *J Biol Chem.* 287 (46), 39094-39106.

Curriculum Vitae

Name:	Matthew Joseph Novello
Post-Secondary Education & Degrees	Western University, London, Ontario, Canada Honours Specialization BMSc 2013-2017
	Western University London, Ontario, Canada MSc Physiology and Pharmacology 2017-2019
Honours & Awards	Western Scholarship of Excellence 2013-2014
	Dean's Honour List 2013-2017
	Western Graduate Research Scholarship 2017-2019
Teaching Experience	Teaching Assistant Cellular Physiology 3140A Western University 2017-2019

Publications:

Novello, M. J., Zhu, J., Feng, Q., Ikura, M., & Stathopulos, P. B. (2018). Structural elements of stromal interaction molecule function. *Cell Calcium*, 73, 88-94. doi:10.1016/j.ceca.2018.04.006.

Novello, M. J., Zhang, M., Snyder, H. E., & Lin, Q. T. (2019). Calcium desensitization in cardiac troponin C: a novel role in mouse skeletal muscle. *The Journal of physiology*, *597*(5), 1227-1229. doi.org/10.1113/JP277616.

Zhang, M., **Novello, M. J.,** Houpt, J. A., Wang, S., Lin, Q. T. (2019). Growth Cone Steering: An Emerging Role for Stromal Interaction Molecule 1. *Journal of Neuroscience*, (under review).

Novello, M. J., Zhu, J., Zhang, M., Feng, Q., & Stathopulos, P. B. (2019). Excess nitric oxide stabilizes the luminal domain of STIM2 in a Cys-specific manner thereby inhibiting basal calcium homeostasis and store-operated calcium entry, (in preparation).

Conferences:

Poster Presentation
The 11th Annual Department of Physiology and Pharmacology Research Day, Western University, London, ON, 2017.
Title: *S*-Nitrosylation suppresses stromal interaction molecule-2 stability and activation

Poster Presentation
London Health Research Day, London, ON, 2018
Title: *S*-Nitrosylation stabilizes stromal-interaction molecule 2 by inducing structural changes which suppress its activation

Platform Presentation
Western University Health and Research Conference, Western University, London, ON, 2018
Title: *S*-Nitrosylation stabilizes stromal-interaction molecule 2 by inducing structural changes which suppress its activation

Poster Presentation
The 12th Annual Department of Physiology and Pharmacology Research Day, Western University, London, ON, 2018.
Title: *S*-Nitrosylation stabilizes the luminal region of STIM2 in a cysteine-specific manner concomitant with marked structural changes

Platform Presentation
Cardiovascular Journal Club, Western University, London, ON, 2018
Title: *S*-Nitrosylation stabilizes the luminal region of STIM2 in a cysteine-specific manner concomitant with marked structural changes

Judge: Poster Presentations
Western Student Research Conference, Western University, London, ON, 2019.
Category: Molecular sciences and biotechnology.

Poster Presentation
London Health Research Day, London, ON, 2019
Title: *S*-Nitrosylation stabilizes the luminal domain of STIM2 in a Cys-specific manner thereby regulating basal calcium homeostasis and store-operated calcium entry

Platform Presentation
Canadian Nitric Oxide Society (CNOS) Conference, Trent University, Peterborough, ON, 2019.
Title: Excess NO stabilizes the luminal domain of STIM2 in a Cys-specific manner thereby regulating basal calcium homeostasis and store-operated calcium entry.